Deformation history and gold mineralization of the Cadillac Group north of the Larder Lake-Cadillac deformation zone, southern Abitibi greenstone belt, Quebec

by

Brendon Samson

A thesis submitted in partial fulfillment
of the requirements for the degree of
Master of Science (MSc) in Geology

The Faculty of Graduate Studies
Laurentian University
Sudbury, Ontario, Canada

THESIS DEFENCE COMMITTEE/COMITÉ DE SOUTENANCE DE THÈSE
Laurentian Université/Université Laurentienne
Faculty of Graduate Studies/Faculté des études supérieures

Title of Thesis Titre de la thèse	Deformation history and gold mineralization of the Cadillac Group north of the Larder Lake–Cadillac deformation zone, southern Abitibi greenstone belt, Quebec
Name of Candidate Nom du candidat	Samson, Brendon
Degree Diplôme	Master of Science
Department/Program Département/Programme	Geology
Date of Defence Date de la soutenance	August 16, 2019

APPROVED/APPROUVÉ

Thesis Examiners/Examinateurs de thèse:

Dr. Bruno Lafrance
(Supervisor/Directeur(trice) de thèse)

Xiaohui Zhou
(Co-supervisor/Co-directeur(trice) de thèse)

Dr. Stéphane Perrouty
(Committee member/Membre du comité)

Dr. Stéphane De Souza
(External Examiner/Examinateur externe)

Approved for the Faculty of Graduate Studies
Approuvé pour la Faculté des études supérieures
Dr. David Lesbarrères
Monsieur David Lesbarrères
Dean, Faculty of Graduate Studies
Doyen, Faculté des études supérieures

ACCESSIBILITY CLAUSE AND PERMISSION TO USE

Abstract

The Cadillac Group is located immediately north of the Larder Lake–Cadillac deformation zone (LLCDZ) along the southern margin of the Abitibi greenstone belt in the Archean Superior Province, Quebec. The LLCDZ is a major 250 km long structure known for hosting several gold deposits. It is generally east-trending over a distance of 170 km, and then it swings to the southeast over a distance of 35 km along the so-called Malartic segment, before resuming its easterly trend for another 45 km. With its thick sequence of <2687 Ma turbiditic sandstone interlayered with mudstone and polymictic conglomerate, the Cadillac Group provides favourable rocks for studying the structural history of the Malartic segment which, due to its unique trend, is important for understanding the overall tectonic evolution of the LLCDZ. Deformation of the Cadillac Group began with large-scale isoclinal folding and the formation of a regional cleavage parallel to the trend of the Malartic segment (D_1 event). These structures overprint a 2675.5 ± 2 Ma quartz-feldspar-phyric (QFP) intrusion providing a maximum age for the D_1 event and a minimum age for the deposition of the Cadillac sequence. The deformation of the Cadillac Group resumed with bedding-parallel sinistral shearing and the emplacement of gold-bearing extensional quartz veins (D_2 event), and continued with bedding-parallel dextral shearing, Z-shaped folding, the formation of a cleavage oriented oblique (anticlockwise) to the trend of the Malartic segment, and by the rotation and segmentation of the gold-bearing veins (D_3 event). Contrary to previous interpretations of the Malartic segment as an early pre-D_1 accretionary structure, it is interpreted as the short limb of a broad Z-shaped flexure that formed during D_3 folding of the LLCDZ and that postdates the emplacement of gold-bearing veins in the Cadillac Group. Mineralized veins at the nearby world-class Canadian Malartic deposit were emplaced during the same D_2 event but they differ in alteration mineralogy and geochemistry to the Cadillac veins suggesting different sources for the

mineralizing fluids. Mineralization at the Lapa deposit is similar in sulphide mineralogy and metal association to the Cadillac veins but was emplaced earlier during the deformation history of the LLCDZ.

Keywords

Larder Lake–Cadillac deformation zone, Malartic segment, structural evolution, Piché Group, Cadillac Group, Pontiac Group, deformation, gold mineralization

Co-Authorship Statement

This manuscript has multiple authors; this section outlines the contributions made by the co-authors and the candidate in pursuit of this Masters of Science Degree:

1. This project was developed by Dr. Bruno Lafrance and Dr. Xiaohui Zhou with input from the candidate. These two co-authors visited the field site and reviewed mapping results upon completion. Additional input was provided by Dr. Stéphane Perrouty and Mr. Pierre Pilote.
2. Field work and sample collection was completed by the candidate with the assistance of M. Jacques (2017) and L. Roy (2018). Field work was completed over two summer field seasons: (1) May-August 2017 and (2) May-August 2018. An area approximately 2 km by 5 km was mapped at a scale of 1:2000, with additional mapping at 1:100 and 1:50 scale.
3. Eighty-six samples were collected by the candidate from outcrop and saw cuts. The samples were cut by the candidate, and thin sections were prepared by Willard Desjardins at Laurentian University. Sample preparation was conducted by the candidate and were sent to ALS laboratories for whole rock crushing and analysis. One sample for zircon U-Pb TIMS was sent to the Jack Satterly Lab at the University of Toronto. Petrographic analysis was conducted on the samples by the candidate with consultation from the two co-authors.
4. All initial interpretations of the data and the first drafts were prepared by the candidate with guidance and reviews from the co-authors. Intellectual input and edits were provided by the co-authors.

Acknowledgments

First and foremost, I would like to sincerely thank you, Dr. Bruno Lafrance, for your utmost support, encouragement and guidance throughout the course of this thesis. You have taught me so much and I cannot explain how grateful I am to have had you as a supervisor.

Dr. Xiaohui Zhou, thank you for your positivity at all times. Your leadership and guidance in the field and your thorough reviews on my work are greatly appreciated.

Danielle Shirriff, you were such a delight to spend the summers with. I couldn't have asked for a better mapping or BBQing partner. Hopefully we will work together again sometime!

Field work could not have been completed without the help from Mouche Jacques, Jeremie Rivest, and Kevin Kotylak during the 2017 field season, and Luc Roy, Naomi Welt, and Sam Duckworth Battye during the 2018 field season. I will always look back on all of the fond memories, from getting the field trucks stuck to picking blueberries to catching only a single walleye throughout the entire two summers.

The constructive discussions on interpretations with Dr. Stéphane Perrouty, Mr. Pierre Pilote, Dr. Réal Daigneault, and Dr. Stéphane De Souza, were interesting and enlightening for me. Each conversation provided many considerations for this thesis. Thank you.

Dr. Mike Lesher, I appreciate all of your reviews on my geochemical plots. Your suggestions and insightful comments greatly improved my understanding of the diagrams.

Dr. Jeff Marsh, thank you so much for all of your help with the data collection on the SEM. It was a pleasure to work with you.

Thank you, Mr. Gino Roger and Mrs. Marie-France Bugnon, for allowing access to the Héva East property and making this thesis possible.

To my family, thank you for dealing with my absence throughout the past two years and putting up with my constant chatting about rocks. To my friends in Sudbury, thank you for the many great times of potlucks, board game nights, whiskey Fridays, and endless discussions about geology.

Lastly, I would like to thank my father for always being there for me during the tough times and the good. If it weren't for your constant support, these two years would have been much more difficult. To my mom, I love you, miss you, and wish you were here to see me.

I wish the best for everyone in the future and I hope we continue to cross paths during our adventures.

Table of Contents

List of Tables

List of Figures

1. Chapter 1 – Introduction to Thesis

1.1. Research Problem

The Cadillac Group is located immediately north of the Larder Lake–Cadillac deformation zone (LLCDZ) in the southern Abitibi greenstone belt in Quebec (Fig. 1.1). From west to east, it extends over a distance of 100 km from Rouyn-Noranda to Halet, where it merges with the Kewagama Group, to Val-d'Or. The Cadillac and Kewagama groups consist of sequences of turbiditic sandstone with minor polymictic conglomerate and iron formation, unconformably overlying or in fault contact with older metavolcanic rocks. The latter include the Piché Group which bounds the Cadillac Group to the south and is interpreted as the surface expression of the LLCDZ.

The LLCDZ is typically east-trending and divided into different segments, one of which is southeast-trending and known as the Malartic segment (Fig. 1.1; Bedeaux et al., 2017). The trend of the Malartic segment has been attributed to late folding by Gunning and Ambrose (1940), Dimroth et al. (1983) and Desrochers and Hubert (1996), and has been more recently interpreted by Bedeaux et al. (2017, 2018) as an early accretionary feature that became linked to east-trending segments of the LLCDZ during north-south shortening and the development of regional folds and cleavage. As several gold deposits, including the world-class Canadian Malartic deposit and the ~1 Moz Lapa deposit, are hosted near the inflection points of the Malartic segment, how this segment formed is important for understanding the origin of the LLCDZ and the emplacement of gold deposits along it. The thesis attempts to resolve this question or research problem on the origin of the Malartic segment through detailed mapping of structures and gold occurrences in the Cadillac Group flanking the LLCDZ to the north.

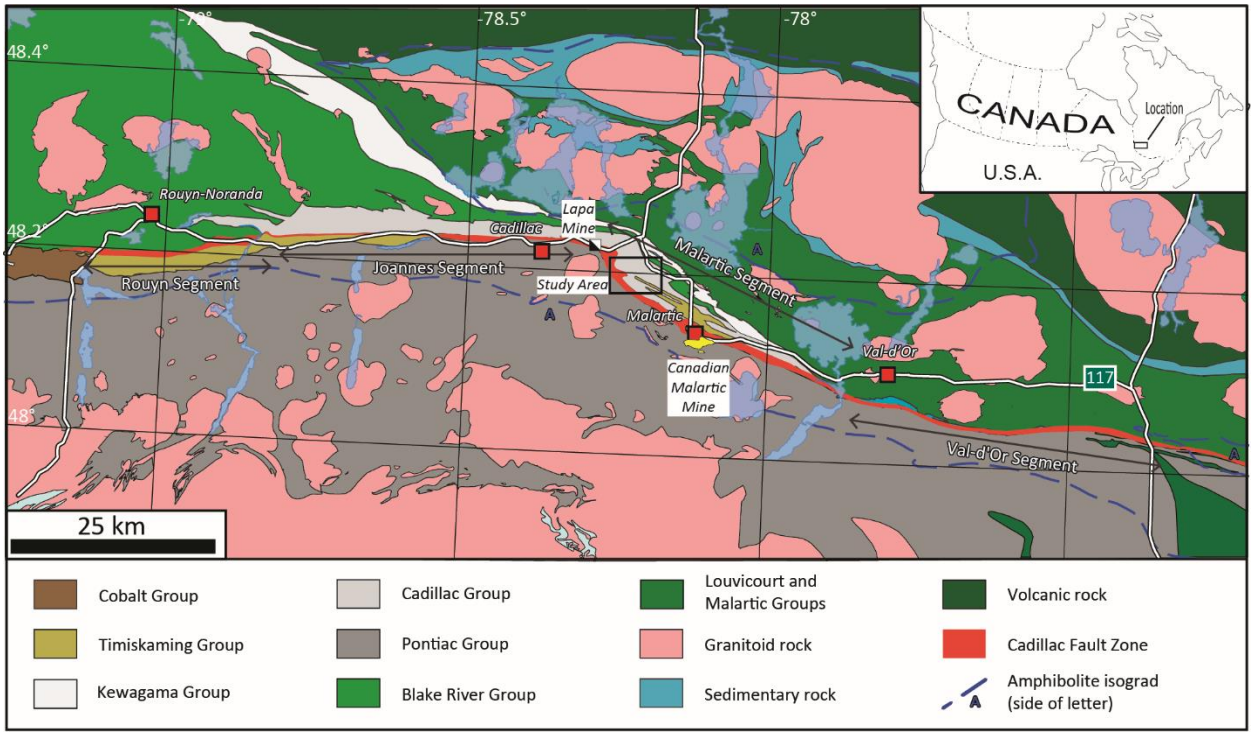

Figure 1.1: Geological map of the LLCDZ subdivided into four segments. Modified after Hubert et al. (1984), Imreh (1984), and Bedeaux et al. (2017).

1.2. Objectives of the Thesis

The thesis aims to add to the understanding of the deformation and mineralizing events along the Malartic segment of the LLCDZ. Regional mapping at 1:2000 scale along with more detailed mapping at 1:100 scale focusing on lithologies, structures and mineralization, as well as geochemical and petrographic analysis of selected samples, and U-Pb zircon geochronology (TIMS) of an intrusion, were done to achieve this goal. The main objectives of the thesis are to:

1. Establish the structural deformation history of the Cadillac Group.

2. Determine the controls on gold mineralization in the Cadillac Group and compare those to the Canadian Malartic and Lapa deposits.

3. Provide an interpretation for the large-scale tectonic evolution and present southeast trend of the Malartic segment of the LLCDZ.

1.3. Structure of Thesis

This thesis is written as two separate chapters. Chapter 1 provides an introduction to the thesis and outlines the research problem, objectives, methodology and structure of the thesis and includes a statement of contributions by the author. Chapter 2 is written as a manuscript for submission to a scientific journal and is entitled: *"Deformation history and gold mineralization of the Cadillac Group north of the Larder Lake–Cadillac deformation zone, southern Abitibi greenstone belt, Quebec"*. Co-authors on this publication are:

- Lafrance, B., Mineral Exploration Research Center, Harquail School of Earth Sciences, Laurentian University, 935 Ramsey Lake Road, Sudbury, Ontario, P3E 2C6, Canada
- Zhou, X., Mineral Exploration Research Center, Harquail School of Earth Sciences, Laurentian University, 935 Ramsey Lake Road, Sudbury, Ontario, P3E 2C6, Canada
- Hamilton, M., Jack Satterly Geochronology Research Laboratory, University of Toronto, Toronto, Ontario, M5S 3B1, Canada

Additional information collected during the research is included in appendices. **Appendix A** describes the methodology used for analyses by inductively coupled plasma mass spectrometry (ICP-MS), isotope dilution thermal ionization mass spectrometry (ID-TIMS) and scanning electron microscope (SEM). **Appendix B** contains additional whole rock geochemical analyses, assay results, and structural measurements. **Appendix C** contains two summary of field work reports that were completed after the field seasons and published by the Ministère de l'Énergie et des Ressources Naturelles du Québec.

2. Chapter 2 – Deformation history and gold mineralization of the Cadillac Group north of the Larder Lake–Cadillac deformation zone, southern Abitibi greenstone belt, Quebec

2.1 Introduction

The Cadillac Group is a 1–5 km wide linear belt of metasedimentary rocks along the southern margin of the Archean Abitibi greenstone belt in Quebec (Fig. 2.1). It is in contact with older mafic and felsic metavolcanic rocks of the Blake River Group (Goutier, 1997; Lafrance et al., 2003; Mercier-Langevin et al., 2007b; Bedeaux et al., 2018) to the north and with interleaved mafic and ultramafic rocks of the Piché Group (Bedeaux et al., 2017, 2018) to the south. The latter varies in width from 100 m to 1000 m and is bound to the south by metasedimentary rocks of the Pontiac Subprovince (Card, 1990; Calvert and Ludden, 1999). The Piché Group has been recently renamed as the Piché Structural Complex (Bedeaux et al., 2018) because of the lack of lateral continuity of internal units due to deformation and the sheared nature of its contacts with the Pontiac and Cadillac groups. The shear zones marking these contacts are part of the Larder Lake–Cadillac deformation zone (LLCDZ; Fig. 2.2), which straddles the Piché Group over a distance of 150 km from Val-d'Or in the east to Rouyn to the west in Quebec, and extends an additional 100 km in Ontario along the contact between the Larder Lake Group (Jensen, 1978), which is equivalent to the Piché Group (Poulsen, 2017), and younger metasedimentary rocks of the Timiskaming assemblage.

The LLCDZ is one of two major deformation zones in the southern Abitibi greenstone belt long recognized as major structures or "breaks" defined by the occurrence of gold deposits (Knight, 1924; Bell and Bell, 1931; Gunning and Ambrose, 1939). The Sigma-Lamaque gold

deposit in Val-d'Or, Quebec, the Canadian Malartic gold deposit in Malartic, Quebec, and the Kerr-Addison gold deposit in Virginiatown, Ontario, are amongst several major orogenic gold deposits along the LLCDZ and associated secondary structures (Robert et al., 2005). Resolving how the LLCDZ initially formed and later evolved is therefore essential for understanding the gold endowment of the southern Abitibi greenstone belt.

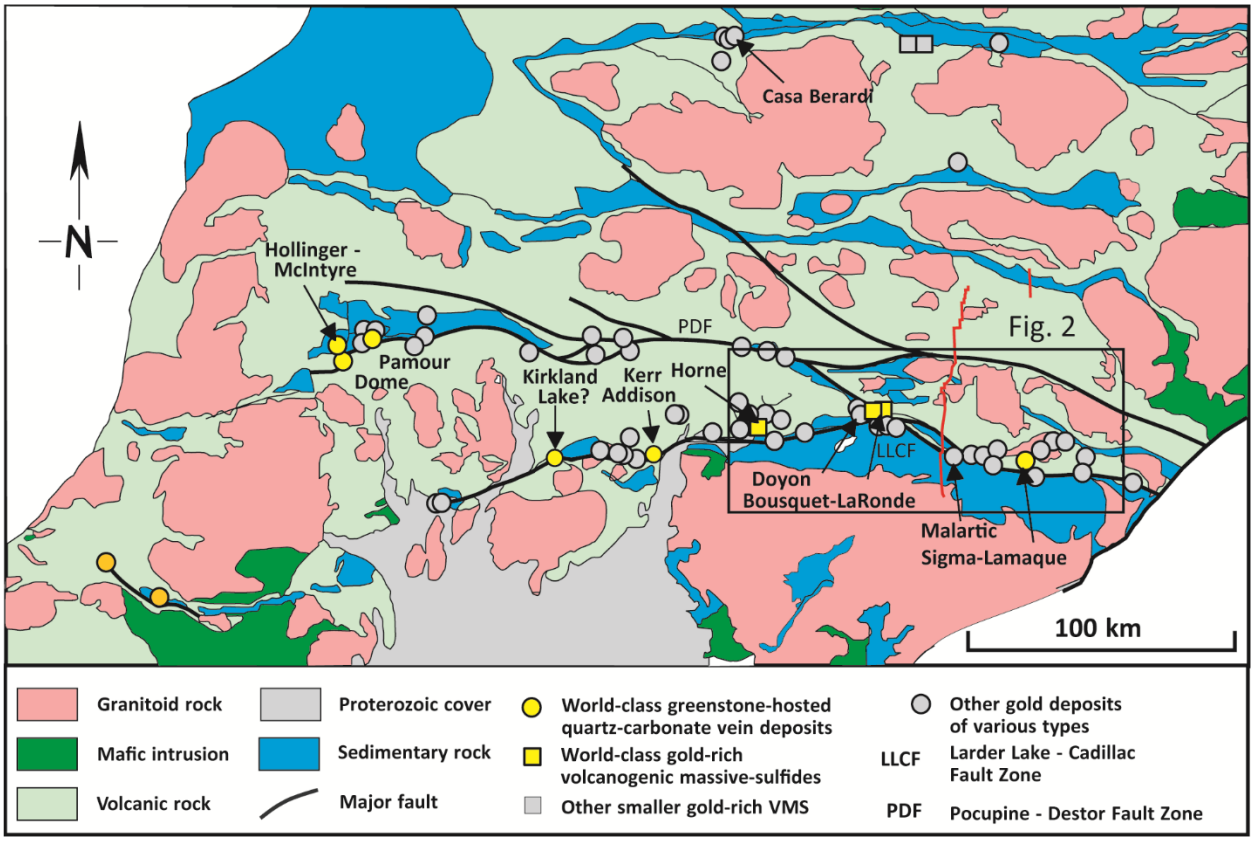

Figure 2.1: Simplified geological map of the Abitibi greenstone belt showing the distribution of major fault zones and mineral deposits. The Malartic transect of the Metal Earth research project is highlighted in red. Modified after Dubé and Gosselin (2007).

In Quebec, the LLCDZ is roughly east-trending with one major, 40 km long, SE-trending segment, named the Malartic segment (Fig. 2.2; Bedeaux et al., 2017). In the past literature, this major bend has been interpreted as a simple flexure or Z-shaped drag fold that formed late during the tectonic history of the greenstone belt after early isoclinal regional folding (Gunning and

Ambrose, 1940; Dimroth et al., 1983; Desrochers and Hubert, 1996). More recently, it has been re-interpreted as an early structure that became linked to adjacent east-trending segments during later deformation along the LLCDZ (Bedeaux et al., 2017, 2018). This imparted an early configuration to the southern margin of the Abitibi greenstone belt that later influenced the development of structures, the formation of dilational sites, the flow of hydrothermal fluids, and the emplacement of gold deposits along the LLCDZ (Bedeaux et al., 2017, 2018). To test this hypothesis, structures in the Cadillac Group along the Malartic segment were mapped and their orientation and relative structural chronology were compared to those along other segments of the LLCDZ. To provide further constraints on the early evolution of the LLCDZ, the nature of an intrusion along the Piché-Cadillac contact was investigated. Based on these new findings, a structural interpretation is proposed for the Cadillac Group and LLCDZ, which is then used to interpret the formation of orogenic gold occurrences in the Cadillac Group and compare their formation to that of the Canadian Malartic and Lapa deposits.

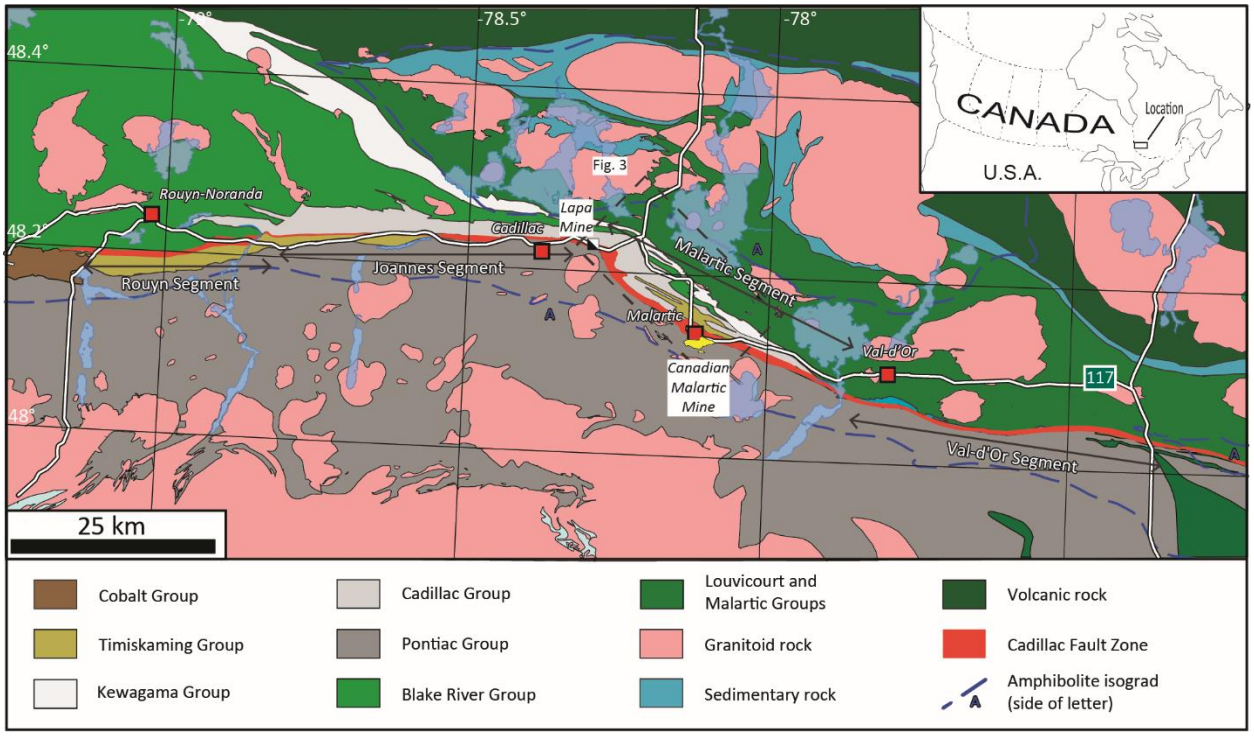

Figure 2.2: Geological map of the LLCDZ subdivided into four segments. Modified after Hubert et al. (1984), Imreh (1984), and Bedeaux et al. (2017).

2.2 Regional Geology

The Cadillac Group is located along the southern margin of the Archean Abitibi greenstone belt. It consists of turbiditic wacke and minor iron formation and polymictic conglomerate with a maximum depositional age of <2687 ± 3 Ma (U-Pb detrital zircon; Davis, 2002). The Cadillac Group is in unconformable contact and in fault contact with older metavolcanic rocks of the Blake River Group (Goutier, 1997; Lafrance et al., 2003; Mercier-Langevin et al., 2007b; Bedeaux et al., 2018), and it correlates with the <2690–2685 Ma Porcupine Group in Timmins, Ontario (Ayer et al., 2005), which also consists of turbiditic wacke unconformably overlying older metavolcanic rocks (Bleeker and Parrish, 1996). Near Malartic, the Cadillac Group is overlain by the Timiskaming Group (Fig. 2.3). Although the Cadillac-Timiskaming contact is not observed, it is likely an unconformity or a faulted unconformity as observed in Timmins,

Ontario, between the Porcupine Group and the Timiskaming Group (Born, 1995). The Timiskaming Group is dominated by alluvial-fluvial conglomerates, crossbedded sandstones and turbidites. The youngest detrital zircon population in a conglomerate sample yielded a weighted mean U-Pb date of 2677 ± 0.9 Ma (ID-TIMS on zircon; David et al., 2018). This date is interpreted as the maximum depositional age for the Timiskaming Group in the Malartic area (Pilote et al., 2015; David et al., 2018). 70 km to the west of Malartic, and 5 km to the south of Rouyn, volcaniclastic rocks interbedded with wacke in the Timiskaming Granada basin yielded a primary crystallization age of 2673 ± 2 Ma using sensitive high-resolution ion microprobe (SHRIMP) on zircon (Davis, 2002). In this same area, a 2672 ± 2 Ma feldspar syenite porphyry pluton cuts through the Timiskaming Group (SHRIMP on zircon; Davis, 2002). These two ages collectively suggest an age of ca. 2673 Ma for the formation and deposition of the Timiskaming Group. In Ontario, Timiskaming conglomerates and sandstone are interbedded and in conformable contact with alkalic to calc-alkaline volcanic rocks (Thompson, 1949; Hewitt, 1963; Ridler, 1970; Hyde, 1980), which returned a primary crystallization age of 2669 ± 1.4 Ma (SHRIMP on zircon; Ayer et al., 2005). A similar age of 2669.6 ± 1.4 Ma, was also obtained for volcanic rocks interlayered within the Timiskaming Group in the Kirkland Lake area (Ispolatov et al., 2008).

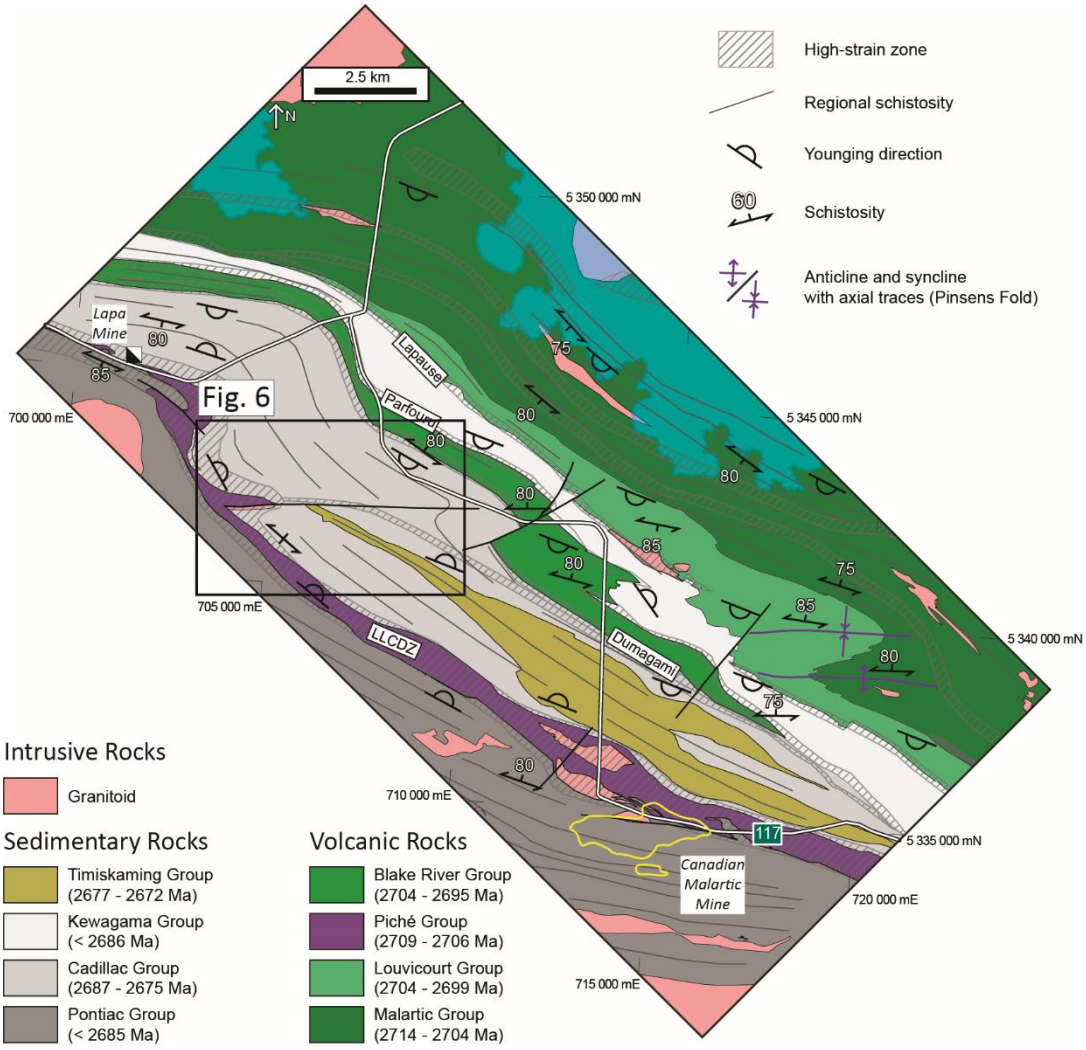

Figure 2.3: Geological map of the Malartic segment of the LLCDZ. Modified after Bedeaux et al. (2017).

The Cadillac Group is in contact with metavolcanic rocks of the Blake River Group to the north and the Piché Group to the south. The Blake River Group varies in age from ca. 2704 to 2695 Ma (Corfu et al., 1989, 1993; Mortensen, 1993; McNicoll et al., 2014) and is composed of basaltic flows with intercalated felsic flows and intermediate volcaniclastic rocks (Pearson and Daigneault, 2009; Ross et al., 2011; Mueller et al., 2012; Moore et al., 2016). It corresponds to the 2704–2695 Ma Blake River assemblage of Thurston et al. (2008) and represents a subaqueous oceanic environment at depths below storm wave base (Mueller et al., 1994). The

Piché Group varies in age from ca. 2709–2706 Ma (Pilote et al., 2015; David et al., 2018) and is interpreted as a tectonic imbricate of Malartic and Louvicourt metavolcanic rocks (Bedeaux et al., 2018). The ca. 2714–2704 Ma Malartic Group consists of komatiitic flows and basaltic to andesitic flows (Pilote et al., 1999, 2000, 2015). It corresponds to the 2719–2711 Ma Kidd-Munro and 2710–2704 Ma Tisdale assemblages of Thurston et al. (2008) and represents a deep ocean-floor volcanic environment (Dimroth et al., 1983; Scott et al., 2002). The ca. 2704–2699 Ma Louvicourt Group conformably overlies the Malartic Group and consists of andesitic, dacitic and rhyolitic flows as well as volcaniclastic units (Pilote et al., 1999, 2015; Scott et al., 2002). It corresponds to the 2710–2704 Ma Tisdale assemblage of Thurston et al. (2008) and represents a transition from a deep ocean-floor volcanic environment to a volcanic arc environment (Scott et al., 2002).

The Piché Group is overprinted by the LLCDZ (Fig. 2.3) and is considered the physical expression of the deformation zone (Dimroth et al., 1983). The LLCDZ is a prominent structure at the contact between the Abitibi greenstone belt and the Pontiac Subprovince to the south (Card, 1990). The LLCDZ is steeply south-dipping in Ontario from Matachewan to the Cheminis mine in Larder Lake and north-dipping from Larder Lake to Val-d'Or in Quebec (Poulsen, 2017). It is interpreted as: (1) a reverse north- or south-verging shear zone (Hodgson and Hamilton, 1989; Smith et al., 1993; Daigneault et al., 2002; Ispolatov et al., 2008; Bleeker, 2012), (2) a reactivated normal fault (Dimroth et al., 1983; Cameron, 1993; Bleeker, 2012), and (3) a transpressional shear zone (Robin and Cruden, 1994; Wilkinson et al., 1999). Although very different, these interpretations all portray the LLCDZ as a major transcrustal shear zone that focused the upward flow and migration of hydrothermal fluids to form gold deposits.

The Pontiac Subprovince lies to the south of the Piché Group and is similar in age and rock

type to the Cadillac Group and is interpreted as a forearc accretionary terrane (Card, 1990; Calvert and Ludden, 1999) consisting mainly of turbiditic wacke, plutons, and thin ultramafic units (Camiré, 1993). It has also been interpreted as a syn-orogenic foreland basin (Camiré and Burg, 1993; Davis, 2002; Kimura et al., 1993) and as a rift-fill basin that was later deformed and metamorphosed during later accretion (Benn et al., 1994; Bédard, 2018). It is bracketed in age between <2685 ± 3 Ma, the maximum depositional age of the turbiditic wacke (Mortensen, 1993; Davis, 2002; De Souza et al., 2017), and 2682.4 ± 1.0 Ma, the crystallization age of the Lac Fournière Pluton, which cuts the metasedimentary rocks south of Malartic (Davis, 2002).

The Abitibi greenstone belt is metamorphosed to greenschist facies with localized zones of higher metamorphic grade amphibolite facies adjacent to intrusions (Robert et al., 2005). In the Pontiac Subprovince, metamorphic grade increases from north to south from greenschist facies adjacent to the Piché Group to amphibolite facies roughly 5 km south of the Piché Group (Benn et al., 1994; Piette- Lauzière et al., 2019). Henceforth, as all supracrustal rocks of the Abitibi greenstone belt and Pontiac Subprovince are metamorphosed, for brevity the prefix “meta” will be inferred.

2.3 Local Geology

2.3.1 Cadillac Group

The Cadillac Group consists mainly of interlayered sandstone and mudstone, with lesser polymictic conglomerate and iron formation (Trudel et al., 1992). Interlayered sandstone and mudstone are fine- to medium-grained, thinly-bedded (1-10 cm) turbidites. Beds are normally graded with sharp lower surfaces and sandstone-siltstone bottoms fining upward to mudstone (Fig. 2.4a). Polymictic conglomerate occurs in the southeastern part of the study area near its contact with the Piché Group. Beds are typically ~1 m thick and can be up to ~5 m thick. The

conglomerate is clast-supported and consists of subrounded (aspect ratio of 1:2), large (1 to 35 cm) granitoid clasts, surrounded by flattened (aspect ratio of 1:15), smaller (1 to 25 cm) clasts of mafic and felsic volcanic rocks, mafic intrusive rocks, sandstone, and black chert (Fig. 2.4b). Massive sandstone is found interlayered with both turbidites and polymictic conglomerate. Beds are ~50 cm to 3 m thick and consist of fine- to medium-grained subrounded quartz and feldspar grains with minor biotite. Oxide-facies iron formation is locally interbedded with turbidites as alternating magnetite-rich and fine-grained sandstone lamellae, varying in thickness from ~1 mm to 1 cm. Up to 100 m thick bands of highly magnetic iron formation can be traced on the Ministère des Ressources Naturelles et de la Faune du Québec (MRNF) aeromagnetic map (D'Amours and Intissar, 2012).

2.3.2 Timiskaming Group

The Timiskaming Group occupies the central part of the study area. Its southern contact with the Cadillac Group is not exposed but is either a discontinuity or a conformable contact because beds in the two sedimentary groups strike and dip parallel to each other. Along its northern contact with the Cadillac Group, both groups young towards the north suggesting that the older Cadillac Group is stratigraphically above the younger Timiskaming Group. This contact relationship can be interpreted as: (1) a fault contact where the Cadillac Group was thrusted on top of the Timiskaming Group; or (2) the result of an early folding event affecting the Cadillac Group prior to the deposition of the Timiskaming Group (Bouchard, 1980). The Timiskaming Group consists primarily of polymictic conglomerate and sandstone. Beds of polymictic conglomerate vary in thickness from 1 m to 5 m and consist of self-supported clasts of granodiorite-tonalite, mafic and felsic volcanic rocks, sandstone, chert and smokey quartz, surrounded by a sandy matrix (Fig. 2.4c). Granodiorite-tonalite clasts are subrounded and larger

in size than the other clasts which are flattened parallel to foliation. Thickly-bedded sandstone horizons are typically massive, <1 m to 5 m in thickness, with locally preserved ripples and planar to trough cross laminations (Fig. 2.4d).

2.3.3 Quartz-Feldspar-Phyric Intrusion

A quartz-feldspar-phyric (QFP) intrusion occurs along the contact between the Piché Group and Cadillac Group. It can be traced for up to 1 km and at its thickest point is ~250 m wide. It is white to beige on outcrop surface and grey on fresh surface. It is quartz- and plagioclase-phyric with an equigranular matrix (<0.05 - 0.1 mm in size) of quartz, feldspar, biotite and tourmaline with minor zircon and apatite. Quartz and plagioclase phenocrysts range in size from 0.5 to 3 mm in the centre of the intrusion and from 0.5 to 1 mm along the margins of the intrusion (Fig. 2.4e). Quartz phenocrysts have embayed grain shapes, plagioclase phenocrysts are replaced by secondary albite and sericite, and biotite is hydrothermally-altered to chlorite. A tectonic foliation is defined by biotite and muscovite alignment within the intrusion.

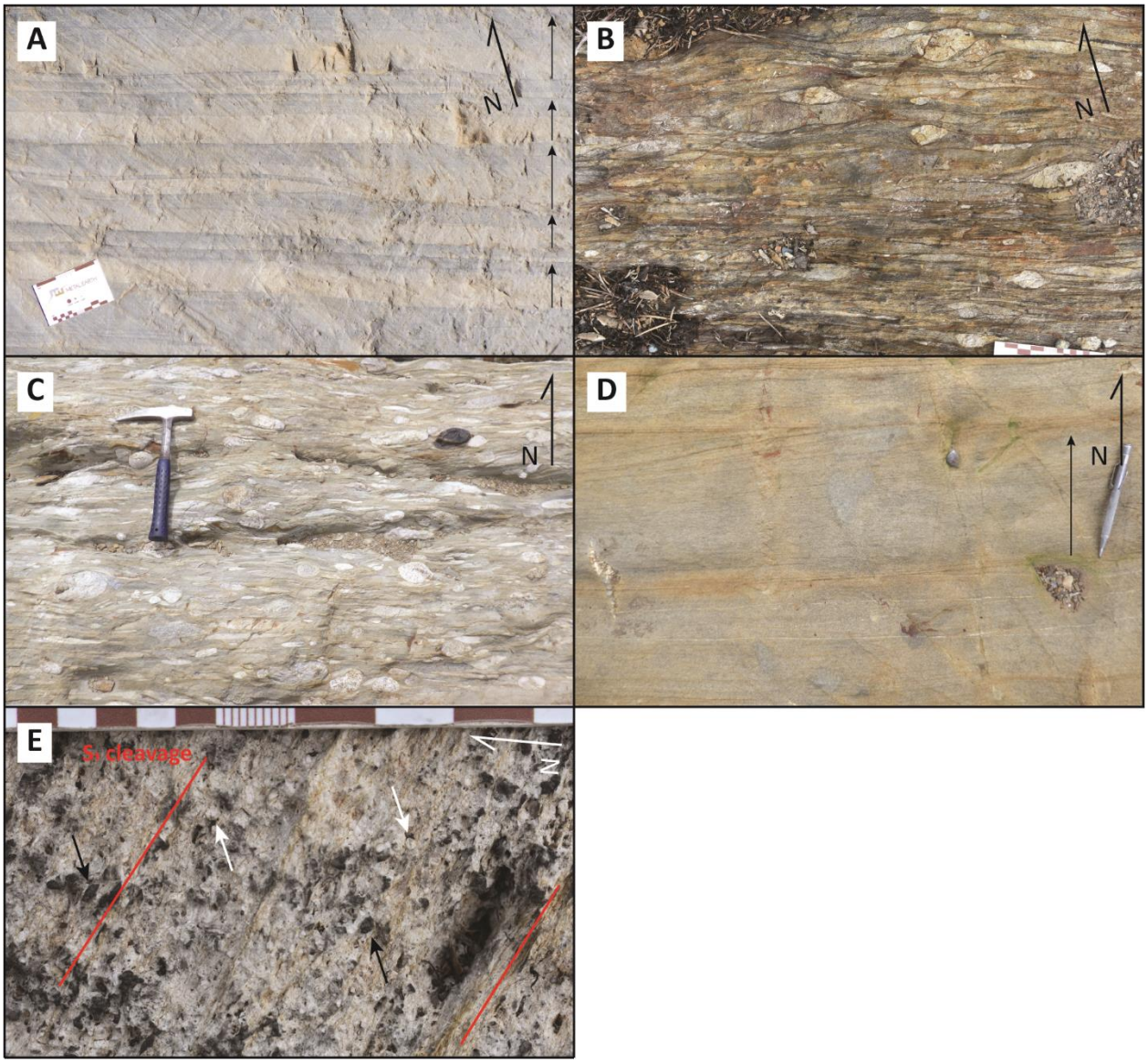

Figure 2.4: Field photographs. (a) Turbiditic wacke of the Cadillac Group. Younging direction is in the direction of the black arrows and is indicated by normal grading. Photo card (9 cm in length) for scale. (b) Polymictic conglomerate at the base of the Cadillac Group. Photo card (9 cm in length) for scale. (c) Polymictic conglomerate of the Timiskaming Group. Hammer (33 cm in length) for scale. d) Cross-bedded sandstone of the Timiskaming Group. Magnet pen (13 cm in length) for scale. (e) QFP intrusion with quartz and feldspar phenocrysts and a strong foliation defined by biotite and muscovite. Black and white arrows point to quartz and feldspar phenocrysts, respectively. Scale bar at the top of photograph is 7 cm in length.

2.4 Structural geology of the Cadillac Group

The Cadillac Group experienced four deformation events (D_1-D_4). In accordance with previous studies, D_1 refers to the first regional deformation event that affected both the Cadillac and Timiskaming groups. Pre-Timiskaming deformation of older volcanic rocks (e.g., Blake

River Group; Hubert, 1990), is not discussed in this study. Table 1 relates the deformation events presented here to those in previous studies. Structural measurements from the Cadillac and Timiskaming groups along the Malartic segment of LLCDZ is summarized in Table 1. All structural data are compiled on stereonet plots in Figure 2.5.

Table 1: Summary of deformation events along the LLCDZ in Quebec.

	Bedeaux et al. (2017)		**Gunning and Ambrose (1940)***	**Perrouty et al. (2017) & De Souza et al. (2017)**	**This study**
	Rouyn-Joannes	Malartic	Malartic	Pontiac	Malartic
NW-SE Shortening	**D4** NE-trending, vertical cleavage, axial planar to asymmetrical Z-shaped folds	**D4** NE-trending, vertical cleavage, axial planar to asymmetrical Z-shaped folds	**D3** ENE-trending, vertical cleavage, axial planar to asymmetrical Z-shaped folds	**D3** NE-trending, vertical cleavage, axial planar to asymmetrical Z-shaped folds	**D3** ENE-trending, vertical cleavage axial planar to asymmetrical Z-shaped folds
NE-SW Shortening	**D3** NW-trending, steeply dipping cleavage axial planar to asymmetrical S-shaped folds	**D3** Not observed	**D2** NW-trending, steeply dipping cleavage axial planar to asymmetrical S-shaped folds	**D2** NW-trending, steeply dipping cleavage axial planar to asymmetrical S-shaped folds	**D2** Bedding-parallel sinistral shearing, sigmoidal S-shaped tension gashes, WNW-trending extensional veins
Extension	**D2** Horizontal cleavage axial planar to open folds	**D2** Not observed	—	—	—
N-S Shortening	**D1** E-trending, moderately dipping cleavage axial planar to isoclinal folds	**D1** E-trending, vertical cleavage axial planar to tight Z-shaped folds	**D1** SE-trending, vertical cleavage axial planar to isoclinal folds	**D1** Bedding-parallel cleavage axial planar to isoclinal folds	**D1** ESE-trending, vertical cleavage axial planar to isoclinal folds

*Gunning and Ambrose (1940) did not group structures into deformation events, which are inferred based on their structural observations.

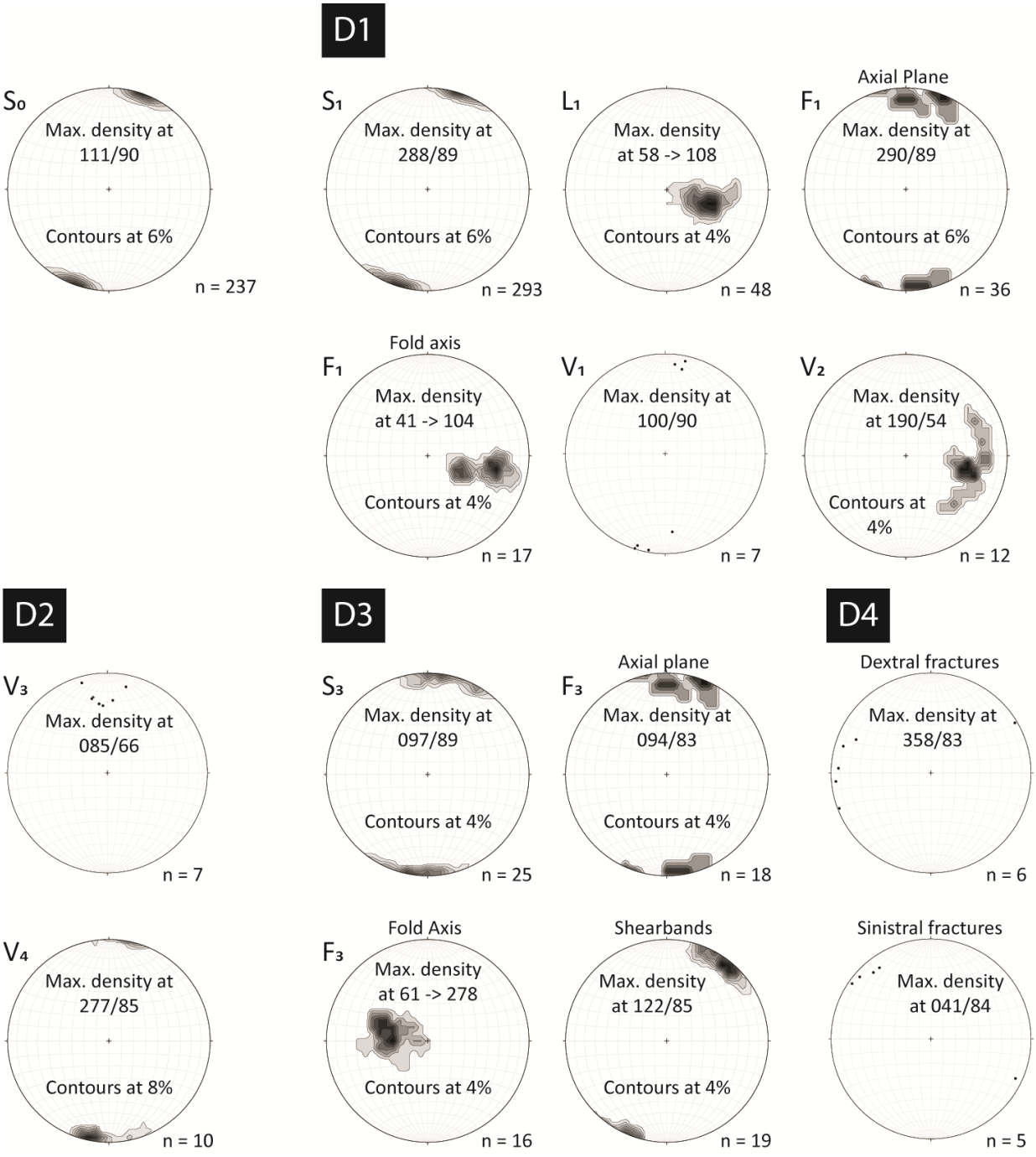

Figure 2.5: Stereonet plots of lineations and fold axes, and poles to veins, foliations and fold axial planes in the Cadillac and Timiskaming groups, Malartic segment. The contours are in percentage of the total data points per 1% area of the stereonet.

2.4.1 D_1 Deformation Event

Regional, tight to isoclinal, F_1 folds overprint the sedimentary rocks of the Cadillac and Timiskaming groups. The regional folds are depicted by bedding form surface lines in Figure

2.6, and detailed outcrop maps from opposite limbs of the folds are shown in Figure 2.7a and 2.7b. F_1 folds are upright with steeply dipping (~85-90°), west-northwest striking (~290°) axial planes, and fold axes plunging moderately (~40°) to the east-southeast (~105°) (Fig. 2.8a). A regional west-northwest striking S_1 cleavage is axial planar to the folds. The S_1 cleavage is oriented clockwise to south-facing beds (Figs. 2.7a, 2.8b) and anticlockwise to north-facing beds (Figs. 2.7b, 2.8c). It is axial planar to S-shaped and Z-shaped parasitic F_1 folds on the south-facing (Fig. 2.7a) and north-facing limbs of regional F_1 folds (Fig. 2.7b), respectively. The S_1 cleavage is expressed as a slaty cleavage in mudstone, where it is defined by the preferred orientation of biotite, muscovite, and elongate quartz and feldspar grains, and as a disjunctive spaced cleavage in sandstone (Fig. 2.8c), where it is defined by ~0.5 mm thick microlithons of quartz and feldspar bound by discontinuous biotite and muscovite domains. Clasts are strongly flattened parallel to the S_1 cleavage in conglomerate and in the QFP intrusion at the Piché-Cadillac contact. The S_1 cleavage in the QFP is represented by parallel and smooth, disjunctive cleavage domains of biotite and muscovite, separating ~1 mm thick microlithons of quartz and feldspar (Fig. 2.4e).

A lineation (L_1) is roughly parallel to F_1 fold axes. It has a moderate (~50°) plunge to the east-southeast (~105°). It is expressed as an intersection lineation between bedding (S_0) and the S_1 cleavage, as a mineral lineation defined by an early metamorphic porphyroblast replaced by biotite in mudstone (Fig. 2.8d), as an aggregate lineation defined by elongate quartz-feldspar domains in sandstone and the QFP intrusion, and as a stretching form lineation defined by deformed elongate clasts in conglomerate.

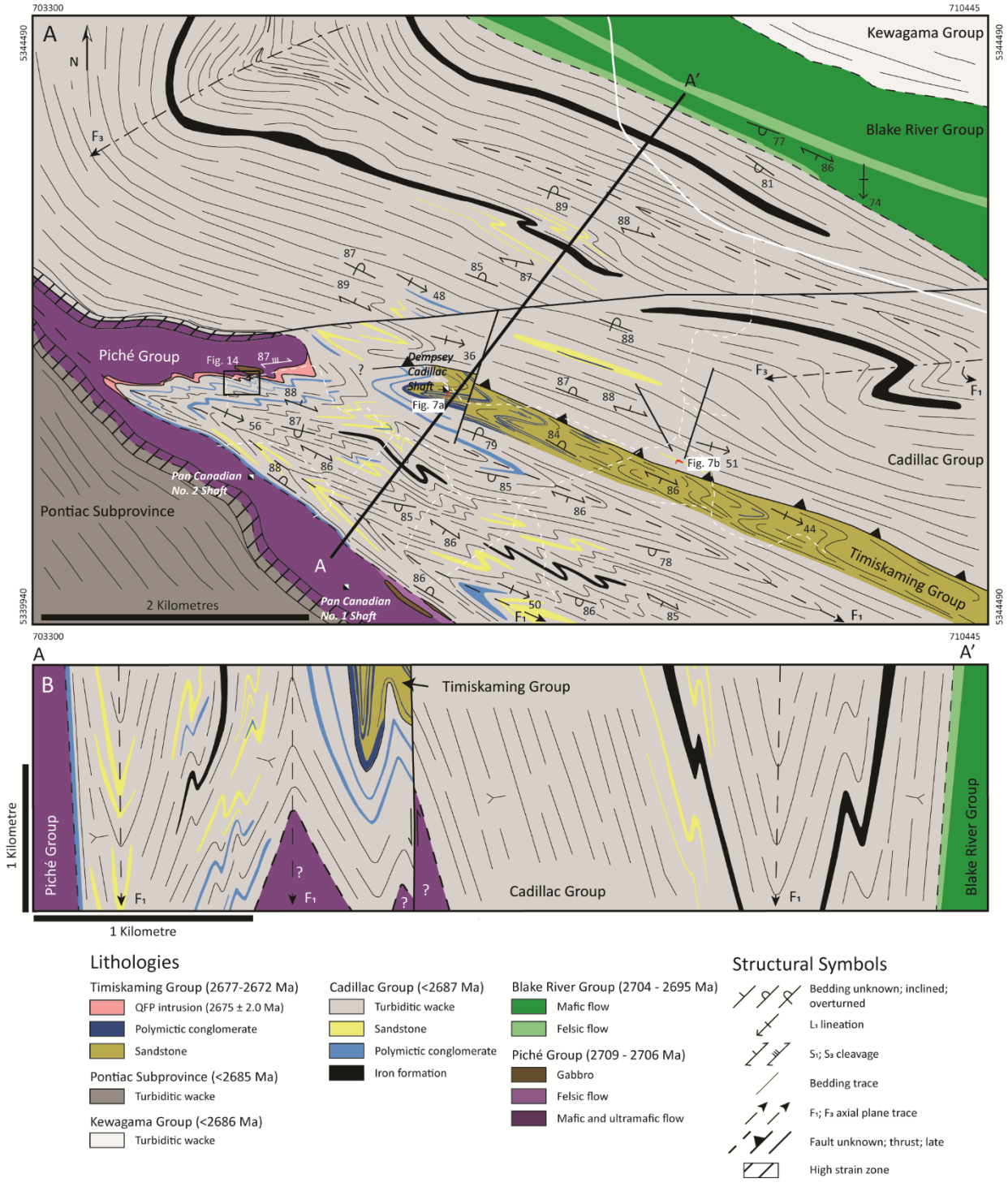

Figure 2.6: (a) Geological map of the Cadillac and Timiskaming groups. The Cadillac Group is folded into a syncline defined by regional isoclinal F_1 folds overprinted by Z-shaped F_3 folds. The Piché Group has also been folded by the F_1 syncline. The location of the section in (b), the outcrop maps of Figure 2.7a and 2.7b, and the detailed map area in Figure 2.14 are represented by the black A-A' line, the red outcrop outlines, and the black open rectangle, respectively. (b) Cross-section of the Cadillac and Timiskaming groups. The Piché Group is folded beneath the Cadillac Group.

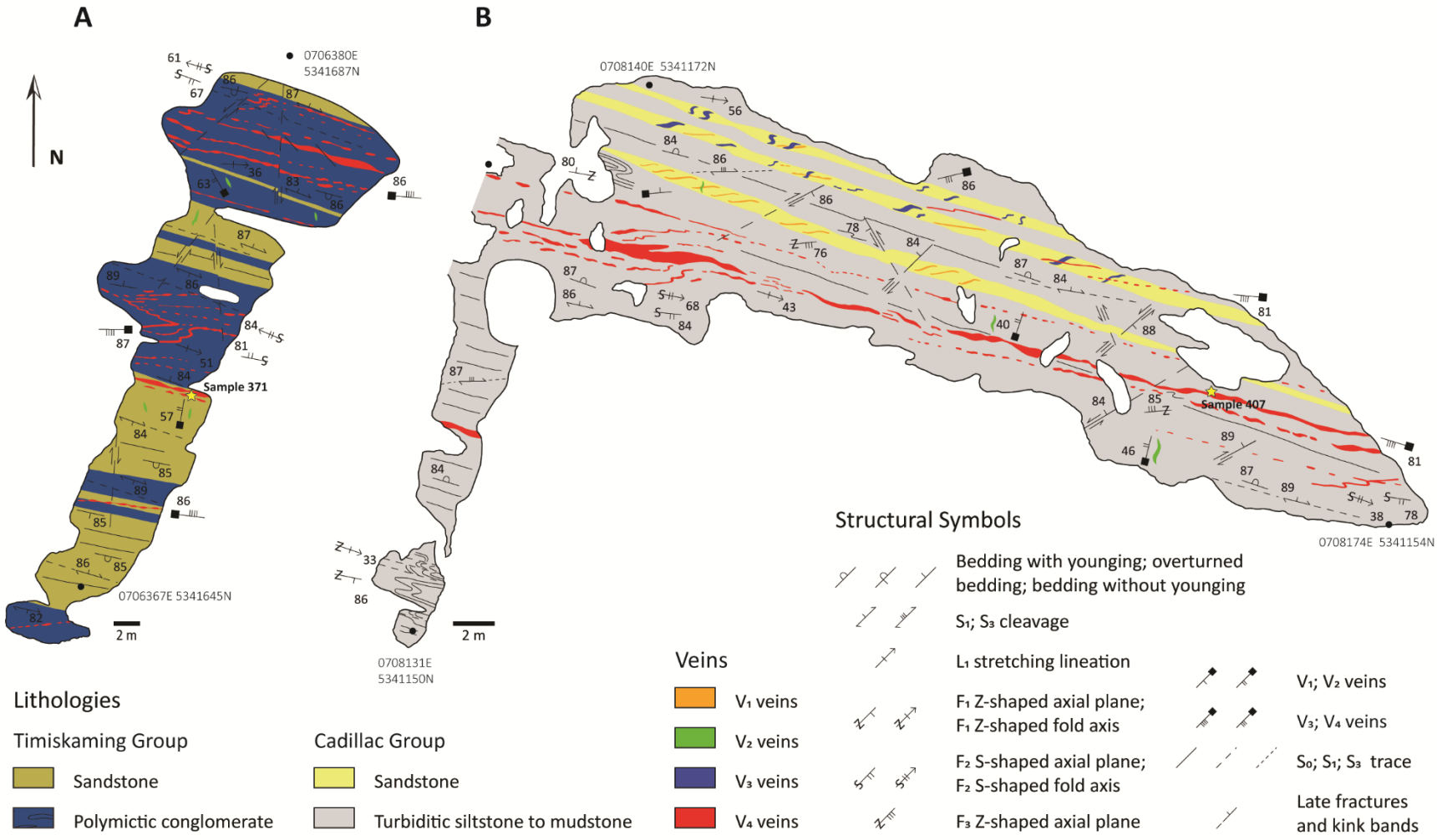

Figure 2.7: Geological maps of stripped outcrops on opposite limbs of a regional fold. (a) Timiskaming outcrop with bedding south-younging and cleavage oriented clockwise to bedding. V_4 veins are oriented anticlockwise to bedding. (b) Cadillac outcrop with bedding north-younging and cleavage oriented anticlockwise to bedding. V_4 veins are also oriented anticlockwise to bedding. See Figure 2.6a for locations.

Two sets of veins are spatially associated with D_1 structures. V_1 veins are present in competent sandstone beds as *en echelon* arrays of dark quartz-filled fractures oriented at a small angle to the S_1 cleavage and bedding (Fig. 2.8e). They are subvertical with an average strike of ~100°. They vary in width from ~2 mm to 3 cm and either terminate within the sandstone beds or extend across the complete width of the beds as ladder veins. V_2 veins are lozenge-shaped tension gashes composed of quartz, albite, Fe-carbonate and biotite (Fig. 2.8f). They have an average length of ~10 cm and vary in width from ~2 to 5 cm. They cut across the earlier V_1 veins. They have an average strike of 190° and dip of 55° and are oriented sub-perpendicular to the stretching L_1 lineation, suggesting that they formed during extension parallel to the lineation.

2.4.2 D_2 Deformation Event

The D_2 deformation event within the Cadillac and Timiskaming groups along the Malartic segment is characterized by the formation of two vein generations, V_3 and V_4. There is evidence for folding during this deformation event at Canadian Malartic and the generation of a northwest-trending cleavage along the Joannes segment (Fig. 2.2) of the LLCDZ. Along the Malartic segment, V_3 veins are ~2 cm to 10 cm thick veins of smoky grey to white quartz. They strike roughly east (085°) with an average dip of 65° towards the south. They can be traced across thick sandstone beds as *en echelon*, sigmoidal S-shaped veins oriented anticlockwise to bedding (Fig. 2.9a). They refract in clockwise manner as they pass from the thick sandstone beds into surrounding thinner beds where they terminate within a distance of a few centimetres. V_4 veins form a prominent set of younger crosscutting black smoky to white quartz veins, varying in width from ~1 cm to 25 cm. They have an average strike of 275° and an average dip of 85°. They can be traced for more than 100 meters across large stripped outcrops on both limbs of a regional F_1 fold (Figs. 2.7a, b), where they are oriented anticlockwise to bedding and are overprinted by

S-shaped folds on both north- (Fig. 2.9b) and south-younging (Figs. 2.9c, d) limbs of the regional fold.

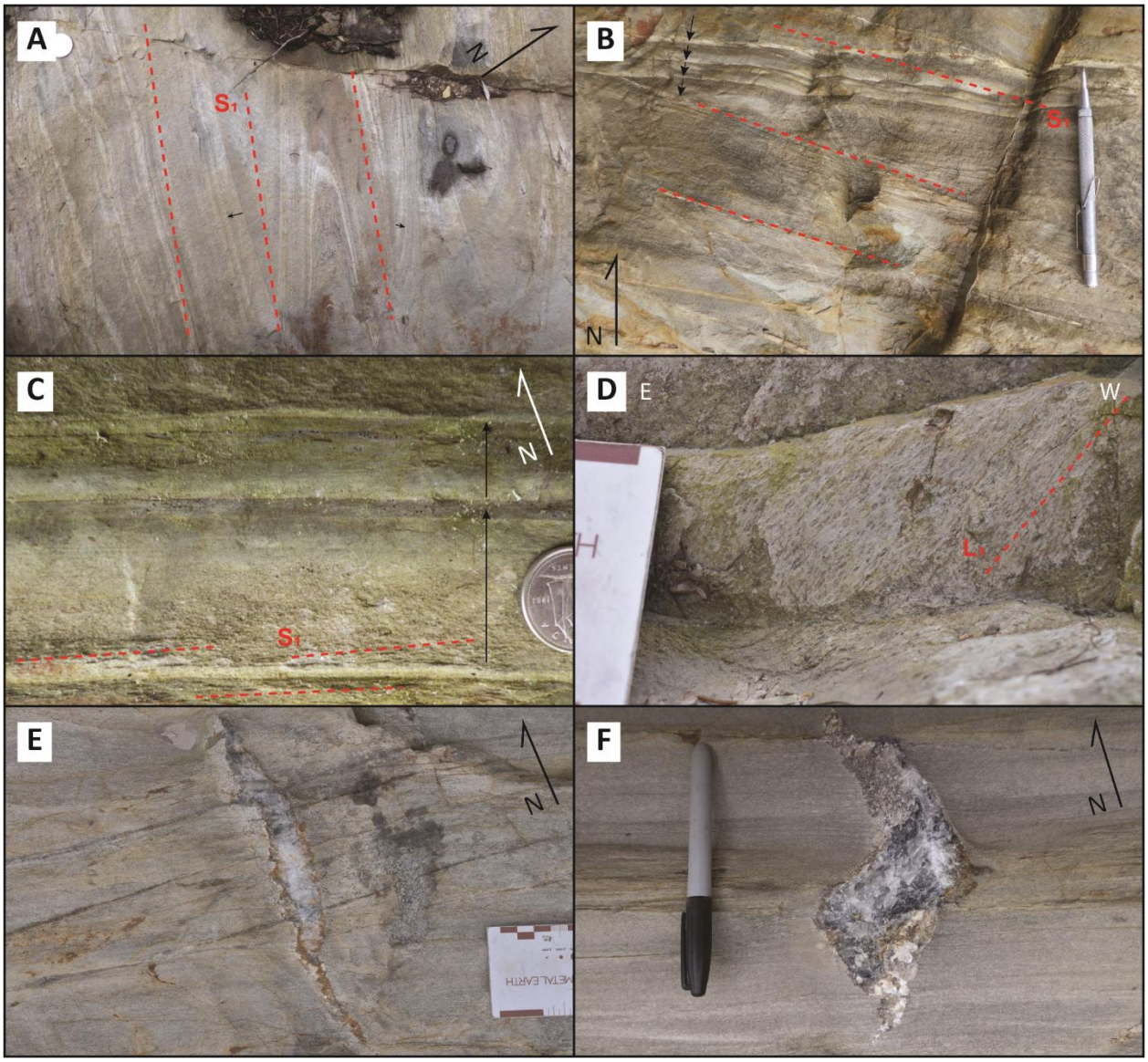

Figure 2.8: Field photographs. (a) Parasitic F_1 folds in turbiditic wacke of the Cadillac Group. Coin (18 mm diameter) for scale. (b) S_1 cleavage oriented clockwise to south younging bedding. Pen magnet (13 cm in length) for scale. (c) S_1 spaced cleavage defined by biotite oriented anticlockwise to north younging bedding. Coin (18 mm diameter) for scale. (d) L_1 mineral lineation defined by an early metamorphic porphyroblast replaced by biotite in turbiditic wacke. Edge of photo card is 5 cm. (e) V_1 vein oriented at a small angle to bedding and cut by a later V_2 vein. Photo card (5 cm in length) for scale. (f) V_2 vein oriented subperpendicular to the L_1 stretching lineation. Marker pen (13 cm) for scale.

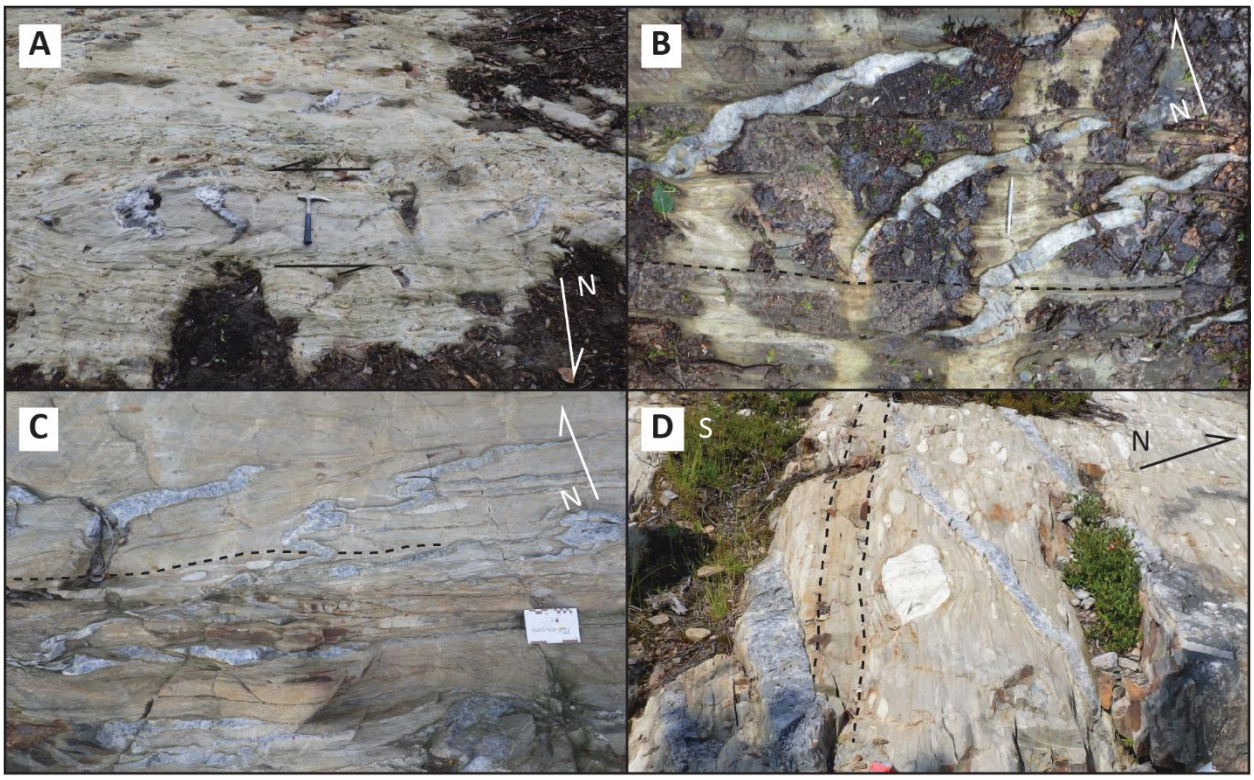

Figure 2.9: (a) S-shaped, sigmoidal V_3 veins on north-younging limb of regional F_1 fold. Hammer (33 cm in length) for scale. (b) S-shaped folded V_4 veins oriented anticlockwise to bedding on north facing limb of regional F_1 fold. Pen magnet (13 cm in length) for scale. (c) S-shaped folded V_4 veins oriented anticlockwise to bedding on south facing limb of regional F_1 fold. Photo card (9 cm in length) for scale. (d) V_4 veins oriented anticlockwise to bedding on south facing limb of regional F_1 fold. Photo card (5 cm in length) for scale in the bottom right hand corner of photograph. Black dashed lines indicate the trace of bedding.

2.4.3 D_3 Deformation Event

D_3 structures overprint all earlier structures. The regional S_1 cleavage and bedding are folded by tight, Z-shaped F_3 folds with an axial planar S_3 cleavage (Fig. 2.10a). F_3 axial planes strike east (~090-094°) and dip steeply to the south (~80°-85°); their fold axes plunge moderately (~60°) to the west (~275°-280°). The S_3 cleavage is oriented anticlockwise to bedding and to the S_1 cleavage on both north-facing and south-facing limbs of regional F_1 folds. It is best expressed in mudstone as a differentiated spaced cleavage defined by white mica and chloritized biotite, alternating with ~0.1 mm thick microlithons of quartz and feldspar. The V_2 and V_4 veins are folded by Z-shaped F_3 folds, which are also present as flanking structures folding bedding and

the S_1 cleavage in the wallrocks of V_4 veins (Fig. 2.10a). Along strike, the veins are deflected in clockwise manner into near-parallelism with bedding and are boudinaged and overprinted by steeply-dipping dextral shear bands (Figs. 2.10b, c), striking ~125° and dipping steeply to the southwest (~85°). In conglomerate, clasts are surrounded by dextral asymmetrical strain shadows (Fig. 2.10d). This feature, together with the presence of dextral shear bands, Z-shaped flanking folds and F_3 drag folds, and boudinage structures along V_4 veins, suggests that D_3 is a dextral transcurrent shearing event.

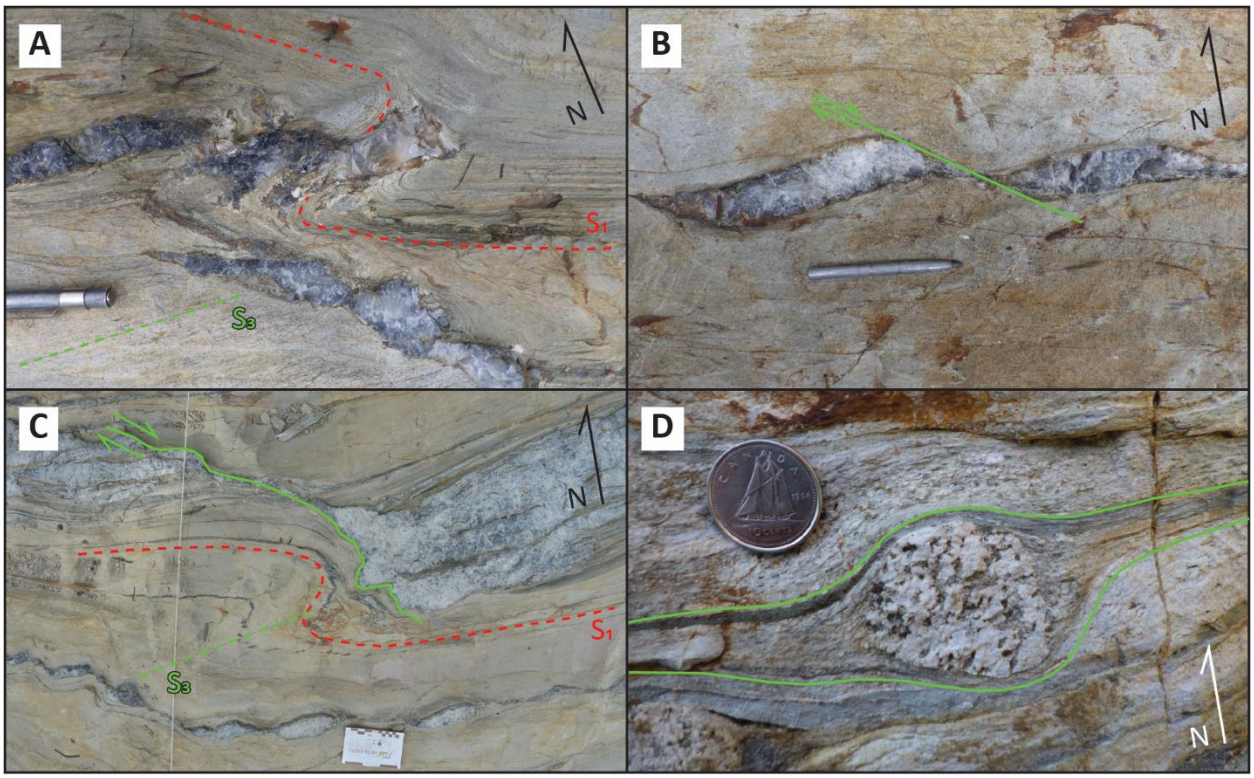

Figure 2.10: Field photographs. (a) Z-shaped F_3 fold flanking V_4 quartz veins. S_3 cleavage is axial planar to the fold. Pen magnet (5 cm in length) for scale. (b) V_4 veins boudinaged and cut by dextral shear bands. Pen scribe point (4 cm in lenth) for scale. (c) Z-shaped F_3 folds overprinting boudinaged V_4 veins cut by dextral shear bands. Photo card (9 cm) for scale. (d) Asymmetrical dextral strain shadows surrounding a clast in conglomerate. Coin (18 mm in diameter) for scale.

2.4.4 D_4 Deformation Event

The D_4 deformation event is characterized by late conjugate brittle fractures and kink bands. Dextral brittle fractures and kink bands strike north and dip steeply to the east (000°/85°);

sinistral brittle fractures and kink bands strike northeast and dip steeply to the southeast (040°/85°). On outcrop, displacements along these fractures are on the scale of a few centimetres, however, on the MRNF aeromagnetic map (D'Amours and Intissar, 2012), magnetic markers are dextrally offset by up to 275 metres along a north-trending fault.

2.5 Gold Mineralization

Gunning and Ambrose (1940) described several gold occurrences located along the southeast-trending Malartic segment of the Cadillac Group, including the Deane Cadillac, Dempsey Cadillac, Hayes Cadillac, Lartic, Mervyn Malartic, Paquette Malartic, Rubec, Sladen Malartic, and Valco Cadillac occurrences. In addition to these occurrences, two gold deposits occur along the inflection points of the Malartic segment of the Cadillac Group including the world-class Canadian Malartic deposit and the Lapa deposit. The two stripped outcrops with multiple vein sets (V_1-V_4), which are described in this paper and shown in Figures 2.7a and 2.7b, are in mining claims originally owned by Dempsey Cadillac Gold Mines Limited and now owned by Midland Exploration Incorporated. The stripped outcrop of Timiskaming conglomerate and sandstone (Fig. 2.7a) is on the site of the former Dempsey Cadillac Gold Mine, where a 275 feet vertical shaft was sunk in 1937 on a mineralized quartz vein hosted by conglomerate (Gunning and Ambrose, 1940). The quartz vein was reported to contain free gold, but mining operations ceased a few months later due to discouraging assay results. Structural overprinting relationships between the veins and the regional cleavage and folds have been described. This section focuses on the mineralogy of the veins, their alteration minerals, and mass changes during alteration.

Of the four generations of veins, V_4 veins only are mineralized. Gold occurs in the veins and their alteration halos. The latter extends continuously over 5 to 10 cm on both sides of the veins.

Away from the veins, the host sandstone consists of quartz, oligoclase, biotite, muscovite, apatite and zircon. In the alteration halo, ferromagnesian minerals become more magnesium rich and the Mg # for biotite, chlorite, and muscovite increase from 40 to 49%, 43 to 51%, and 40 to 47%, respectively. Chlorite replaces biotite, muscovite increases in abundance and grain size, and calcite, tourmaline, and up to 10% arsenopyrite are added. Calcite, chlorite and biotite are found within strain shadows surrounding arsenopyrite grains (Fig. 2.11a). Up to 30% muscovite is present in the strongly-altered wall rock and has been reoriented in the direction of the S_3 cleavage (Fig. 2.11b). The S_3 cleavage is observed to wrap around the competent arsenopyrite grains and euhedral tourmaline is found throughout the altered wall rock (Fig. 2.11c). In the strain shadows surrounding arsenopyrite grains, preserved biotite is being replaced by chlorite (Fig. 2.11d). Arsenopyrite is the most abundant sulphide mineral and often contains inclusions of pyrrhotite, chalcopyrite, sphalerite, and rutile (Fig. 2.12a). Two textural types are found within arsenopyrite grains: an oscillatory zoned texture and a massive texture. Sections of oscillatory zoned textured arsenopyrite are surrounded by the massive textured arsenopyrite (Fig. 2.12b). In addition, back-scattered electron element maps of arsenopyrite show an inverse relationship between arsenic and sulphur (Fig. 2.12c, d). The arsenopyrite grain is zoned with an arsenic-rich core and rim with a sulphur-rich transitional zone. Gold grains occur as inclusions and along grain boundaries of the massive textured and arsenic-rich arsenopyrite (Fig. 2.12b).

Mass gains and losses during alteration of the wall rocks of V_4 veins were calculated using the method of MacLean (1990). Sampling was done across two veins in turbiditic sandstone of the Cadillac Group and one vein in massive sandstone beds of the Timiskaming Group. The coordinates for the locations of these samples and their geochemistry are provided in Table 2. Twenty-centimetre-long transects were cut across the vein wall rocks on one side only of the

veins and were sampled in 5 cm intervals for a total of four samples per vein. They correspond with decreasing distance from the veins to the least-altered, weakly altered, moderately altered, and strongly altered samples. Because sandstones contain variable amount of heavy detrital minerals, such as zircon, apatite, monazite, and may therefore vary in trace element abundance, mass changes are calculated only for major elements and indicator metals using Al_2O_3 as the reference immobile element. The mobility of Al_2O_3 was first assessed using a binary plot of Al_2O_3 versus TiO_2 for all altered samples. Al_2O_3 and TiO_2 have a R-squared correlation factor of 0.96, suggesting that the two elements were immobile during alteration.

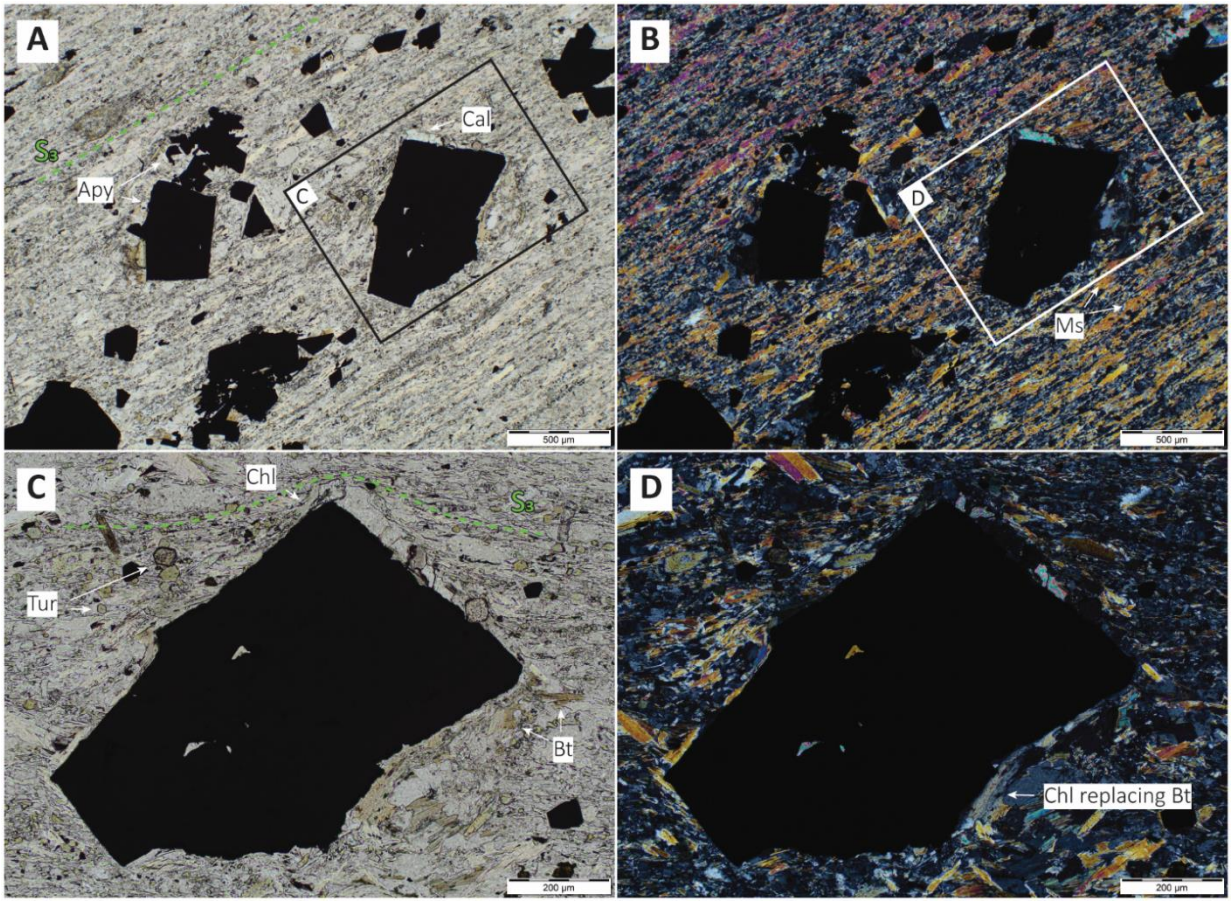

Figure 2.11: Microphotographs of a strongly-altered Cadillac sandstone (sample 407). (a) S_3 cleavage defined by muscovite overprinting arsenopyrite grains. Calcite, chlorite, and biotite are found in the strain shadows of the arsenopyrite. PPL (b) Abundant muscovite defining the S_3 cleavage. XPL (c) Close-up on a arsenopyrite grain. S_3 cleavage is wrapping around the competent arsenopyrite grain. Euhedral tourmaline grains are found throughout the altered sandstone. PPL (d) A pre-existing biotite being replaced by chlorite in the strain shadow of arsenopyrite. XPL. Abbreviations: Apy – arsenopyrite; Cal – calcite; Ms – muscovite; Tur – tourmaline; Chl – chlorite; Bt – biotite.

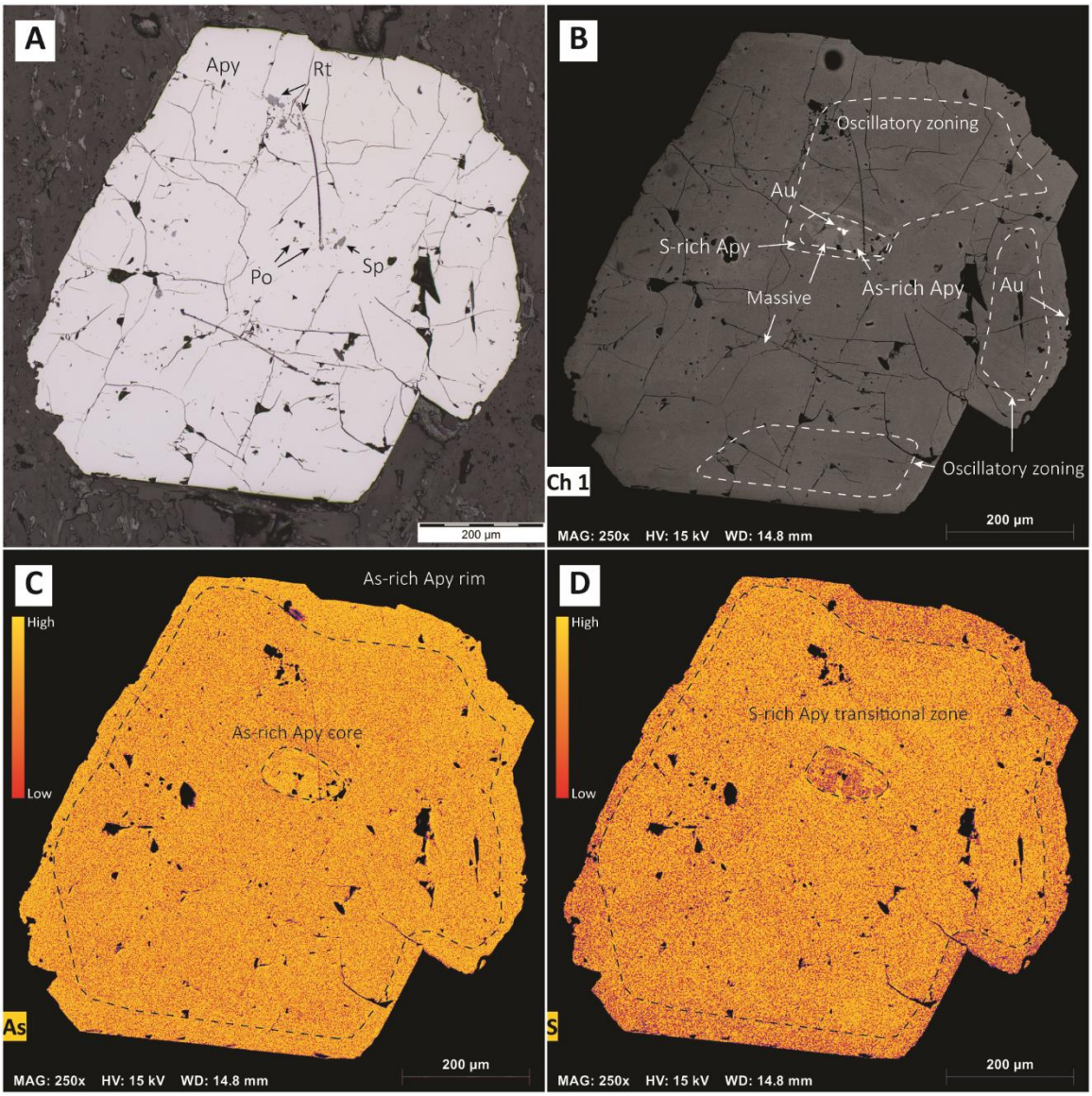

Figure 2.12: (a) Microphotograph of an arsenopyrite grain containing a gold, pyrrhotite, sphalerite and rutile inclusions. Reflected light. (b) Back-scattered electron image of an arsenopyrite grain. The white dashed lines delineate a oscillatory zoned texture and a massive texture found within the arsenopyrite grain. (c) Back-scattered electron element map showing the relative distribution of arsenic within the arsenopyrite grain. An As-rich core and rim are present and delineated by the black dashed lines. (d) Back-scattered electron element map showing the relative distribution of sulphur within the arsenopyrite grain. The S-rich zone is outlined by the black dashed lines. Abbreviations: Apy – arsenopyrite; Rt – rutile; Po – pyrrhotite; Sp – sphalerite.

The results of the mass balance calculations are displayed on % mass change histograms in Figure 2.13. The histograms show that the weakly- and moderately-altered Cadillac sandstones underwent strong mass gains in Sb, C, and moderate mass gains in W, Te, S (Fig. 2.13a). The strongly-altered Cadillac sandstones underwent additional strong mass gains in Bi, Te, Ba, and

also As, which is above detection limits and was not therefore included in the histograms, moderate mass gains in K, and mass loss in Na, Ca, Mn, and Mg. The mass loss in Na and Ca and mass gains in K, Ba and C reflect the breakdown of feldspars and formation of sericite and calcite, whereas the mass loss in Mg is likely due to chloritization of biotite. The latter liberated Fe, which was incorporated in the new sulfide minerals, and Mg, which was partially taken by chlorite and sericite as suggested by their increase in Mg #. Similarly, the Timiskaming sandstones underwent strong mass gains in Bi, Te, Ba, and mass loss in Na and Ca, but differs by their mass gains in Cu and mass loss in C (Fig. 2.13b), possibly reflecting a slightly different alteration fluid chemistry or later modification during D_3 dextral shearing.

Table 2: Concentration data for major elements and trace metal indicators along three transects across altered vein wall rocks.

Sample		252A G03	252A G04	252A G05	252A G06	371A G12	371A G13	371A G14	371A G15	407A G28	407A G29	407A G30	407A G31
Location		07040893E		5341775N		0706376E		5341663N		0708166E		5341143N	
D.f.v.		1-5	6-10	11-15	16-20	1-5	6-10	11-15	16-20	1-5	6-10	11-15	16-20
Alt. Index		Strong	Mod.	Weak	Least	Strong	Mod.	Weak	Least	Strong	Mod.	Weak	Least
Elements	Method												
SiO_2	FUS-ICP	41.90	44.70	62.60	54.00	64.50	66.20	70.20	68.40	39.20	64.60	67.80	67.20
Al_2O_3	FUS-ICP	26.20	23.70	16.20	18.55	16.35	15.50	14.15	13.90	26.10	15.15	14.55	14.85
LOI	FUS-ICP	5.17	4.88	2.63	3.41	2.33	2.17	1.37	1.21	9.17	1.36	1.33	1.39
K_2O	FUS-ICP	5.78	4.23	3.12	3.10	3.38	3.13	2.66	2.65	7.16	1.95	2.71	3.13
Na_2O	FUS-ICP	1.33	2.19	2.98	2.91	1.65	2.06	2.45	2.43	1.41	3.07	2.45	2.19
Ba	FUS-MS	1740	1170	866	836	1205	999	704	775	2990	581	544	811
CaO	FUS-ICP	1.54	2.60	1.98	2.67	1.50	1.70	2.12	1.98	1.07	2.60	1.99	1.60
MgO	FUS-ICP	6.24	6.84	4.10	5.31	2.82	2.88	2.77	2.48	1.23	2.31	2.64	2.50
MnO	FUS-ICP	0.10	0.11	0.07	0.08	0.07	0.07	0.07	0.06	0.02	0.06	0.07	0.06
Fe_2O_3	FUS-ICP	9.35	10.40	6.37	8.09	5.62	5.78	5.34	5.00	10.00	5.69	5.67	5.64
Cu	TD-ICP	1	11	37	3	84	66	46	42	13	54	52	54
Zn	TD-ICP	107	114	60	67	79	86	73	70	38	80	87	90
TiO_2	FUS-ICP	1.02	0.98	0.58	0.78	0.54	0.54	0.51	0.45	0.96	0.52	0.52	0.53
W	FUS-MS	8	4	2	3	19	22	25	23	25	7	4	4
Sb	AR-MS	0.22	0.23	0.29	0.32	0.67	0.72	0.56	0.56	57.10	10.25	1.78	0.96
As	AR-MS	46	67.6	37.4	75.5	250	250	244	186	250	250	250	250
Bi	AR-MS	0.10	0.11	0.13	0.16	0.40	0.38	0.25	0.20	3.53	0.42	0.31	0.33
Pb	TD-ICP	10	15	12	15	14	11	11	11	26	26	22	19
Te	AR-MS	0.02	0.02	0.03	0.03	0.08	0.08	0.03	0.02	0.41	0.10	0.04	0.04
C	LECO	0.02	0.06	0.02	0.01	0.01	0.01	0.01	0.02	0.03	0.02	0.01	0.01
S	LECO	0.005	0.005	0.01	0.01	0.49	0.38	0.33	0.35	3.36	0.75	0.40	0.45
S.G.		2.84	2.89	2.8	2.77	2.78	2.75	2.79	2.76	3.06	2.83	2.69	2.78

Note: Major elements in wt.%; trace elements in ppm; C and S in %; Location, sample 252 location can be found on Figure 2.14. Locations for samples 371 and 407 can be found on Figure 2.7a and b, respectively; D.f.v., distance from vein in centimetres; Alt. Index, relative alteration index; Mod., moderately; LOI, loss on ignition; S.G., specific gravity; FUS-ICP, lithium metaborate and tetraborate fusion ICP; FUS-MS, lithium metaborate and tetraborate fusion ICP-MS; TD-ICP, total four-acid digestion ICP; AR-MS, aqua regia digestion ICP-MS; LECO, combustion by Leco™ induction furnace.

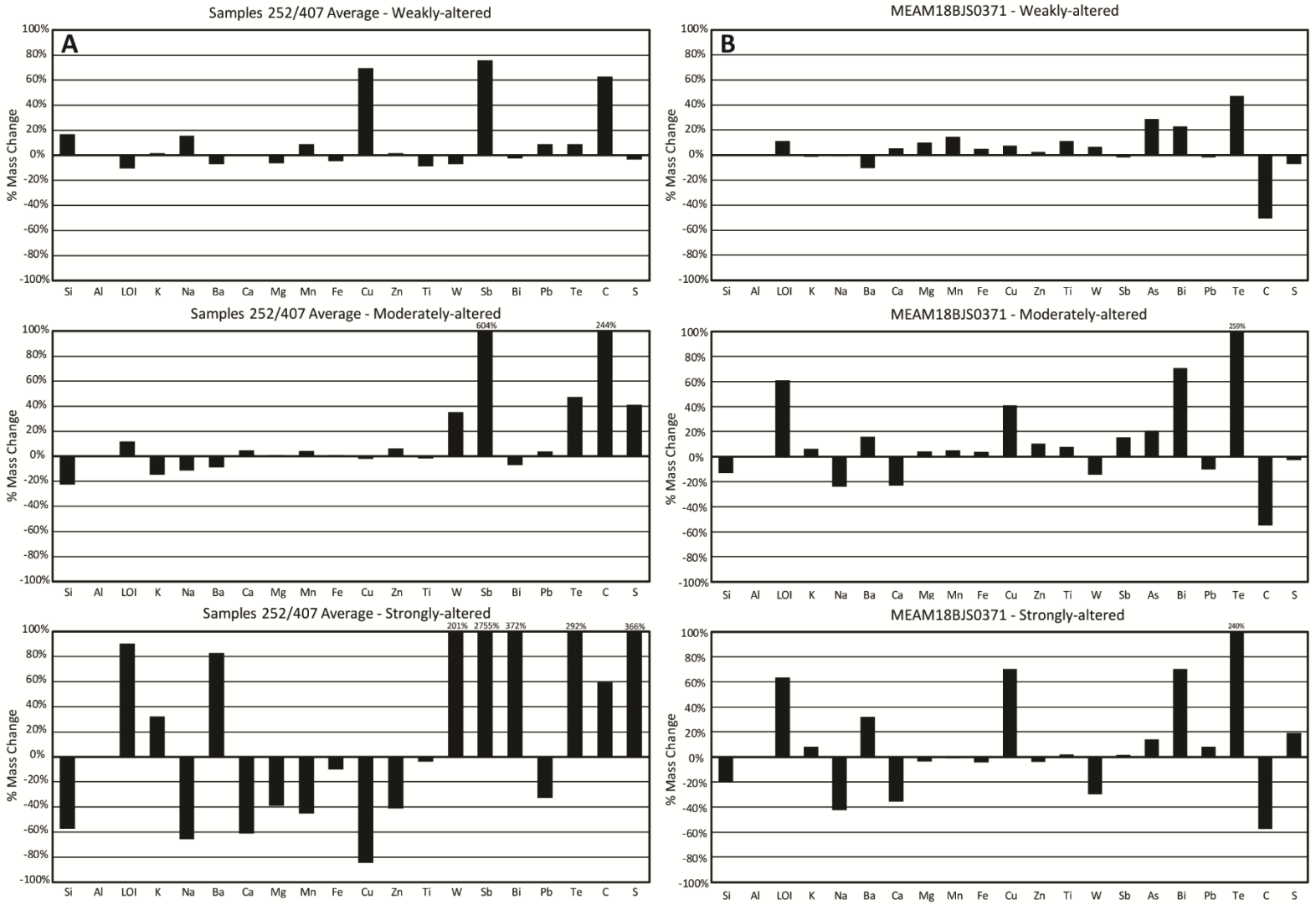

Figure 2.13: Mass change histograms showing calculated elemental gains/losses during hydrothermal alteration. (a) Mass change histograms for the average of two samples obtained from Cadillac sandstone units. (b) Mass change histograms for a sample obtained from Timiskaming sandstone. Histograms are organized so that the mass changes from weakly-altered to strongly-altered are read from top to bottom.

2.6 QFP Intrusion

The QFP intrusion is located along the folded contact between sedimentary rocks of the Cadillac Group and volcanic rocks of the Piché Group on the north limb of a regional F_1 fold. The intrusion truncates bedding in the sedimentary rocks and is folded and overprinted by parasitic F_1 folds and the regional S_1 cleavage (Fig. 2.14).

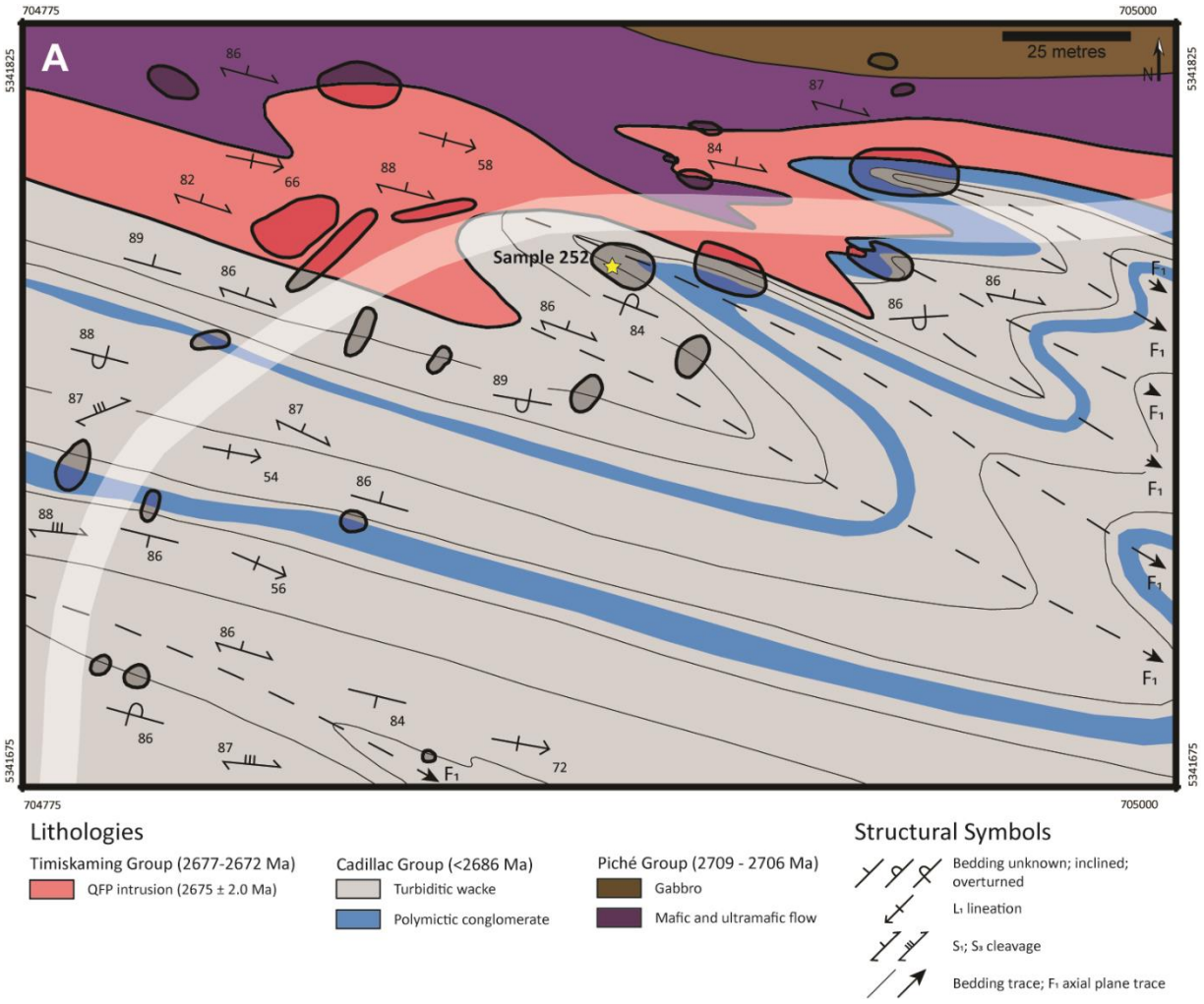

Figure 2.14: Detailed map of the QFP intrusion along the contact between the Piché and Cadillac groups. The QFP intrusion is truncating bedding in sedimentary rocks of the Cadillac Group and is folded by F_1 folds. Thick transparent white line indicates gravel road.

2.6.1 Geochemistry

Six samples of the intrusion were analyzed for major, minor and trace element

concentrations. Major element concentrations vary from 66.2-69.9 wt.% SiO_2, 15.45-16.85 wt.% Al_2O_3, 3.2-5.36 wt.% Na_2O, 2.31-3.45 wt.% Fe_2O_3, 1.33-3.27 wt.% CaO, 1.84-3.13 wt.% K_2O, and 0.98-1.85 wt.% MgO. They plot within the andesite-basalt and the trachy-andesite fields on the Nb/Y vs. Zr/TiO_2 diagram of Winchester and Floyd (1977) (Fig. 2.15a), in the TTG (Tonalite- Trondjhemite-Granodiorite) to granite fields on the Ab-An-Or ternary normative diagram of Barker (1979) (Fig. 2.15b), and in the biotite-two mica granite field on the ternary A/CNK - N/K - FMSB diagram of Laurent et al. (2014) (Fig. 2.15c). They are calc-alkaline ($Zr/Y > 7$; Barrett and MacLean, 1994), peraluminous (molar $Al_2O_3/CaO + Na_2O + K_2O > 1$) with low ferromagnesian oxide contents ($FeO + MgO + MnO + TiO_2$ = 3.39-5.26 wt.%). On the chondrite-normalized REE diagram (Fig. 2.16a), they are enriched in LREE with chondrite normalized La/Yb_{cn} values varying from 26.9-79.93. Extended element patterns normalized to primitive mantle display an enrichment in the more compatible elements, pronounced negative Nb and Ta anomalies, and slightly positive Zr and Hf anomalies (Fig. 2.16b).

2.6.2 U-Pb Geochronology

A sample of the intrusion was dated by U-Pb isotope dilution-thermal ionization mass spectrometry (ID-TIMS) at the Jack Satterly Geochronological Laboratory at the University of Toronto, Canada. Detailed analytical procedures are presented in Appendix A. Isotope analytical results are listed in Table 3 and are summarized below. Analytical uncertainties for the ID-TIMS data are reported at 2σ.

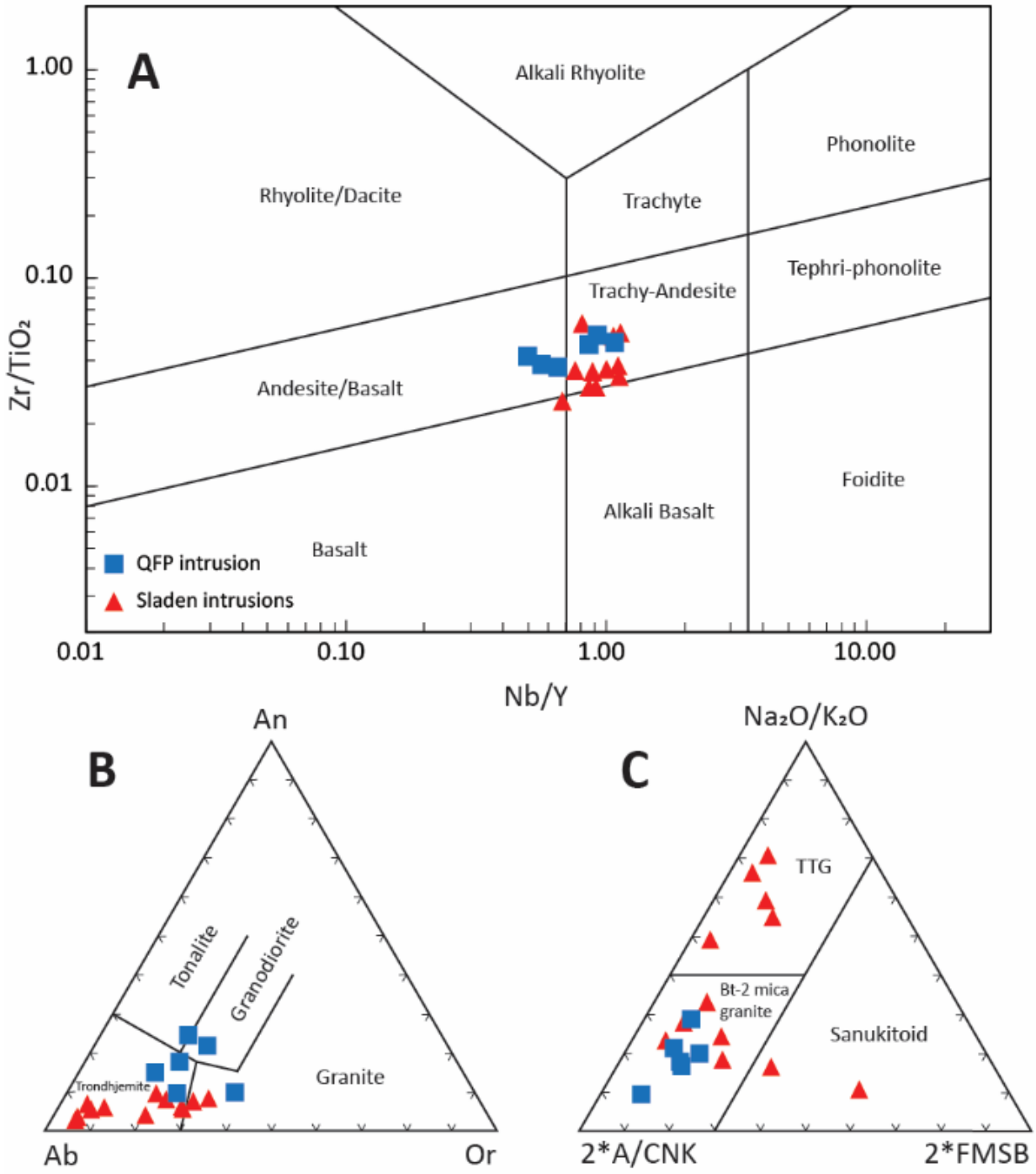

Figure 2.15: Major and trace element discrimination plots for the QFP intrusion (blue squares) at the Cadillac-Piché contact and the Sladen intrusions (red triangles) at the Canadian Malartic mine. (a) Nb/Y vs. Zr/TiO_2 diagram (Winchester and Floyd, 1977). (b) Ab-An-Or ternary normative diagram (Barker, 1979). (c) A/CNK (molar $Al_2O_3/[CaO + Na_2O + K_2O]$) – Na_2O/K_2O – FMSB ([FeO + MgO]wt.% * [Sr + Ba]wt.%) ternary diagram (Laurent et al., 2014). Data for the Sladen intrusions are from Helt (2012). TTG = Tonalite-Trondhjemite-Granodiorite.

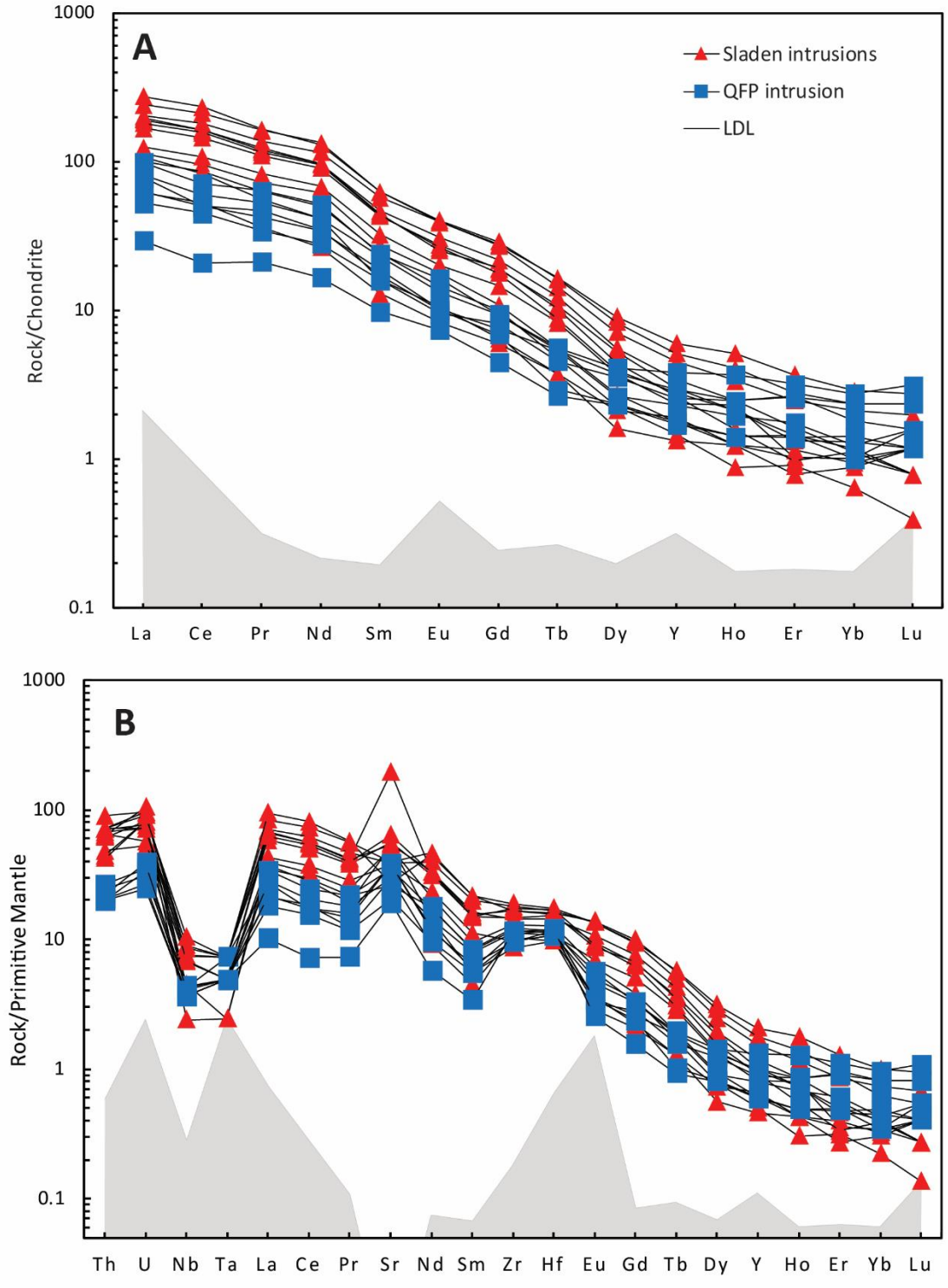

Figure 2.16: Trace element plots for the QFP intrusion (blue squares) at the Cadillac-Piché contact and the Sladen intrusions (red triangles) at the Canadian Malartic mine. (a) Chondrite-normalized REE plot. (b) Primitive mantle-normalized multi-element plot. Chondrite and primitive mantle values are from Sun and McDonough (1989). Data for the Sladen intrusions are from Helt (2012). The shaded area represents values below the detection limit for the respective elements.

Table 3: Zircon U-Pb isotopic data for the QFP intrusion.

Fraction	Description	U (ppm)	Pb^T (pg)	Pb_C (pg)	Th/U	$^{206}Pb/^{204}Pb$	$^{206}Pb/^{238}U$	± 2σ	$^{207}Pb/^{235}U$	± 2σ	$^{207}Pb/^{206}Pb$	± 2σ	Ages (Ma) $^{206}Pb/^{238}U$	± 2σ	$^{207}Pb/^{235}U$	± 2σ	$^{207}Pb/^{206}Pb$	± 2σ	Disc. (%)
18BJS-0404; QFP intrusion																			
Z1	1 med, clr, cls short pr, crk	48	51.72	1.18	0.100	2729	0.514318	0.001200	12.94119	0.03813	0.182491	0.000252	2675.0	5.1	2675.4	2.8	2675.6	2.3	0.0
Z2	1 sm, clr, cls, 2:1 pr	40	22.77	2.52	0.338	547	0.515076	0.001860	19.96105	0.09587	0.182502	0.000954	2678.3	7.9	2676.8	7.0	2675.7	8.7	-0.1
Z3	1 lrg clr, cls, brkn, sharp pr, incl	50	58.40	0.42	0.479	7902	0.520651	0.001112	13.27697	0.03317	0.184949	0.000184	2701.9	4.7	2699.5	2.4	2697.8	1.6	-0.2
Z4	1 sm-med, clr, cls, 2:1 pr, crk	27	14.97	0.87	0.286	1039	0.512262	0.002325	12.88167	0.07420	0.182381	0.000523	2666.3	9.9	2671.0	5.4	2674.6	4.8	0.4

Notes:

All analyzed fractions represent best optical quality (crack-, inclusion-, core-free), fresh (least altered) grains of zircon. Zircons were chemically abraded. Abbreviations: Z - zircon; clr - clear; cls - colourless; crk - cracked, pr - prism/prismatic; sm - small; med - medium; lrg - large; brkn - broken; incl - inclusions. Pb^T is total amount (in picograms) of Pb.

Pb_C is total measured common Pb (in picograms) assuming the isotopic composition of laboratory blank: 206/204 - 18.221; 207/204 - 15.612; 208/204 - 39.360 (errors of 2%). Pb/U atomic ratios are corrected for spike, fractionation, blank, and, where necessary, initial common Pb; 206Pb/204Pb is corrected for spike and fractionation.

Th/U is model value calculated from radiogenic 208Pb/206Pb ratio and 207Pb/206Pb age, assuming concordance. Disc. (%) - per cent discordance for the given 207Pb/206Pb age.

Uranium decay constants are from Jaffey et al. (1971).

On a Concordia plot of four single zircon grain fractions extracted from the sample, three yielded concordant to nearly concordant dates with $^{207}Pb/^{206}Pb$ dates ranging from 2674.6 to 2675.7 Ma. A regression line passing through the origin and the three single zircon data points returned a weighted mean date of 2675.5 ± 2 Ma (93% probability of fit, MSWD = 0.07; Fig. 2.17). The fourth single zircon fraction is concordant but distinctly older at 2698 Ma and is interpreted as a xenocryst from the surrounding metasedimentary rocks. The 2675.5 ± 2 Ma date is interpreted as the best estimate of the crystallization age of the intrusion.

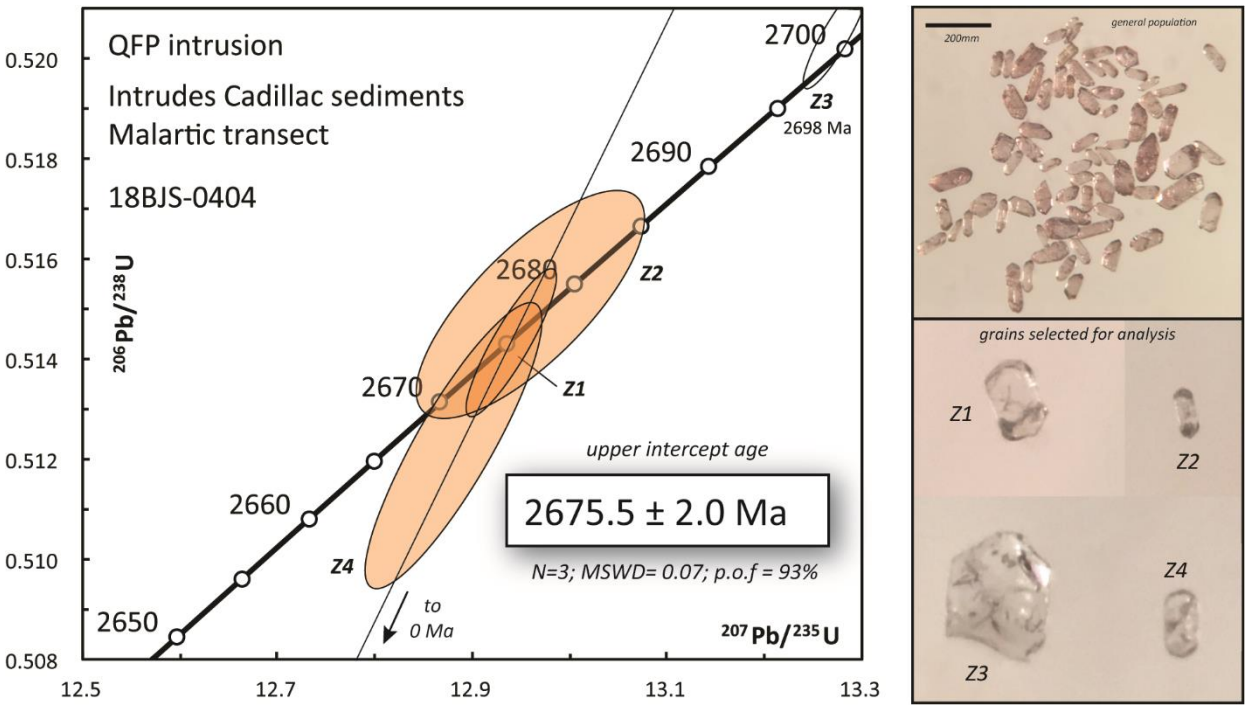

Figure 2.17: Concordia diagram, and associated zircon images, showing U-Pb isotopic data on zircons from sample MEAM18BJS0404AG01, the granodioritic intrusion crosscutting the Cadillac Group metasedimentary rocks and Piché Group metavolcanic rocks. Three concordant to near-concordant overlapping analyses from zircon are shaded in orange. The unshaded ellipse at the upper right in that for the larger, clear grain Z3, represents an inherited zircon.

2.7 Discussion

2.7.1 Structural Implications

Our study of the Cadillac Group along the Malartic segment of the LLCDZ suggests that the sedimentary rocks were deformed during four events. The sequence of events is summarized in

Table 1 and illustrated in Figures 2.18 and 2.19. During the D_1 deformation event, the Cadillac group was tightly folded by regional F_1 folds with an axial planar regional S_1 cleavage and coaxial L_1 stretching lineation. Their strikes and trend are parallel to the structural trend, which is defined on map-scale by the trace of lithologic contacts. During the D_2 deformation event, both limbs of regional F_1 folds were overprinted by steeply-dipping quartz veins (V_3 and V_4) oriented anticlockwise to bedding. As the veins retain the same relative orientation to bedding on both limbs of the folds, this suggests that they were emplaced after the formation of the folds. The veins are important, not only because V_4 veins are gold-bearing, but also because they represent a deformation event that can be correlated across other segments of the LLCDZ. Their anticlockwise orientation relative to bedding, sigmoidal S-shape within sandstone beds, and overprinting by S-shaped drag folds, suggest that they were emplaced as extensional veins parallel to the D_2 shortening direction during sinistral shearing parallel to bedding. Reversal of the shear direction during the D_3 deformation event changed the strain field containing the veins from contractional during the D_2 event to extensional during the D_3 event. This caused the veins to undergo boudinage and back-rotation along dextral shear bands as they rotated in clockwise manner towards bedding. Shear was impeded against some veins resulting in buckling and the formation of Z-shaped flanking folds. On outcrop scale, other Z-shaped F_3 drag folds with an east-striking S_3 cleavage overprint the S_1 cleavage and V_2 to V_4 veins. On map scale, they are represented by macroscopic Z-shaped folds overprinting regional F_1 folds in the Cadillac Group and interleaved volcanic panels of the Malartic Group north of the Cadillac Group. This event further resulted in the gentle Z-shaped flexure represented by the change in orientation of the LLCDZ from east-trending in the Rouyn and Joannes segments, to southeast-trending in the Malartic segment, to east-southeast–trending in the Val-d'Or segment (Fig. 2.2). Late conjugate

D_4 brittle faults and kink bands overprint all structures but their collective strain effect is minimal.

The presence of a major regional F_1 fold in the Cadillac Group was first described by Gunning and Ambrose (1940) who named it the Cadillac syncline. At the past Pan-Canadian mine on the south limb of the syncline, they uncovered the contact between the Piché Group and the Cadillac Group (Fig. 2.6a). They described the contact as structurally conformable because polymictic conglomerate of the Cadillac Group rests directly on volcanic rocks of the Piché Group but lacks the volcanic clasts indicative of an erosional unconformity. Farther west in the Bousquet area, Gorman (1986) described the same Piché-Cadillac contact as an erosional unconformity. On the north limb of the syncline, the contact between the Cadillac Group and Blake River volcanics has been described as conformable (Gunning and Ambrose, 1940; Goulet, 1978; Stone, 1990), as a strained unconformity (Dubé et al., 2007), or as a fault (Tourigny et al. 1988), and is portrayed on the recent map of Pilote (2013) as a fault. The opposing facing directions of the sedimentary rocks on the south flank and north flank of the Cadillac Group, as shown on maps by Gunning and Ambrose (1940), Pilote (2013) and Figure 2.6a in this study, are consistent with the presence of a regional scale syncline on the scale of the Cadillac Group. The polymictic conglomerate horizons observed along the south flank of the Cadillac Group are not present along its north flank. The polymictic conglomerate horizons observed along the south flank of the basin are not present along its north flank, suggesting that they have been removed by faulting consistent with the interpretation of Pilote (2013). Changes in facing directions across the sedimentary rocks further suggest the presence of second-order, southeast-trending, F_1 folds associated with the larger Cadillac syncline. Collectively, the contact relationships, reversals in facing and more than 20 Ma age gap suggest that the Cadillac Group was unconformably

deposited above the older volcanic rocks and then folded and sheared along contact-parallel faults or high-strain zones.

The existence of the Cadillac syncline was questioned by Imreh (1976), Latulippe (1976) and Bouchard (1980) because of the asymmetry in the large scale distribution of units across the fold. As defined by Gunning and Ambrose (1940), the Cadillac syncline was a large structure with a north limb consisting of volcanic rocks of the Blake River and Malartic groups and sedimentary rocks of the Kewagama Group, and a south limb consisting of volcanic rocks of the Piché Group and sedimentary rocks of the Pontiac Group. Thus, the north limb consisted mainly of volcanic rocks that did not correlate with the mainly sedimentary rocks on the south limb of the syncline. Although the presence of a Cadillac syncline on the scale proposed by Gunning and Ambrose (1940) has been refuted, its existence remains valid if applied strictly to the F_1-folded Cadillac Group and unconformably underlying Blake River and Piché volcanic rocks.

In the Canadian Malartic mine area of the Pontiac Group, the presence of F_1 folds is indicated by changing facing directions (Derry, 1939; Sansfaçon et al., 1987; Sansfaçon and Hubert, 1990; Trudel and Sauvé, 1992; De Souza et al., 2015, 2017; Perrouty et al., 2017). A bedding-parallel cleavage defined by white mica is axial planar to those folds. The expression of those structures is best observed in the hinge and short limb of an open S-shaped F_2 fold, which controls the folded geometry of the Pontiac Group sedimentary rocks in the mine area. A northwest-trending S_2 cleavage, which is defined by white mica, biotite and chlorite, is oriented near perpendicular to bedding in the hinge zone and short limb of the F_2 fold, and is oriented clockwise to bedding along the long limb of the fold (Sansfaçon and Hubert, 1990; De Souza et al., 2017*)*. South and west of the mine area, changing facing directions and folded iron formation horizons define regional isoclinal F_1 folds which are overprinted on outcrop- and map-scale by

the S_2 cleavage and S-shaped F_2 folds (Perrouty et al., 2017). A similar cleavage has been reported by Goulet (1978), Dimroth et al. (1983), and Bedeaux et al. (2017) in the Rouyn and Joannes areas. Bedeaux et al. (2017) described a northwest-striking cleavage overprinting an older regional cleavage and isoclinal folds. The cleavage is axial planar to S-shaped folds and is therefore similar in structural association and relative timing to the S_2 cleavage in the Canadian Malartic mine area. Although they dismissed this cleavage as a local feature associated with late brittle faulting, its presence in the Canadian Malartic mine area suggests that it has regional significance. Several decades ago, Hawley (1932) attributed the formation of this cleavage to sinistral bedding-parallel shearing. In the Cadillac and Timiskaming groups, this corresponds to the emplacement of the V_3 and gold-rich V_4 veins during D_2 sinistral shearing. Thus, not only was this deformation event regionally significant, it was also important for the formation of gold deposits as discussed below for the Canadian Malartic and Lapa deposits.

Overprinting of the Cadillac syncline and volcanic rocks of the Malartic area by map-scale Z-shaped folds was first described by Gunning and Ambrose (1940), Dimroth et al. (1983) and Desrochers and Hubert (1996) and attributed to dextral transcurrent shearing (Gunning and Ambrose, 1940; Robert, 1989; Daigneault et al., 2002; Bedeaux et al., 2017; Perrouty et al., 2017). Bedeaux et al. (2017) later suggested that the present geometry of the southern margin of the Abitibi greenstone belt and LLCDZ, which they divided into three east-trending segments (i.e. Rouyn, Joannes, and Val-d'Or), and the southeast-trending Malartic segment, was established during early imbrication of the volcanic Malartic and Blake River groups before the deposition of the younger Timiskaming sequence. They suggested that during post-Timiskaming north-south shortening, an east-striking cleavage formed axial planar to symmetrical regional folds along east-trending segments, and the same cleavage formed axial planar to Z-shaped folds

along the southeast-trending Malartic segment. The cleavage was said to cut across the Cadillac Group along the Malartic segment and to be dragged in clockwise manner along contact-parallel high-strain zones that formed during the same north-south shortening event. This interpretation has important implications and is conceptually interesting because it suggests that the segments of the LLCDZ may have originated as separate early structures that became linked during later tectonic events forming bends, jogs and flexures that controlled the flow of hydrothermal fluids and the emplacement of shear zone-related gold mineralization along the LLCDZ (Bedeaux et al., 2017, 2018).

The latter interpretation differs from that proposed by Gunning and Ambrose (1940), Dimroth et al. (1983) and Desrochers and Hubert (1996) who interpreted the Malartic segment as the short limb of an open Z-shaped flexure that formed late during the evolution of the southern margin of the Abitibi greenstone belt. Our results are consistent with their interpretation. Several lines of evidence suggest that the Malartic segment is a late tectonic flexure rather than an early accretionary structure. First, rock units and their lithological contacts show smooth and gradual changes in orientation from the east-trending Joannes and Val-d'Or segments to the southeast-trending Malartic segment. Second, abrupt changes in lithofacies and in the thickness of units, which would be expected if the segments evolved as separate early accretionary structures, have not been described at bends between east- and southeast-trending segments. Third, across the entire Cadillac and Timiskaming groups, the main cleavage (S_1), which accounts for 92% of all cleavage measurements (Fig. 2.5), is southeast-striking, axial planar to tight southeast-striking folds, and parallel to the trend of the Malartic segment. Thus, similar to the east-trending segments, the main cleavage is oriented parallel to the trend of the segment (i.e. it does not cut across an early accretionary structure). Fourth, the main S_1 cleavage is overprinted by an east-

striking cleavage (S_3) which is axial planar to the Z-shaped folds. The latter are therefore late structures overprinting the Malartic segment. Fifth, a similar sequence of structures occurs along all segments, that is, early segment-parallel folds and a regional cleavage are overprinted by S-shaped folds with an axial planar cleavage and sigmoidal S-shaped extensional quartz veins, which are in turn overprinted by Z-shaped folds with an axial plane cleavage and associated dextral shear indicators (See Table 1). The main difference amongst all segments is the change in orientation of structures along the Malartic segment due to clockwise rotation of the segment during late gentle Z-shaped folding.

2.7.2 Magmatic and tectonic interpretation of the Cadillac Group

The QFP intrusion along the contact between the Piché and Cadillac groups is comparable in geochemistry to the Sladen intrusions, which straddle the contact between the Piché and Pontiac groups in the Canadian Malartic mine area. Helt et al. (2014) and De Souza et al. (2017) describe the Sladen intrusions as sub-alkaline to alkaline quartz-monzodiorite and granodiorite. On Winchester and Floyd (1977)'s diagram, the Sladen intrusions and the QFP intrusion both plot tightly in the trachy-andesite field (Fig. 2.15a). On the ternary normative Ab-An-Or diagram and the ternary A/CNK - N/K - FMSB diagram of Barker (1979) and Laurent et al. (2014), respectively, the Sladen intrusions show more variable compositions and scatters than the QFP intrusion presumably due to alkali mobility during hydrothermal alteration (Figs. 2.15b, c). Their REE and extended element patterns overlap (Figs. 2.16a, b), and the 2675.5 ± 2 Ma U-Pb zircon age of the QFP intrusion (Fig. 2.17) is within error of the ca. 2678–2677 Ma U-Pb zircon ages of the Sladen intrusions (De Souza et al., 2014), suggesting that they are part of the same Timiskaming-age magmatic event.

The ca. 2675 Ma QFP intrusion provides a minimum age for the deposition of the Cadillac

Group and a maximum age for its subsequent ductile reworking and formation of the Cadillac syncline. The early structural history of the Malartic segment is depicted in Figure 2.18. Deposition of the Cadillac Group and Pontiac Group over a Piché-Blake River volcanic substrate began after ca. 2686 Ma (Stage 1 in Fig. 2.18), which is the age of the youngest detrital zircons in both groups (Davis, 2002). The Pontiac Group correlates in age with the Cadillac Group and consists of similar turbidite lithofacies suggesting that they represent a single depositional sequence. However, as discussed by Frieman et al. (2017), the Porcupine assemblage (i.e. the Cadillac Group) contains locally derived zircon populations, whereas the Pontiac Group contains more abundant older zircons suggesting they were derived from a more distal source. The Cadillac Group faces away and is in strained unconformable contact with the Piché Group (Gunning and Ambrose, 1940; Gorman, 1986), whereas the Pontiac Group generally faces towards and is in fault contact with the Piché Group (Pilote, 2013). Their juxtaposition by faulting predate the emplacement of the ca. 2678–2677 Ma Sladen intrusions across the Pontiac-Piché contact (Bedeaux et al., 2017, 2018). Thus, we suggest that low-angle thrusting transported the Piché and Cadillac groups above the Pontiac Group prior to the emplacement of the stitching Sladen intrusions (Stage 2 in Fig. 2.18). This event may correspond to an early ductile deformation that affected the Cadillac Group (Bouchard, 1980) and the Pontiac Group (Goulet, 1978; Dimroth et al., 1983) prior to the deposition of the Timiskaming Group. The Sladen and QFP intrusions are similar in age to the ca. 2677–2672 Ma Timiskaming Group (David et al., 2018; Davis, 2002), further suggesting that the emplacement of the intrusions along the pre-existing thrust fault was largely coeval with the deposition of the Timiskaming Group at ≤ 2675 Ma (Stage 3 in Fig. 2.18; Bedeaux et al., 2017, 2018). Post-Timiskaming shortening (D_1) folded these rocks into tight regional F_1 folds with steeply dipping limbs (Stage 4 in Fig. 2.18). Folding

of the Piché volcanic rocks beneath the Cadillac Group (Fig. 2.6b) is signalled by a large magnetic anomaly on the MRNF aeromagnetic map (D'Amours and Intissar, 2012) extending southeastward from the folded QFP–Piché contact or hinge zone shown in Figure 2.6a. During the same event, contacts between the Piché Group and adjacent Pontiac and Cadillac groups were reactivated or strained, resulting in the development of a strong contact-parallel foliation. Subsequent shearing during the D_2 deformation event, developed a northwest-trending cleavage in the Joannes segment, emplaced the gold-bearing V_4 quartz veins in the Cadillac and Timiskaming groups, reactivated the Piché-Pontiac contact in the Canadian Malartic mine area (De Souza et al., 2017; Perrouty et al., 2017), and emplaced mineralization at ca. 2664 Ma (Re-Os molybdenite age; De Souza et al., 2014) along northwest-trending high strain shear zones in the hinge of a mine-scale S-shaped fold and along the east-trending Sladen Fault (Stage 5 in Fig. 2.19). Late dextral shearing during the D_3 deformation event resulted in the formation of Z-shaped drag folds that rotated the Malartic segment clockwise into its present orientation (Stage 6 in Fig. 2.19).

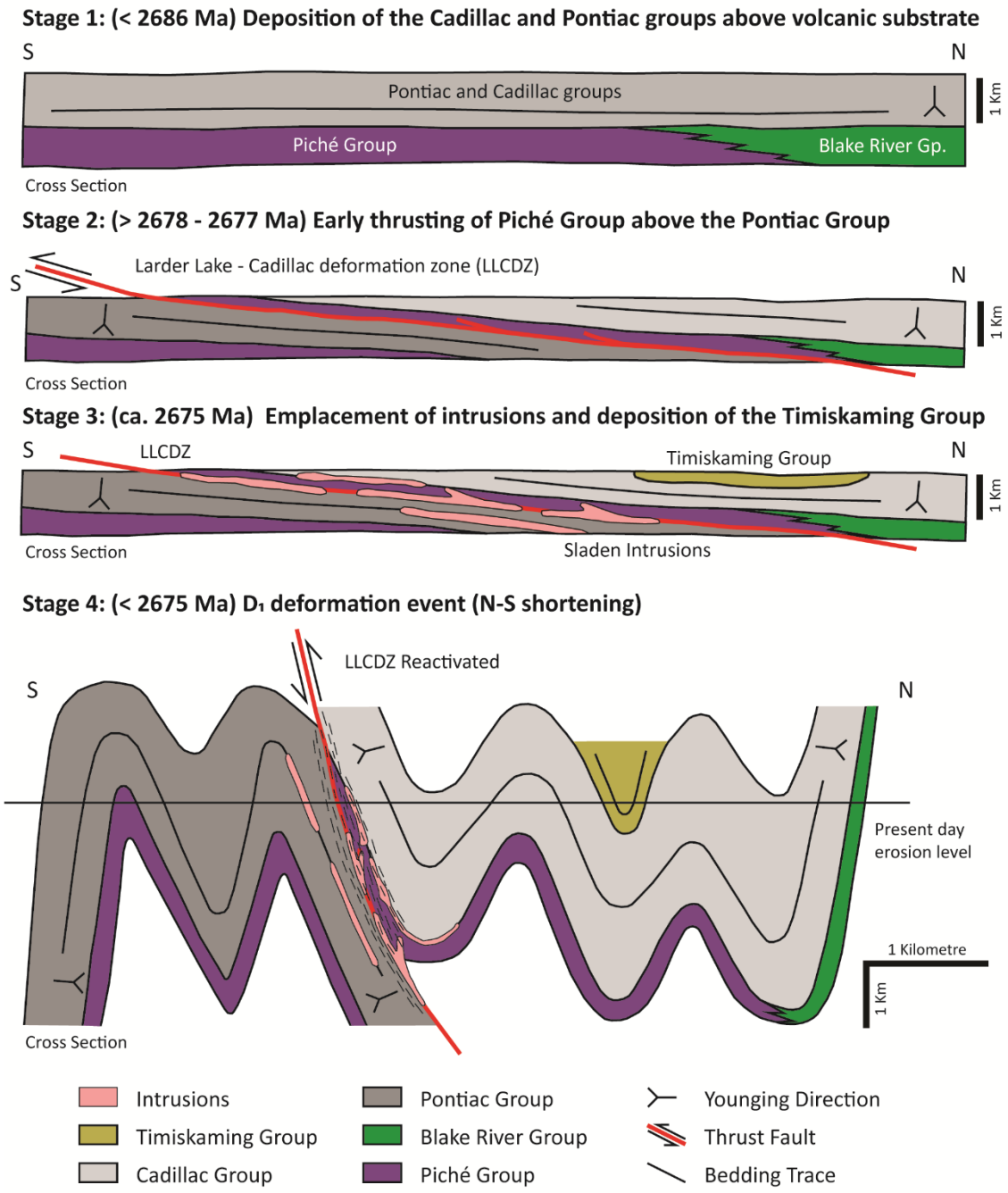

Figure 2.18: Stages 1 to 4 of the structural evolution model for the Malartic segment of the LLCDZ. Cross-section view.

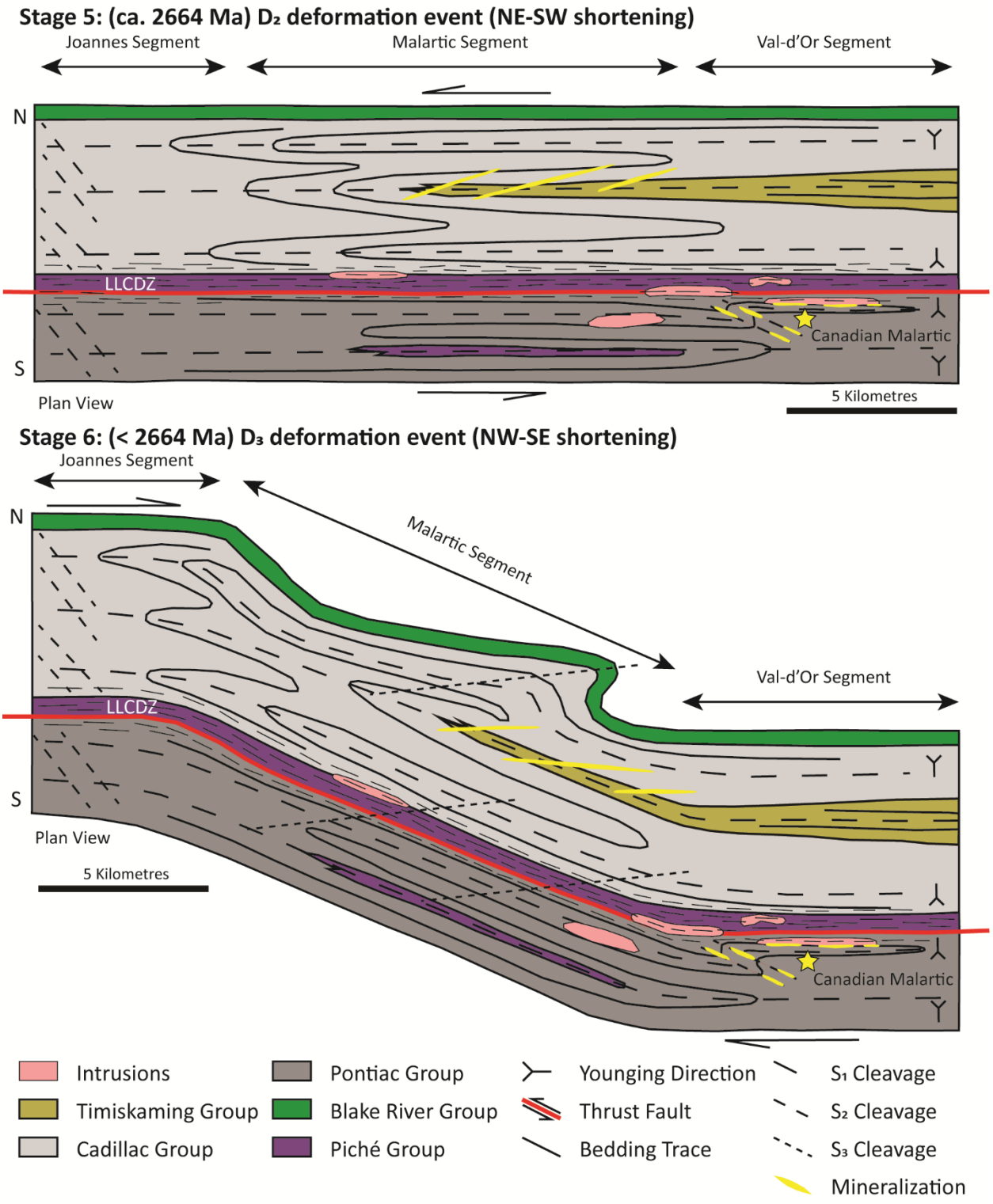

Figure 2.19: Stages 5 and 6 of the structural evolution model for the Malartic segment of the LLCDZ. Plan view.

2.7.3 Comparison with the Canadian Malartic and Lapa gold deposits

The Canadian Malartic gold deposit produced 5.1 Moz of gold at an average grade of 3.37 g/t Au as an underground mine (Trudel and Sauvé, 1992) and is currently in production as an open pit operation mining the low-grade disseminated gold footprint (~1 g/t Au). It consists of disseminated pyrite and quartz-carbonate vein stockwork mineralization spatially associated with sub-alkaline to alkaline quartz-monzodiorite and granodiorite of the ca. 2678–2677 Sladen intrusive suite (Sansfaçon et al., 1987; Trudel and Sansfaçon, 1987; Trudel and Sauvé, 1992; Desrochers and Hubert, 1996; Helt et al., 2014; De Souza et al., 2015, 2017; Perrouty et al., 2017). Helt et al. (2014) interpreted the deposit as an oxidized intrusion-related gold deposit based on the association of the ore zones with extensive potassic biotite and microcline alteration, the Au-Te-W-Bi metal signature of the ore zones, the spatial association of the ore zones with intrusions and, although later disputed by Beaudoin and Raskevicius (2014), the oxygen, hydrogen and sulphur isotope composition of the ore fluids. They suggested that magmatic-hydrothermal ore fluids exsolved from crystallizing monzodioritic magmas at depth, migrated upwards along structural conduits previously used by the Sladen intrusions, and altered these intrusions. The Sladen intrusions were thought to be emplaced during the D_2 deformation event suggesting that gold mineralization was also syn-D_2. De Souza et al. (2015, 2017) emphasized the mutually overprinting relationships between the gold-bearing veins and the S_2 cleavage, the close association between ore shells and the Sladen fault which cut across the Sladen intrusions and reactivated the Pontiac-Piché contact, and suggested that most of the ore was orogenic and syn-D_2 and was remobilized from, or superimposed on, a wider magmatic-hydrothermal gold system associated with the Sladen intrusions.

The Lapa gold deposit produced 1.15 Moz of gold at an average grade of 5.31 g/t Au (Mercier-Langevin et al., 2017) as an underground mine from 2009 to 2018. The deposit is located at the inflection point where the LLCDZ changes from an east-trending orientation to a southeast-trending orientation (Fig. 2.2). The ore zones at the Lapa deposit are roughly east-trending and subvertical, and parallel to the main foliation and contact between the Piché and Cadillac groups (Mercier-Langevin et al., 2017). It consists of finely disseminated arsenopyrite and quartz-carbonate vein mineralization spatially associated with Fe-rich mafic and ultramafic host rocks of the Piché Group and minor sedimentary rocks of the Cadillac Group (Simard et al., 2013). Gold is bound within the crystal lattice of arsenopyrite which was deposited during the development of the main east-trending S_1 cleavage (Simard et al., 2013). It was then partially remobilized and precipitated as native gold during the formation of a northeast-trending S_3 cleavage axial planar to regional Z-shaped folds (Simard et al., 2013). The ore zones at the Lapa deposit have a Au-As-Sb metal signature and are associated with a proximal biotite alteration and minor muscovite alteration (Simard et al., 2013).

The gold-bearing V_4 veins at the Dempsey-Cadillac mine and elsewhere within the Cadillac Group are similar in Bi, Te ± W metallic signature to the veins at the Canadian Malartic deposit. However, they differ in alteration mineralogy and mass changes. At Canadian Malartic, the veins within turbiditic sandstone are surrounded by alteration halos of Na- and K-feldspar, biotite ± pyrite ± carbonate associated with strong mass gains in K, S, and Ca, and consistent mass loss in Mg (Helt et al., 2014; De Souza et al., 2017). This differs from the V_4 veins which lack the strong potassic alteration present at Canadian Malartic and have arsenopyrite rather than pyrite as the dominant sulfide mineral. On the other hand, they have similar structural chronology. Both V_4 veins and Canadian Malartic veins overprint early regional F_1 folds and S_1 cleavage and are in

turn overprinted by a late northeast-trending S_3 cleavage (De Souza et al. 2017; Perrouty et al., 2017). The Canadian Malartic veins were emplaced during the formation of S-shaped folds and their northwest-trending, axial planar cleavage, which is consistent with sinistral shearing during the formation of the V_4 veins. Thus, we suggest that the V_4 and Canadian Malartic veins were emplaced during the same D_2 deformation event but from different fluid sources as indicated by their different alteration mineralogy and chemistry.

The Au-As-Sb metal signature of mineralized zones at the Lapa deposit and their association with arsenopyrite are similar to those of the mineralized V_4 veins in the study area but they differ by the strong proximal biotite alteration and mass gains in K present at the Lapa deposit (Simard et al., 2013). Gold mineralized zones at the Lapa deposit are oriented parallel to the main foliation which correspond to the S_1 cleavage in the study area. Because the V_4 veins cut across the S_1 cleavage, this suggests that gold mineralization at the Lapa mine predates the emplacement of the mineralized V_4 veins in the study area.

2.8 Conclusions

To conclude, the structural interpretation presented here for the Cadillac Group provides a framework for interpreting the tectonic evolution of the Malartic segment of the LLCDZ and the emplacement of gold mineralization in these rocks. The main contributions of the paper are:

(1) A new crystallization age of 2675.5 ± 2 Ma for a QFP intrusion straddling the contact between the Piché and Cadillac groups provides a minimum age for the deposition of the Cadillac Group, and a maximum age for ductile deformation of the Cadillac Group.

(2) Ductile structures and fabrics in the Cadillac Group along the Malartic segment of the LLCDZ formed during four deformation events. The deformation of the sedimentary

rocks began during an early D_1 event with regional isoclinal folding and the formation of a regional cleavage and stretching lineation oriented parallel to the trend of the Malartic segment. D_1 was followed by a D_2 event characterized by sinistral shearing and the emplacement of gold-bearing quartz veins. The D_3 event was associated with dextral shearing and the formation of Z-shaped folds with an axial planar cleavage oriented oblique to the trend of the Malartic segment. The D_4 event corresponds to late kinking and brittle crossfaulting. These structures correlate with similar generations of cleavages, folds, and shear zones along the other segments of the LLCDZ.

(3) The southeast trend of the Malartic segment was established late during the tectonic evolution of the Abitibi greenstone belt as a result of Z-shaped folding of the LLCDZ during the D_3 deformation event. It did not originate as a separate accretionary structure that became linked to contiguous east-trending segments later during the tectonic evolution of the LLCDZ and the belt.

(4) Gold-bearing veins in the Cadillac and Timiskaming groups were emplaced during the same D_2 deformation event as the mineralized veins at the Canadian Malartic deposit. They differ in alteration mineralogy and geochemistry suggesting different sources for the mineralizing fluids. Mineralization at the Lapa deposit is similar in metal signature (Au-As-Sb) and arsenopyrite association to the gold-bearing veins in the Cadillac and Timiskaming groups but they differ in structural timing.

2.9 References

Ayer, J.A., Thurston, P.C., Bateman, R., Dubé, B., Gibson, H.L., Hamilton, M.A., Hathway, B., Hocker, S.M., Houlé, M.G., Hudak, G., Ispolatov, V.O., Lafrance, B., Lesher, C.M.,

MacDonald, P.J., Péloquin, A.S., Piercey, S.J., Reed, L.E., and Thompson, P.H., 2005, Overview of results from the Greenstone Architecture Project: Discover Abitibi Initiative: Ontario Geological Survey Open File Report 6154, 146 p.

Barker, F., 1979, Trondhjemite: Definition, Environment and Hypotheses of Origin: Developments in Petrology, v. 6, p. 1–12.

Barrett, T.J., and MacLean, W.H., 1994, Chemostratigraphy and hydrothermal alteration in exploration for VHMS deposits in greenstone and younger volcanic rocks, in Lentz, D.R. (Ed.), Alteration and Alteration Processes associated with Ore-forming Systems 11. Geological Association of Canada, Short Course Notes, p. 433–467.

Beaudoin, G., and Raskevicius, T., 2014, Constraints on the genesis of the Archean oxidized, intrusion-related Canadian Malartic gold deposit, Quebec, Canada—a discussion: Economic Geology, v. 109, p. 2067–2068.

Bédard, J.H., 2018, Stagnant lids and mantle overturns: Implications for Archean tectonics, magmagenesis, crustal growth, mantle evolution, and the start of plate tectonics: Geoscience Frontiers, v. 9, p. 19–49.

Bedeaux, P., Pilote, P., Daigneault, R., and Rafini, S., 2017, Synthesis of the structural evolution and associated gold mineralization of the Cadillac Fault, Abitibi, Canada: Ore Geology Reviews, v. 82, p. 49–69.

Bedeaux, P., Mathieu, L., Pilote, P., Rafini, S., and Daigneault, R., 2018, Origin of the Piché Structural Complex and implications for the early evolution of the Archean crustal-scale Cadillac – Larder Lake Fault Zone, Canada: Canadian Journal of Earth Sciences, v. 55, p.

905–922.

Bell, L.V. and Bell, A.M., 1931, Bell River Headwaters Area – Detailing the Pacalis-Louvicourt Gold Deposits, Abitibi County: Que. Bur. Mines, Ann. Rept., 1931, pt. B, p. 59–123.

Benn, K., Miles, W., Ghassemi, M., and Gillet, J., 1994, Crustal structure and kinematic framework of the northwestern Pontiac Subprovince, Quebec: an integrated structural and geophysical study: Canadian Journal of Earth Sciences, v. 31, p. 271–281.

Bleeker, W., 2012, Lode gold deposits in ancient deformed and metamorphosed terranes: The role of extension in the formation of Timiskaming basins and large gold deposits, Abitibi greenstone belt—a discussion: Ontario Geological Survey Open File Report 6280, p. 47-1–47-12.

Bleeker, W., and Parrish, R.R., 1996, Stratigraphy and U–Pb geochronology of Kidd Creek: implications for the formation of giant volcanogenic massive sulphide deposits and the tectonic history of the Abitibi greenstone belt: Canadian Journal of Earth Sciences, v. 33, p. 1213–1231.

Born, P., 1995, A sedimentary basin analysis of the Abitibi greenstone belt in the Timmins area, northern Ontario, Canada: Unpublished Ph.D. thesis, Ottawa, ON, Carleton University, 489 p.

Bouchard, M.-F., 1980, Région de Cadillac – Malartic: MER Rapport Intérimaire DPV-791, 10 p.

Calvert, A.J., Ludden, J.N., 1999, Archean continental assembly in the southeastern Superior

Province of Canada, Tectonics, v. 18, p. 412–429.

Cameron, E.M., 1993, Precambrian gold: Perspectives from the top and bottom of shear zones: Canadian Mineralogist, v. 31, p. 917–944.

Camiré, G.E., Burg, J.P., 1993, Late Archaean thrusting in the northwestern Pontiac Subprovince, Canadian Shield: Precambrian Research, v. 61, p. 51–66.

Card, K.D., 1990, A review of the Superior Province of the Canadian Shield, a product of Archean accretion: Precambrian Research, v. 48, p. 99–156.

Corfu, F., Krogh, T.E., Kwok, Y.Y., and Jensen, L.S., 1989, U-Pb zircon geochronology in the southwestern Abitibi greenstone belt, Superior Province: Canadian Journal of Earth Sciences, v. 26, p. 1747–1763.

Corfu, F., Spooner, E.T.C., and Barrie, C.T., 1993, The evolution of the southern Abitibi greenstone belt in light of precise U–Pb geochronology: Economic Geology, v. 88, p. 1323–1340.

Daigneault, R., Mueller, W.U., and Chown, E.H., 2002, Oblique Archean subduction: Accretion and exhumation of an oceanic arc during dextral transpression, Southern Volcanic zone, Abitibi Subprovince, Canada: Precambrian Research, v. 115, p. 261–290.

D'Amours, I., and Intissar., 2012, Levé magnétique héliporté dans le secteur de Malartic, Abitibi: Ministère des Ressources naturelles et de la Faune du Québec. DP 2012-04.

David, J., Pilote, P., Hammouche, H., Leclerc, F., and Talla Takam, F., 2018, Datations U–Pb dans la Province du Supérieur effectuées au GEOTOP en 2013-2014: Ministère de

l'Énergie et des Ressources naturelles, Québec. RP 2017-03.

Davis, D.W., 2002, U-Pb geochronology of Archean metasedimentary rocks in the Pontiac and Abitibi Subprovinces, Quebec, constraints on timing, provenance and regional tectonics: Precambrian Research, v. 115, p. 97–117.

Derry, D.R., 1939, The geology of the Canadian Malartic gold mine, N. Quebec: Economic Geology, v. 34, p. 495–523.

De Souza, S., Dubé, B., McNicoll, V., Dupuis, C., Mercier-Langevin, P., and Creaser, R., 2014, Fracture-controlled hydrothermal alteration at the Canadian Malartic deposit: Toward a multiphase model for Archean intrusion related low-grade bulk tonnage gold deposits [abs.]: Geological Association of Canada – Mineralogical Association of Canada, Joint Annual Meeting, Fredericton, Canada, 2014, Abstracts, v. 37, p. 70.

De Souza, S., Dubé, B., McNicoll, V.J., Mercier-Langevin, P., Creaser, R.A., and Kjarsgaard, I.M., 2015, Geology, hydrothermal alteration, and genesis of the world-class Canadian Malartic stockwork-disseminated Archean gold deposit, Abitibi, Quebec: Geological Survey of Canada Open File Report 7852, p. 113–126.

De Souza, S., Dubé, B., McNicoll, V., Dupuis, C., Mercier-Langevin, P., Creaser, R.A., and Kjarsgaard, I., 2017, Geology and hydrothermal alteration of the world-class Canadian Malartic gold deposit: Genesis of an Archean stockwork-disseminated gold deposit in the Abitibi greenstone belt: Reviews in Economic Geology, v. 19, p. 263–291.

Desrochers, J.P., and Hubert, C., 1996, Structural evolution and early accretion of the Archean Malartic composite block, southern Abitibi greenstone belt, Quebec, Canada: Canadian

Journal of Earth Sciences, v. 33, p. 1556–1569.

Dimroth, E., Imreh, L., Rocheleau, M., and Goulet, N., 1983, Evolution of the south-central part of the Archean Abitibi Belt, Quebec. Part I: Stratigraphy and paleogeographic model: Canadian Journal of Earth Sciences, v. 19, p. 1729–1758.

Dubé, B., and Gosselin, P., 2007, Greenstone-hosted quartz-carbonate vein deposits, in Goodfellow, W.D., ed., Mineral deposits of Canada: A synthesis of major deposit-types, district metallogeny, the evolution of geological provinces, and exploration methods: Mineral Deposits Division, Geological Association of Canada, Special Publication no. 5, p. 49–73.

Dubé, B., Mercier-Langevin, P., Hannington, M.D., Lafrance, B., Gosselin, P., and Gosselin, G., 2007, The LaRonde Penna world-class Au-rich volcanogenic massive sulfide deposit, Abitibi, Québec: Mineralogy and geochemistry of alteration and implications for genesis and exploration, Economic Geology, v. 102, p. 633–666.

Frieman, B., Kuiper, Y., Kelly, N., Monecke, T., Kylander-Clark, A., 2017, Constraints on the geodynamic evolution of the southern Superior Province: U-Pb LA-ICP-MS analysis of detrital zircon in successor basins of the Archean Abitibi and Pontiac subprovinces of Ontario and Quebec, Canada: Precambrian Research, v. 292, p. 398–416.

Gerstenberger, H., and Haase, G., 1997, A highly effective emitter substance for mass spectrometric Pb isotope ratio determinations: Chemical Geology, v. 136, p. 309–312.

Gorman, B.E., 1986, District de Bousquet-Cadillac. *In*: Structure and Gold, Rouyn to Val-d'Or, Québec; textes réunis par C. Hubert et F. Robert. Association géologique du Canada;

Excursion 14.

Goulet, N., 1978, Stratigraphy and Structural Relationships across the Cadillac–Larder Lake fault, Rouyn–Beauchastel Area, Quebec: Queen's University, 141 p.

Goutier, J., 1997, Géologie de la région de Destor (SNRC 32D/07-200-0201): Ministère des Ressources naturelles, Québec, Report RG 96-13, 37 p.

Gunning, H.C., and Ambrose, J.W., 1939, The Timiskaming–Keewatin problem in the Rouyn–Harricanaw region, northwestern Quebec: Transactions of the Royal Society of Canada, Section IV, p. 19–49.

Gunning, H.C., and Ambrose, J.W., 1940, Malartic area, Quebec: Geological Survey of Canada Memoir 222, 142 p.

Hawley, J.E., 1932, Granada Gold Mine and Vicinity, Rouyn Township, Temicamingue County. Que. Bur. Mines, Ann. Rept., pt. B, pp. 3–57.

Helt, K.M., 2012, The Canadian Malartic Deposit: an example of oxidized intrusion-related gold mineralization in the Abitibi greenstone belt, Quebec, Canada: McGill University, 171 p.

Helt, K.M., Williams-Jones, A.E., Clark, J.R., Wing, B.A., and Wares, R.P., 2014, Constraints on the genesis of the Archean oxidized, intrusion-related Canadian Malartic gold deposit, Quebec, Canada: Economic Geology, v. 109, p. 713–735.

Hewitt, D.F., 1963, The Timiskaming Series of the Kirkland Lake area. Canadian Mineralogist, v. 7, p. 497–522.

Hodgson, C.J., and Hamilton, J.V., 1989, Gold mineralization in the Abitibi greenstone belt:

End-stage result of Archean collisional tectonics?: Economic Geology Monograph 6, p. 86–100.

Hubert, C., 1990, Geologic framework, evolution and structural setting of gold and base metal deposits of the Abitibi greenstone belt, Canada: University of Western Australia, Short Course Notes, Publication 24, p. 53–62.

Hubert, C., Trudel, P., Gelinas, L., 1984, Archean wrench fault tectonics and structural evolution of the Blake River group, Abitibi belt, Quebec: Canadian Journal of Earth Sciences, v. 21, p. 1024.

Hyde, R.S., 1980, Sedimentary facies in the archean Timiskaming Group and their tectonic implications, Abitibi Greenstone-Belt, Northeastern Ontario, Canada: Precambrian Research, v. 12, p. 161–195.

Imreh, L., 1976, Nouvelle lithostratigraphie à l'ouest de Val-d'Or et son incidence gîtologique: Ministère des Richesses Naturelles du Québec, report DPV 349, 73 p.

Imreh, L., 1984, Sillon de la Motte-Vassan et son avant-pays meridional; synthese volcanologique, lithostratigraphique et gitoligique. *In:* The La Motte-Vassan Structure and its southern foreland; volcanologic, lithostratigraphic and economic synthesis; Ministère des Naturelles du Québec, MM 82-04, 72 p.

Ispolatov, V., Lafrance, B., Dubé, B., Creaser, R., and Hamilton, M., 2008, Geologic and structural setting of gold mineralization in the Kirkland Lake- Larder Lake gold belt, Ontario: Economic Geology, v. 103, p. 1309–1340.

Jaffey, A.H., Flynn, K.H., Glendenin, L.E., Bentley, W.C., and Essling, A.M., 1971, Precision measurement of the half lives and specific activities of ^{235}U and ^{238}U: Physical Review C, v. 4, p. 1889–1906.

Jensen, L.S., 1978, Archean komatiitic, tholeiitic, calc-alkalic and alkalic volcanic sequences in the Kirkland Lake area: Geological Association of Canada- Mineralogical Association of Canada Joint Annual Meeting, Toronto, Canada, 1978, Field Trips Guidebook, p. 237–259.

Kimura, G., Ludden, J.N., Desrochers, J.P., Hori, R., 1993, A model of ocean crust accretion for the Superior province, Canada: Lithos, v. 30, p. 337–355.

Knight, C.W., 1924, Lightning River Gold area: Ont. Dept. Mines, Ann. Rept., v. 33, pt. 3, p. 41–49.

Krogh, T.E., 1973, A low-contamination method for hydrothermal decomposition of zircon and extraction of U and Pb for isotopic age determinations: Geochimica et Cosmochimica Acta, v. 37, p. 485–494.

Lafrance, B., Moorhead, J., and Davis, D.W., 2003, Cadre géologique du camp minier de Doyon–Bousquet–Laronde: Ministère des Ressources Naturelles. ET 2002-07, 46 p.

Latulippe, M., 1976, Excursion géologique: la région de Val-d'Or-Malartic. (Ed.) Ministère des richesses naturelles du Québec: Institut canadien des mines et de la métallurgie.

Laurent, O., Martin, H., Moyen, J.F., and Doucelance, R., 2014, The diversity and evolution of late-Archean granitoids: evidence for the onset of modern-style plate tectonics between

3.0 and 2.5 Ga: Lithos, v. 205, p. 208–235.

Ludwig, K.R., 2009, Isoplot 3.71—A geochronological toolkit for Microsoft Excel: Berkeley Geochronology Center, Special Publication No. 5, 75 p.

Mattinson, J.M., 2005, Zircon U–Pb chemical abrasion ("CA-TIMS") method: combined annealing and multi-step partial dissolution analysis for improved precision and accuracy of zircon ages: Chemical Geology, v. 220, p. 47–66.

MacLean, W.H., 1990, Mass change calculations in altered rock series: Mineralium Deposita, v. 25, p. 44–49.

McNicoll, V., Goutier, J., Dubé, B., Mercier-Langevin, P., Ross, P.-S., Dion, C., et al., 2014, U–Pb Geochronology of the Blake River Group, Abitibi greenstone belt, Quebec, and implications for base metal exploration: Economic Geology, v. 109, p. 27–59.

Mercier-Langevin, P., Dubé, B., Hannington, M.D., Richer-Laflèche, M., and Gosselin, G., 2007b, The LaRonde Penna Au-rich volcanogenic massive sulfide deposit, Abitibi greenstone belt, Quebec: Part II. Lithogeochemistry and paleotectonic setting: Economic Geology, v. 102, p. 611–631.

Mercier-Langevin, P., Simard, M., Dubuc, R., Côté, J., Doucet, P., Daigneault, R., Gaboury, D., 2017, Geology of the Lapa Orogenic Gold Deposit: Reviews in Economic Geology, v. 19, p. 247–262.

Moore, L.N., Daigneault, R., Aird, H.M., Banerjee, N.R., and Mueller, W.U, 2016, Reconstruction and evolution of Archean intracaldera facies: the Rouyn–Pelletier Caldera

Complex of the Blake River Group, Abitibi greenstone belt, Canada: Canadian Journal of Earth Sciences, v. 53, p. 355–377.

Mortensen, J.K., 1993, U–Pb geochronology of the eastern Abitibi Subprovince. Part 2: Noranda – Kirkland Lake area: Canadian Journal of Earth Sciences, v. 30, p. 29–41.

Mueller, W., Donaldson, J.A., and Doucet, P., 1994, Volcanic and tectono-plutonic influences on sedimentation in the Archean–Kirkland Basin, Abitibi greenstone-belt, Canada: Precambrian Research, v. 68, p. 201–230.

Mueller, W.U., Friedman, R., Daigneault, R., Moore, L., and Mortensen, J., 2012, Timing and characteristics of the Archean subaqueous Blake River Megacaldera Complex, Abitibi greenstone belt, Canada: Precambrian Research, v. 214–215. p. 1–27.

Pearson, V., and Daigneault, R., 2009, An Archean megacaldera complex: The Blake River Group, Abitibi greenstone belt: Precambrian Research, v. 168, p. 66–82.

Perrouty, S., Gaillard, N., Piette-Lauzière, N., Mir, R., Bardoux, M., Olivo, G.R., et al., 2017, Structural setting for Canadian Malartic style of gold mineralization in the Pontiac Subprovince, south of the Cadillac Larder Lake Deformation Zone, Québec, Canada: Ore Geology Reviews, v. 84, p. 185–201.

Piette-Lauzière, N., Guilmette, C., Bouvier, A., Perrouty, S., Pilote, P., Gaillard, N., et al., 2019, The timing of prograde metamorphism in the Pontiac Subprovince, Superior craton; implications for Archean geodynamics and gold mineralization: Precambrian Research, v. 320, p. 111–136.

Pilote, P., Scott, C.R., Mueller, W., Lavoie, S., and Riopel, P., 1999, Géologie des formations de Val-d'Or, Héva et Jacola : nouvelle interprétation du groupe de Malartic: Minsitère de l'énergie et des Ressources. DV 99-03. 52 p.

Pilote, P., Moorhead, J., and Mueller, W., 2000, Développement d'un arc volcanique, la région de Val-d'Or, ceinture de l'Abitibi - volcanologie physique et évolution métallogénique: Ministère de l'Énergie et des Ressources du Québec. MB 2000-09. 20 p.

Pilote, P., 2013. Géologie Malartic, 32D01-NE Ministère de l'Énergie et des Ressources naturelles du Québec; CG-32D01D-2013-01.

Pilote, P., Daigneault, R., David, J., and McNicoll, V., 2015, Architecture of the Malartic, Piché and Cadillac groups and the Cadillac Fault: Geological revisions, new dates and interpretations: Ministère de l'Énergie et des Ressources Naturelles. DV 2015-04. 37 p.

Poulsen, H., 2017, The Larder Lake-Cadillac Break and Its Gold Districts: Reviews in Economic Geology, v. 19, p. 133–167.

Ridler, R.H., 1970, Relationship of mineralization to volcanic stratigraphy in the Kirkland–Larder Lakes area, Ontario. Geol. Assoc. Can., Proc., v. 21, p. 33–42.

Robert, F., 1989, Internal structure of the Cadillac tectonic zone Southeast of Val d'Or, Abitibi greenstone-belt, Quebec: Canadian Journal of Earth Sciences, v. 26, p. 2661–2675.

Robert, F., Poulsen, K.H., Cassidy, K.F., and Hodgson, C.J., 2005, Gold metallogeny of the Superior and Yilgarn cratons: Economic Geology 100th Anniversary Volume, p. 1001–1033.

Robin, P.Y.E. and Cruden, A.R., 1994, Strain and vorticity patterns in ideally ductile transpression zones: Journal of Structural Geology, v. 16, p. 447–466.

Ross, P.S., McNicoll, V., Goutier, J., Mercier-Langevin, P., and Dubé, B., 2011, Basaltic to andesitic volcaniclastic rocks in the Blake River Group, Abitibi Greenstone Belt: 2. Origin, geochemistry, and geochronology: Canadian Journal of Earth Sciences, v. 48, p. 757–777.

Sansfaçon, R., Grant, M., and Trudel, P., 1987, Géologie de la mine Canadian Malartic—District de Val-d'Or: Ministère de l'Énergie et des Ressources du Québec, report MB 87-26, 44 p.

Sansfaçon, R., and Hubert, C., 1990, The Malartic gold district, Abitibi greenstone belt, Québec: Geological setting, structure and timing of gold emplacement at Malartic gold fields, Barnat, East-Malartic, Canadian Malartic and Sladen mines, in Rive, M., Verpaelst, P., Gagnon, Y., Lulin, J.M., Riverin, G., and Simard, A., eds., The northwestern Quebec polymetallic belt: A summary of 60 years of mining exploration: The Canadian Institute of Mining and Metallurgy, Special Volume 43, p. 221–235.

Scott, C.R., Mueller, W.U., and Pilote, P., 2002, Physical volcanology, stratigraphy, and lithogeochemistry of an Archean volcanic arc: evolution from plumerelated volcanism to arc rifting of SE Abitibi greenstone belt, Val-d'Or, Canada: Precambrian Research, v. 115, p. 223–260.

Simard, M., Gaboury, D., Daigneault, R., and Mercier-Lagevin, P., 2013, Multistage gold mineralization at the Lapa Mine, Abitibi Subprovince: Insights into auriferous

hydrothermal and metasomatic processes in the Cadillac-Larder Lake fault zone: Mineralium Deposita, v. 48, p. 883–905.

Smith, J.R., Spooner, E.T.C., Broughton, D.W., and Ploeger, F.R., 1993, Archean Au–Ag–(W) Quartz Vein/Disseminated mineralisation within the Larder Lake — Cadillac Break, Kerr Addison — Chesterville System, North East Ontario, Canada, Ontario Geoscience Research Grant Program, Grant No. 364.: Ontario Geological Survey Open File Report 5831, 310 p.

Stacey, J.S., and Kramers, J.D., 1975, Approximation of terrestrial lead isotope evolution by a two-stage model: Earth and Planetary Science Letters, v. 26, p. 207–221.

Stone, W.E., 1990, Archean volcanism and sedimentation in the Bousquet gold district, Abitibi greenstone belt, Québec: Implications for stratigraphy and gold concentration. Geological Society of America Bulletin, v. 102, p. 147–158.

Sun, S.S., and McDonough, W.F., 1989, Chemical and isotopic system of oceanic basalt: implications for mantle composition and processes: Magmatism in the Ocean Basins. Geological Society Special Publication No. 42. p. 313–345.

Thompson, J.E., 1949, Geology of the Hearst and McFadden Townships. Ontario Department of Mines. Annual Report for 1947, v. 56, p. 1–34.

Thurston, P.C., Ayer, J.A., Goutier, J., and Hamilton, M.A., 2008, Depositional gaps in Abitibi greenstone belt stratigraphy: A key to exploration for syngenetic mineralization: Economic Geology, v. 103, p. 1097–1134.

Tourigny, G., Hubert, C., Brown, A.C., Crepeau, R., 1988, Structural geology of the Blake River Group at the Bousquet Mine, Abitibi, Quebec: Can. J. Earth Sci, v. 25, p. 581–592.

Trudel, P., and Sansfaçon, R., 1987, Géologie de la mine East Malartic-Région de Val-d'Or: Ministère de l'Énergie et des Ressources du Québec, report MB 87-25, 58 p.

Trudel, P., and Sauvé, P., 1992, Synthèse des caractéristiques géologiques des gisements d'or du district de Malartic: Ministère de l'Énergie et des Ressources du Québec. MM 804, 113 p.

Trudel, P., Sauvé, P., Tourigny, G., Hubert, C., and Hoy, L., 1992, Synthèse des caractéristiques géologiques des gisements d'or de la région de Cadillac (Abitibi): Ministère de l'Énergie et des Ressources du Québec, report MM 91-01, 106 p.

Wilkinson, L., Cruden, A.R., and Krogh, T.E., 1999, Timing and kinematics of post-Timiskaming deformation within the Larder Lake – Cadillac deformation rone, southwest Abitibi greenstone belt, Ontario, Canada: Canadian Journal of Earth Sciences, v. 36, p. 627–647.

Winchester, J.A., and Floyd, P.A., 1977, Geochemical discrimination of different magma series and their differentiation products using immobile elements: Chemical Geology, v. 20, p. 165–179.

York, D., 1969, Least squares fitting of a straight line with correlated errors: Earth and Planetary Science Letters, v. 5, p. 320–324.

3. Appendix A: Analytical Methods

3.1. Whole rock lithogeochemistry

Thirty-eight samples of the Cadillac and Timiskaming groups and 6 samples of the QFP intrusion were prepared at the ALS laboratory in Sudbury and analyzed for major element and trace element composition at the ALS laboratory in Vancouver. In addition to the lab standards, two standards, a diabase and a rhyolite (LK-NIP-1-923 and ORCA-1-1140, respectively), and two duplicates were also analyzed to ensure satisfactory accuracy and precision in the analyses.

Samples were trimmed of weathered and altered surfaces, washed and dried, crushed to less than 2 mm (70% of sample), and an aliquot of 250g was further pulverized to less than 75 microns (85% of aliquot). To avoid contamination, the crushers and pulverizers were cleaned with compressed air in between each sample. Lithium metaborate and tetraborate fused samples were analyzed for major elements using the inductively coupled plasma emission spectrometry (ICP) technique, and for trace elements (Ba, Ce, Cr, Cs, Dy, Er, Eu, Ga, Gd, Hf, Ho, La, Lu, Nb, Nd, Pr, Rb, Sm, Sn, Sr, Ta, Tb, Th, Tm U, V, W, Y, Yb, Zr) using the inductively coupled plasma emission – mass spectrometry (ICP-MS) technique. Precision and accuracy is typically better than 10% and 5%, respectively, for major elements (except MnO), REEs, and other trace elements, except for measurements close to detection limits. Base metals (Cd, Co, Cu, Mo, Ni, Pb, Sc, Zn), Ag, and Li were analyzed using four acid digestion ICP technique, with a precision and accuracy better than 10% (except Ni and Pb). Trace elements (As, Bi, Hg, In, Re, Sb, Se, Te, Tl) were analysed using aqua regia digestion with an ICP-MS finish, with a precision better than 8% except for values close to detection limits. Concentrations of C and S were measured by combustion analysis in a Leco™ induction furnace and had a precision better than 4%. H_2O concentrations were measured by combustion and using the absorption of infrared energy with a precision better than 10%. Cl and F were analyzed by potassium hydroxide fusion and ion chromatography with a precision better than 6%.

3.2. Assays

Sixty-eight samples of quartz veins and their altered wall rocks, including two Au standards (0.626 ± 0.074 g/t Au and 67 ± 2 ppb Au) and two duplicates, were submitted for assay quality analyses were at the ALS laboratory in Sudbury. Sample preparation was done as summarized above. In addition to cleaning the crushers and pulverizers, to avoid contamination between mineralization samples, they were run with barren material in between samples. Fifty samples were prepared as four acid digestions and analyzed for base metals (Cu, Pb, Zn) using the ICP technique. Those fifty samples were also prepared as aqua regia digestions and analyzed for Ag using the atomic absorption spectroscopy (AAS) technique. All sixty-eight samples were analyzed for Au using fire assay with the ICP technique.

3.1. Isotope Dilution Thermal Ionization Mass Spectrometry

The description below of the methodology used for dating the QFP intrusion is from Dr. Mike Hamilton, geochronologist at the Jack Satterly Lab, University of Toronto.

Rocks were crushed using a jaw crusher and then underwent grinding using a disk mill. Initial separation of heavy minerals was carried out by passing the heavy concentrate over a shaking, riffled water (Wilfley^{TM}) table multiple times. Further processing employed density separations with methylene iodide and paramagnetic separations with a Frantz isodynamic separator. Final sample selection was achieved by hand picking in alcohol under a binocular microscope, choosing the freshest, least cracked, core-and inclusion-free grains of zircon.

Analytical methods involved isotope dilution thermal ionization mass spectrometry (ID-TIMS) following chemical abrasion (CA, modified after Mattinson, 2005). Zircon grains that underwent CA treatment were annealed in quartz crucibles at 900°C for 2 days. This removes much, although not all, of the radiation damage induced by decay of U and Th contained in the mineral, rendering least altered zircon more inert to chemical attack. The annealed grains were subsequently leached in approximately 0.10 ml of concentrated hydrofluoric (HF) acid for up to several hours in teflon vessels at 200°C. Altered parts of the crystals, which contain isotopically disturbed Pb, dissolve more rapidly than annealed, unaltered crystal domains for low to moderate levels of radiation damage. Attack is variable, depending on the uranium concentration of the grains and the consequent degree of radiation damage. Chemical abrasion has the advantage of penetrative removal of alteration domains where Pb-loss has occurred, and generally improves concordance.

Weights of mineral fractions chosen for ID-TIMS analysis were estimated from scaled digital photomicrographs, using the density of zircon. Estimated weights should be accurate to about ±20%. This affects only U and Pb concentrations, not age information, which depends only on

isotope ratio measurements. Samples were washed briefly in 7N HNO3 prior to dissolution. A mixed 205Pb-235U isotopic spike was added to the dissolution capsules during sample loading. Zircon grains were dissolved using concentrated HF in Teflon bombs at 200°C for 3-4 days, then dried and re-dissolved in 3N HCl overnight to ensure complete dissolution and equilibration with the spike (Krogh, 1973). U and Pb were isolated using 50 microliter anion exchange columns using HCl elutions, dried down, and then loaded onto outgassed rhenium filaments with silica gel (Gerstenberger and Haase, 1997).

Pb and UO2 were analyzed on a VG354 mass spectrometer using a Daly collector in pulse counting mode. The mass discrimination correction for this detector was constant at 0.07%/AMU. Thermal mass discrimination corrections are 0.10%/AMU for Pb and U. Dead time of the Daly system was 16 ns for Pb during the analytical period, monitored using the SRM982 Pb standard.

Mass spectrometer data was reduced using in-house software (UtilAge program) coded by D. Davis. All common Pb was assigned to procedural blank. Initial Pb from geological sources above 1 picogram was corrected using the Pb evolution model of Stacey and Kramers (1975). Plotting of Concordia curves and averaging of age results were carried out using the Isoplot 3.71 Add-In for MS Excel, of Ludwig (2009). The age calculated is based on a regression using a modified version of the York (1969) algorithm, in which points are weighted proportional to the inverse of the square of the assigned errors, incorporating error correlations (see Ludwig, 2009); uncertainties in the U decay constants are not considered. Probabilities of fit would be expected to be 50% on average for random data with correctly chosen analytical errors. All age errors and error ellipses are given at the 2 sigma or 95% level of confidence.

3.2. Scanning Electron Microscope

Two polished thin sections of the most-altered sandstone in the alteration halo of mineralized quartz veins emplaced in the Cadillac Group (0102AG01 and 0407AG28), and 1 polished thin section of the least-altered sandstone precursor (0407AG31), were examined using a Tescan Vega 3 – LMH scanning electron microscope equipped with a tungsten filament and a Bruker Flash 6 - 60 mm^2 energy dispersive spectrometer (EDS) detector. Data acquisition was done at an accelerating voltage of 15 kV, ~1 nA beam intensity, acquisition count time of 5 seconds, and a working distance of 15 mm. Calibration of the instrument was completed prior to data acquisition by analyzing a standard pure copper tape located on the sample holder to calibrate the X-ray energy position of the copper K-α and K-β peaks, which have known values.

4. Appendix B: Associated Data

4.1. Lithogeochemistry Results

Table 4: Concentration data for major and trace elements for all collected samples.

Analyte	Unit	Rock	Easting	Northing	SiO_2	TiO_2	Al_2O_3
Unit		Type			wt.%	wt.%	wt.%
LDL					0.01	0.01	0.01
Method					FUS-ICP	FUS-ICP	FUS-ICP
0052AG01	Cadillac	Turbidite	0706324	5340249	60.90	0.62	16.25
0052AG02	Cadillac	Siltstone	0706324	5340249	69.70	0.44	12.85
0052AG03	Cadillac	Mudstone	0706324	5340249	60.20	0.64	18.40
0094AG01	Cadillac	Mudstone	0706341	5341597	74.00	0.28	13.45
0102AG01	Cadillac	Siltstone	0708156	5341165	51.00	0.85	22.20
0102AG02	Cadillac	Siltstone	0708156	5341165	66.70	0.58	15.40
0123AG01	Timiskaming	Sandstone	0707020	5341531	67.10	0.51	14.40
0123AG02	Timiskaming	Sandstone	0707020	5341531	64.90	0.56	15.40
0124AG01	Timiskaming	Sandstone	0706994	5341488	68.10	0.48	14.50
0125AG01	Timiskaming	Sandstone	0706953	5341433	63.70	0.56	17.15
0125AG01-2	Timiskaming	Sandstone	0706953	5341433	45.70	0.93	27.10
0126AG01	Cadillac	Turbidite	0707063	5341655	65.60	0.53	16.05
0126AG02	Cadillac	Turbidite	0707063	5341655	69.70	0.47	14.80
0133AG01	Cadillac	Sandstone	0706984	5340744	77.80	0.30	11.85
LK-NIP-1-923	Standard	Diabase	—	—	49.50	1.15	15.45
0138AG01-2	Timiskaming	Duplicate	0707457	5341936	63.90	0.64	15.85
0133AG01-2	Cadillac	Sandstone	0706984	5340744	77.70	0.30	11.90
0138AG01	Timiskaming	Siltstone	0707457	5341936	59.50	0.74	18.20
0142BG01	Cadillac	Sandstone	0707020	5341578	62.20	0.64	16.85
0252AG03	Cadillac	Sandstone	0704893	5341775	41.90	1.02	26.20
0252AG04	Cadillac	Sandstone	0704893	5341775	44.70	0.98	23.70
0252AG05	Cadillac	Sandstone	0704893	5341775	62.60	0.58	16.20
0252AG06	Cadillac	Sandstone	0704893	5341775	54.00	0.78	18.55
0371AG12	Timiskaming	Sandstone	0706376	5341663	64.50	0.54	16.35
0371AG13	Timiskaming	Sandstone	0706376	5341663	66.20	0.54	15.50
0371AG14	Timiskaming	Sandstone	0706376	5341663	70.20	0.51	14.15
0371AG15	Timiskaming	Sandstone	0706376	5341663	68.40	0.45	13.90
0407AG28	Cadillac	Sandstone	0708166	5341143	39.20	0.96	26.10
0407AG29	Cadillac	Sandstone	0708166	5341143	64.60	0.52	15.15
0407AG30	Cadillac	Sandstone	0708166	5341143	67.80	0.52	14.55
0407AG31	Cadillac	Sandstone	0708166	5341143	67.20	0.53	14.85
0268AG01	Cadillac	Conglomerate	0704953	5341796	69.10	0.19	13.50
0406AG01	Cadillac	Conglomerate	0704944	5341781	72.20	0.16	13.90
0444AG01	Cadillac	Conglomerate	0704943	5341777	71.70	0.18	16.05
0445AG01	Cadillac	Conglomerate	0704940	5341780	67.90	0.21	14.90
0446AG01	Cadillac	Conglomerate	0704939	5341793	69.00	0.22	16.00
0267AG01	Timiskaming	QFP	0704954	5341798	67.60	0.27	16.85
0271AG01	Timiskaming	QFP	0705056	5341799	66.20	0.29	15.65
0286AG01	Timiskaming	QFP	0705336	5341851	67.20	0.28	15.90
0404AG01	Timiskaming	QFP	0704817	5341792	67.20	0.23	15.45
0405AG01	Timiskaming	QFP	0704914	5341777	69.90	0.26	16.80
0443AG01	Timiskaming	QFP	0704936	5341783	67.50	0.30	16.40
0271AG01	Timiskaming	QFP	0705056	5341799	67.10	0.28	16.30
ORCA-1-1140	Standard	Rhyolite	—	—	73.50	0.29	12.60
Precision	—	—	—	—	-4.24	9.00	4.87
Accuracy	—	—	—	—	1.05	2.61	1.03

Table 4: (continued).

Analyte	**Fe_2O_3**	**Cr_2O_3**	**MnO**	**MgO**	**CaO**	**SrO**	**BaO**	**Na_2O**	**K_2O**
Unit	wt.%	wt.%	wt.%	wt.%	wt.%	wt.%	wt.%	wt.%	wt.%
LDL	0.01	0.01	0.01	0.01	0.01	0.01	0.01	0.01	0.01
Method	FUS-ICP	FUS-ICP	FUS-ICP	FUS-ICP	FUS-ICP	FUS-ICP	FUS-ICP	FUS-ICP	FUS-ICP
0052AG01	7.39	0.030	0.08	2.84	2.21	0.03	0.05	2.53	2.30
0052AG02	4.31	0.020	0.07	1.64	3.48	0.04	0.04	3.27	1.55
0052AG03	6.84	0.030	0.07	3.19	1.58	0.05	0.13	2.48	3.44
0094AG01	2.30	<0.010	0.03	1.07	0.29	0.02	0.12	1.25	3.25
0102AG01	7.25	0.060	0.05	3.02	2.82	0.13	0.15	3.58	3.60
0102AG02	5.46	0.040	0.06	2.71	1.32	0.04	0.11	2.33	3.09
0123AG01	5.37	0.030	0.06	3.06	1.72	0.05	0.07	4.35	1.40
0123AG02	5.73	0.040	0.06	3.62	1.33	0.03	0.11	2.84	2.73
0124AG01	4.97	0.040	0.08	2.78	2.33	0.04	0.07	3.78	1.88
0125AG01	5.82	0.030	0.06	3.09	1.37	0.04	0.08	4.12	2.07
0125AG01-2	7.71	0.050	0.10	4.39	0.75	0.06	0.28	2.28	5.89
0126AG01	4.86	0.030	0.07	2.61	1.41	0.07	0.06	5.63	1.19
0126AG02	4.30	0.030	0.07	2.33	2.32	0.06	0.06	3.98	1.78
0133AG01	2.62	0.010	0.04	1.16	1.53	0.05	0.03	4.05	0.93
LK-NIP-1-923	13.70	0.020	0.19	7.27	10.45	0.02	0.02	2.43	0.46
0138AG01-2	6.56	0.030	0.08	3.39	1.69	0.02	0.07	1.70	2.57
0133AG01-2	2.48	0.010	0.02	1.15	1.13	0.04	0.03	4.14	0.96
0138AG01	7.27	0.030	0.08	3.82	1.53	0.02	0.10	1.57	3.27
0142BG01	6.37	0.030	0.05	3.53	0.43	0.01	0.07	2.88	2.59
0252AG03	9.35	0.057	0.10	6.24	1.54	0.06	0.20	1.33	5.78
0252AG04	10.40	0.058	0.11	6.84	2.60	0.07	0.14	2.19	4.23
0252AG05	6.37	0.032	0.07	4.10	1.98	0.08	0.10	2.98	3.12
0252AG06	8.09	0.056	0.08	5.31	2.67	0.08	0.10	2.91	3.10
0371AG12	5.62	0.038	0.07	2.82	1.50	0.04	0.14	1.65	3.38
0371AG13	5.78	0.041	0.07	2.88	1.70	0.05	0.11	2.06	3.13
0371AG14	5.34	0.038	0.07	2.77	2.12	0.06	0.08	2.45	2.66
0371AG15	5.00	0.027	0.06	2.48	1.98	0.06	0.09	2.43	2.65
0407AG28	10.00	0.077	0.02	1.23	1.07	0.09	0.35	1.41	7.16
0407AG29	5.69	0.035	0.06	2.31	2.60	0.08	0.06	3.07	1.95
0407AG30	5.67	0.036	0.07	2.64	1.99	0.06	0.08	2.45	2.71
0407AG31	5.64	0.036	0.06	2.50	1.60	0.05	0.09	2.19	3.13
0268AG01	2.60	0.005	0.05	1.18	4.25	0.06	0.04	4.44	0.96
0406AG01	2.08	0.003	0.04	0.43	2.95	0.09	0.03	4.96	0.78
0444AG01	1.68	<0.002	0.02	0.53	1.19	0.08	0.06	6.47	1.34
0445AG01	1.89	0.004	0.08	0.62	5.73	0.09	0.03	4.38	0.94
0446AG01	2.35	0.008	0.04	0.66	2.17	0.09	0.07	6.48	1.05
0267AG01	2.51	0.003	0.02	1.17	1.43	0.07	0.18	4.83	2.50
0271AG01	3.04	0.007	0.03	1.79	2.97	0.05	0.12	3.83	2.51
0286AG01	3.45	0.009	0.03	1.85	2.43	0.10	0.11	4.44	2.12
0404AG01	2.31	0.003	0.04	1.04	2.23	0.10	0.10	5.36	1.84
0405AG01	2.61	0.004	0.01	0.98	1.33	0.05	0.12	3.20	3.13
0443AG01	2.94	0.008	0.05	1.34	3.27	0.08	0.07	3.94	1.90
0271AG01	2.84	0.006	0.02	1.74	2.32	0.06	0.12	3.85	2.56
ORCA-1-1140	2.76	0.008	0.05	0.44	1.10	0.01	0.04	4.54	2.09
Precision	8.54	7.69	20.0	7.38	7.32	-9.09	17.65	-4.24	11.00
Accuracy	2.90	—	10.83	3.94	1.80	—	—	0.54	2.23

Table 4: (continued).

Analyte	P_2O_5	LOI	Total	C	S	H_20^+	Cl	F	S.G.	Ag
Unit	wt.%	wt.%	wt.%	%	%	%	ppm	ppm		ppm
LDL	0.01	0.01		0.01	0.01	0.01	50	20		0.5
Method	FUS-ICP	FUS-ICP		LECO	LECO	COM-IRS	KOH	KOH		TD-ICP
0052AG01	0.17	2.62	98.02	0.16	0.20	2.16	70	550	2.76	<0.5
0052AG02	0.11	1.03	98.55	0.24	0.11	0.59	50	410	2.72	<0.5
0052AG03	0.14	2.33	99.52	0.03	0.14	2.72	50	610	2.78	<0.5
0094AG01	0.11	1.88	98.05	0.01	0.01	1.66	80	350	2.76	<0.5
0102AG01	0.19	4.40	99.30	0.02	1.42	1.94	90	860	2.83	<0.5
0102AG02	0.16	2.33	100.3	<0.01	0.46	2.17	100	540	2.71	<0.5
0123AG01	0.16	1.22	99.50	0.01	0.21	1.27	70	440	2.67	<0.5
0123AG02	0.15	2.19	99.69	<0.01	0.04	2.11	90	530	2.75	<0.5
0124AG01	0.12	0.94	100.1	0.01	0.17	1.00	100	420	2.76	<0.5
0125AG01	0.15	2.22	100.5	0.01	0.15	2.47	60	430	2.67	<0.5
0125AG01-2	0.07	4.38	99.69	0.01	0.16	5.01	60	450	2.73	<0.5
0126AG01	0.16	1.73	100.0	0.01	0.06	1.87	100	510	2.63	<0.5
0126AG02	0.15	0.81	100.9	0.02	0.04	1.11	70	670	2.66	<0.5
0133AG01	0.07	0.84	101.3	0.08	0.08	0.77	60	250	2.61	<0.5
LK-NIP-1-923	0.11	0.11	100.9	0.02	0.03	0.81	460	260	2.99	<0.5
0138AG01-2	0.16	2.65	99.31	0.04	0.03	2.94	50	660	2.73	<0.5
0133AG01-2	0.06	0.84	100.8	0.05	0.04	0.80	60	240	2.63	<0.5
0138AG01	0.22	3.26	99.61	0.04	0.04	3.47	50	730	2.75	<0.5
0142BG01	0.16	3.26	99.07	0.04	0.02	3.27	100	530	2.74	<0.5
0252AG03	0.42	5.17	99.37	0.02	<0.01	5.65	50	1030	2.84	<0.5
0252AG04	0.44	4.88	101.3	0.06	<0.01	5.57	60	1090	2.89	<0.5
0252AG05	0.26	2.63	101.1	0.02	0.01	2.98	100	730	2.80	<0.5
0252AG06	0.36	3.41	99.50	0.01	0.01	4.08	90	1060	2.77	<0.5
0371AG12	0.11	2.33	99.09	0.01	0.49	2.46	<50	420	2.78	<0.5
0371AG13	0.13	2.17	100.4	0.01	0.38	2.34	70	450	2.75	<0.5
0371AG14	0.13	1.37	102.0	0.01	0.33	1.49	60	460	2.79	<0.5
0371AG15	0.12	1.21	98.86	0.02	0.35	1.45	80	450	2.76	<0.5
0407AG28	0.14	9.17	96.98	0.03	3.36	2.67	<50	480	3.06	1.1
0407AG29	0.13	1.36	97.62	0.02	0.75	1.18	<50	540	2.83	<0.5
0407AG30	0.15	1.33	100.1	0.01	0.40	1.74	<50	510	2.69	<0.5
0407AG31	0.15	1.39	99.42	0.01	0.45	1.88	<50	520	2.78	<0.5
0268AG01	0.08	2.40	98.86	0.56	0.02	0.87	100	340	2.72	<0.5
0406AG01	0.06	1.23	98.91	0.26	0.01	0.57	170	200	2.67	<0.5
0444AG01	0.08	0.65	100.0	0.01	0.01	0.70	190	220	2.67	<0.5
0445AG01	0.09	2.39	99.25	0.66	<0.01	0.61	90	280	2.63	<0.5
0446AG01	0.09	0.79	99.02	0.18	0.01	0.74	130	240	2.66	<0.5
0267AG01	0.12	1.80	99.35	0.18	0.02	1.61	70	520	2.65	<0.5
0271AG01	0.11	2.33	98.93	0.38	0.09	1.08	80	550	2.72	<0.5
0286AG01	0.11	1.01	99.04	0.11	<0.01	1.05	70	820	2.74	<0.5
0404AG01	0.1	2.35	98.35	0.39	<0.01	1.33	70	640	2.81	<0.5
0405AG01	0.19	1.6	100.2	0.01	0.01	1.56	70	570	2.75	<0.5
0443AG01	0.14	1.00	98.94	0.11	<0.01	0.97	90	680	2.75	<0.5
0271AG01	0.12	1.52	98.84	0.15	0.13	1.54	80	540	2.70	<0.5
ORCA-1-1140	0.06	0.57	98.06	0.01	0.01	1.21	90	320	2.71	<0.5
Precision	11.44	31.36	0.20	43.40	-3.90	-9.29	0.00	5.95	0.73	—
Accuracy	-7.63	30.63	—	—	-50.0	-32.79	—	—	—	—

Table 4: (continued).

Analyte	As	Ba	Bi	Cd	Ce	Co	Cr	Cs	Cu	Dy
Unit	ppm	ppm	ppm	ppm	ppm	ppm	ppm	ppm	ppm	ppm
LDL	0.1	0.5	0.01	0.5	0.5	1	10	0.01	1	0.05
Method	AR-MS	FUS-MS	AR-MS	TD-ICP	FUS-MS	TD-ICP	FUS-MS	FUS-MS	TD-ICP	FUS-MS
0052AG01	21.4	503	0.33	<0.5	48.1	25	210	2.77	45	2.80
0052AG02	19.9	351	0.24	<0.5	55.1	17	160	3.18	39	2.30
0052AG03	25.1	1200	0.33	<0.5	25.2	28	210	6.20	36	1.98
0094AG01	36.0	1055	0.08	<0.5	23.9	5	30	3.75	8	1.71
0102AG01	>250	1270	0.98	<0.5	42.8	34	400	4.40	9	2.97
0102AG02	>250	926	0.37	<0.5	22.6	25	300	5.82	70	2.20
0123AG01	69.1	584	0.17	<0.5	14.4	29	240	3.72	50	1.90
0123AG02	>250	921	0.12	<0.5	50.5	9	280	7.31	42	2.53
0124AG01	6.1	559	0.18	<0.5	11.6	19	240	6.74	41	1.70
0125AG01	>250	691	0.16	<0.5	19.9	21	220	3.22	38	2.81
0125AG01-2	>250	2430	0.19	<0.5	67.3	35	380	7.89	51	2.09
0126AG01	145	510	0.26	<0.5	49.9	24	200	1.74	58	2.30
0126AG02	47.8	463	0.26	<0.5	34.2	15	180	7.27	34	2.13
0133AG01	8.3	272	0.07	<0.5	39.6	12	80	1.33	25	2.16
LK-NIP-1-923	0.9	134	0.02	0.8	18.9	58	160	0.54	177	3.91
0138AG01-2	23.1	599	0.25	<0.5	58.4	22	210	4.83	45	3.24
0133AG01-2	10.0	260	0.07	<0.5	30.0	10	70	1.22	20	1.89
0138AG01	35.8	803	0.33	<0.5	28.8	22	240	5.79	59	2.13
0142BG01	100	559	0.34	<0.5	167.5	5	220	3.98	26	4.27
0252AG03	46.0	1740	0.10	<0.5	53.5	29	480	7.98	1	4.06
0252AG04	67.6	1170	0.11	<0.5	82.5	37	490	6.14	11	4.44
0252AG05	37.4	866	0.13	<0.5	40.5	19	270	2.82	37	2.59
0252AG06	75.5	836	0.16	<0.5	69.8	30	460	3.60	3	3.64
0371AG12	>250	1205	0.40	<0.5	13.1	36	310	5.51	84	1.99
0371AG13	>250	999	0.38	<0.5	15.7	30	330	5.42	66	1.90
0371AG14	244	704	0.25	<0.5	15.4	32	310	5.96	46	1.69
0371AG15	186	775	0.20	<0.5	63.3	20	230	5.9	42	2.67
0407AG28	>250	2990	3.53	0.7	115.0	49	610	7.52	13	3.86
0407AG29	>250	581	0.42	<0.5	70.1	24	310	8.08	54	2.62
0407AG30	>250	544	0.31	<0.5	34.0	25	210	9.06	52	1.60
0407AG31	>250	811	0.33	<0.5	80.1	23	290	15.1	54	2.28
0268AG01	32.7	382	0.09	<0.5	19.2	9	50	1.45	38	0.92
0406AG01	8.4	277	0.06	<0.5	15.8	4	40	0.89	3	0.50
0444AG01	7.6	571	0.03	<0.5	19.0	5	20	1.04	7	0.64
0445AG01	14.8	313	0.05	<0.5	20.9	7	40	1.33	5	1.15
0446AG01	11.1	669	0.09	<0.5	26.3	7	80	0.86	9	0.86
0267AG01	2.3	1660	0.15	<0.5	43.6	6	40	2.77	4	0.67
0271AG01	4.0	1080	0.25	<0.5	27.5	13	70	3.77	12	0.91
0286AG01	3.9	1015	0.11	<0.5	30.7	7	80	5.28	2	0.96
0404AG01	1.5	938	0.01	<0.5	30.8	7	30	3.53	2	0.60
0405AG01	71.0	1125	0.05	<0.5	12.8	2	40	3.87	6	0.59
0443AG01	9.3	662	0.20	<0.5	36.4	9	80	3.19	5	1.04
0271AG01	3.0	1145	0.38	<0.5	30.4	15	60	3.86	5	0.72
ORCA-1-1140	0.6	391	0.05	<0.5	64.0	4	80	0.58	12	10.85
Precision	35.85	11.63	-6.84	—	-38.95	-7.14	14.36	7.86	54.64	-9.01
Accuracy	—	0.64	—	—	2.57	-14.5	-5.25	-339.6	-3.54	7.50

Table 4: (continued).

Analyte	Er	Eu	Ga	Gd	Ge	Hf	Hg	Ho	In
Unit	ppm	ppm	ppm	ppm	ppm	ppm	ppm	ppm	ppm
LDL	0.03	0.03	0.1	0.05	5	0.2	0.005	0.01	0.005
Method	FUS-MS	FUS-MS	FUS-MS	FUS-MS	FUS-MS	FUS-MS	AR-MS	FUS-MS	AR-MS
0052AG01	1.64	0.94	21.4	3.37	<5	3.6	<0.005	0.54	0.018
0052AG02	1.23	0.98	15.8	2.98	<5	3.3	<0.005	0.47	0.031
0052AG03	1.36	0.64	23.5	1.99	<5	3.3	<0.005	0.45	0.020
0094AG01	1.07	0.42	16.5	1.59	<5	4.0	<0.005	0.38	<0.005
0102AG01	1.62	1.23	25.1	3.24	<5	5.7	0.007	0.58	0.025
0102AG02	1.30	0.77	19.6	2.35	<5	4.7	<0.005	0.46	0.017
0123AG01	1.26	0.57	16.5	1.49	<5	2.9	0.006	0.41	0.028
0123AG02	1.38	1.12	18.5	3.25	<5	4.0	<0.005	0.48	0.017
0124AG01	1.05	0.53	15.6	1.32	<5	3.1	<0.005	0.36	0.029
0125AG01	1.64	0.80	19.7	2.66	<5	4.1	0.008	0.59	0.018
0125AG01-2	1.26	1.17	34.0	2.96	<5	6.1	<0.005	0.41	0.015
0126AG01	1.23	1.20	16.6	3.17	<5	4.1	0.006	0.46	0.026
0126AG02	1.20	0.72	17.2	2.47	<5	3.8	<0.005	0.43	0.023
0133AG01	1.23	0.81	10.6	2.86	<5	2.3	0.007	0.46	0.009
LK-NIP-1-923	2.28	1.06	19.1	3.68	<5	2.3	<0.005	0.83	0.016
0138AG01-2	1.54	1.47	19.7	4.68	<5	3.2	<0.005	0.63	0.019
0133AG01-2	1.14	0.66	10.5	2.08	<5	2.4	0.005	0.39	0.009
0138AG01	1.35	0.85	22.6	2.06	<5	3.8	<0.005	0.47	0.022
0142BG01	1.78	2.15	20.8	7.04	<5	3.3	<0.005	0.72	0.012
0252AG03	2.12	1.36	35.6	4.32	<5	5.7	0.005	0.66	0.013
0252AG04	2.48	2.05	30.8	6.30	<5	5.7	<0.005	0.84	0.019
0252AG05	1.55	1.39	17.8	3.29	<5	3.2	0.007	0.47	0.020
0252AG06	1.98	1.63	23.2	5.17	<5	5.1	0.005	0.69	0.026
0371AG12	1.22	0.59	19.9	1.66	<5	4.3	<0.005	0.44	0.013
0371AG13	1.33	0.62	18.9	1.46	<5	4.3	<0.005	0.38	0.012
0371AG14	1.07	0.59	16.6	1.42	<5	3.7	0.005	0.35	0.012
0371AG15	1.41	1.15	16.5	3.66	<5	3.1	0.007	0.49	0.014
0407AG28	2.20	1.88	37.6	5.52	<5	9.2	0.007	0.75	0.022
0407AG29	1.23	1.17	18.4	3.51	<5	4.3	0.010	0.39	0.022
0407AG30	1.00	0.71	13.5	2.07	<5	3.6	0.006	0.35	0.017
0407AG31	1.49	1.16	17.6	3.54	<5	4.1	0.005	0.43	0.015
0268AG01	0.62	0.42	15.2	1.20	<5	2.8	0.024	0.22	0.012
0406AG01	0.30	0.37	16.8	0.90	<5	2.7	0.048	0.11	0.007
0444AG01	0.30	0.50	17.7	1.01	<5	3.2	0.011	0.10	0.006
0445AG01	0.75	0.50	16.5	1.31	<5	3.1	0.014	0.23	0.011
0446AG01	0.41	0.71	20.0	1.69	<5	3.1	0.028	0.14	0.013
0267AG01	0.29	0.95	28.4	1.94	<5	3.5	0.022	0.11	<0.005
0271AG01	0.44	0.55	23.8	1.69	<5	3.3	0.027	0.14	0.006
0286AG01	0.43	0.59	25.0	1.54	<5	3.6	<0.005	0.14	0.013
0404AG01	0.23	0.58	22.0	1.42	<5	3.6	0.015	0.08	<0.005
0405AG01	0.24	0.43	26.0	0.93	<5	3.7	0.009	0.08	<0.005
0443AG01	0.53	0.77	22.5	1.92	<5	3.3	0.013	0.21	0.011
0271AG01	0.40	0.54	25.1	1.40	<5	3.4	0.019	0.13	0.006
ORCA-1-1140	7.77	1.30	15.9	9.26	<5	7.8	<0.005	2.42	0.022
Precision	-1.81	-25.81	4.20	-29.49	—	7.08	34.78	-10.8	7.32
Accuracy	4.23	5.61	2.08	7.90	—	2.00	—	5.44	63.33

Table 4: (continued).

Analyte	La	Li	Lu	Mo	Nb	Nd	Ni	Pb	Pr	Rb
Unit	ppm	ppm	ppm	ppm	ppm	ppm	ppm	ppm	ppm	ppm
LDL	0.5	10	0.01	1	0.2	0.1	1	2	0.03	0.2
Method	FUS-MS	TD-ICP	FUS-MS	TD-ICP	FUS-MS	FUS-MS	TD-ICP	TD-ICP	FUS-MS	FUS-MS
0052AG01	24.0	40	0.27	2	7.2	21.0	90	19	5.83	77.4
0052AG02	28.0	20	0.17	2	5.1	22.4	57	16	6.37	61.2
0052AG03	10.6	50	0.24	1	6.7	11.4	111	19	3.05	114.5
0094AG01	7.40	20	0.16	<1	8.3	6.9	17	27	1.88	86.3
0102AG01	19.4	40	0.29	2	8.4	19.1	134	28	5.02	121.0
0102AG02	10.6	40	0.22	8	5.8	10.3	79	16	2.71	87.0
0123AG01	5.80	30	0.19	1	4.5	6.8	117	16	1.70	43.1
0123AG02	25.5	40	0.21	1	5.1	21.8	56	13	5.94	78.4
0124AG01	5.70	30	0.18	1	4.3	5.4	70	15	1.36	62.4
0125AG01	10.9	40	0.25	1	5.2	11.1	87	10	2.90	59.1
0125AG01-2	30.2	60	0.27	2	7.8	28.0	141	9	7.73	160.0
0126AG01	30.4	40	0.19	1	5.6	24.4	84	16	6.69	41.2
0126AG02	14.5	30	0.19	1	6.3	14.5	66	24	3.94	73.8
0133AG01	23.7	20	0.19	1	3.5	19.7	42	6	5.28	28.2
LK-NIP-1-923	8.50	10	0.34	1	4.5	11.3	157	5	2.48	12.7
0138AG01-2	43.7	40	0.24	1	5.9	36.2	98	13	9.58	82.1
0133AG01-2	13.5	10	0.18	1	3.2	12.8	35	6	3.43	27.2
0138AG01	12.4	40	0.24	2	6.7	13.9	94	13	3.51	101.5
0142BG01	88.5	50	0.24	2	5.8	71.6	52	7	18.95	80.0
0252AG03	24.9	80	0.31	<1	9.0	26.3	126	10	6.50	214.0
0252AG04	41.7	80	0.32	<1	8.9	41.7	148	15	10.25	155.0
0252AG05	22.4	40	0.19	<1	5.7	22.3	81	12	5.69	104.0
0252AG06	36.9	70	0.28	1	6.7	35.8	119	15	9.20	104.5
0371AG12	5.1	40	0.24	1	5.0	5.9	143	14	1.63	94.6
0371AG13	6.1	40	0.19	1	4.9	6.9	126	11	1.87	86.6
0371AG14	6.8	30	0.17	1	4.3	6.9	101	11	1.88	80.9
0371AG15	31.7	30	0.19	1	4.2	27.4	83	11	7.31	81.5
0407AG28	57.8	30	0.34	2	9.5	49.5	185	26	12.95	196.0
0407AG29	35.7	30	0.19	2	5.6	29.9	91	26	7.98	76.1
0407AG30	16.3	40	0.11	1	3.8	14.7	91	22	3.80	71.9
0407AG31	38.8	40	0.20	1	4.8	34.1	94	19	9.12	107.0
0268AG01	9.3	20	0.10	1	1.9	9.5	15	8	2.43	33.9
0406AG01	7.6	10	0.03	1	2.0	8.2	9	9	2.07	25.4
0444AG01	8.1	10	0.04	<1	2.2	8.3	6	7	2.05	46.3
0445AG01	9.3	10	0.08	<1	2.2	10.1	22	15	2.49	34.2
0446AG01	13.6	10	0.07	<1	2.5	13.7	20	10	3.39	32.5
0267AG01	23.4	30	0.04	<1	3.1	24.1	11	7	6.04	75.1
0271AG01	12.5	30	0.04	<1	2.6	13.1	15	6	3.26	70.5
0286AG01	15.0	20	0.06	1	2.6	15.9	24	10	4.01	64.5
0404AG01	18.6	20	0.03	<1	2.6	16.4	13	6	4.44	52.2
0405AG01	7.0	30	0.03	1	2.9	7.8	5	9	2.01	96.6
0443AG01	19.5	30	0.08	<1	3	19.3	41	16	5.02	70.4
0271AG01	13.9	30	0.06	<1	2.7	15.4	19	5	3.82	74.9
ORCA-1-1140	27.3	10	1.22	4	10.8	35.9	4	5	8.16	53.5
Precision	-61.1	0.00	-20.00	66.7	4.46	-52.58	-13.9	9.09	-54.28	7.54
Accuracy	3.60	-63.9	1.29	19.3	7.53	3.22	17.8	-25.8	5.58	3.43

Table 4: (continued).

Analyte	Re	Sb	Sc	Se	Sm	Sn	Sr	Ta	Tb	Te
Unit	ppm	ppm	ppm	ppm	ppm	ppm	ppm	ppm	ppm	ppm
LDL	0.001	0.05	1	0.2	0.03	1	0.1	0.1	0.01	0.01
Method	AR-MS	AR-MS	TD-ICP	AR-MS	FUS-MS	FUS-MS	FUS-MS	FUS-MS	FUS-MS	AR-MS
0052AG01	0.002	0.16	16	0.2	4.11	2	291	0.5	0.45	0.05
0052AG02	0.001	0.16	9	<0.2	4.02	1	319	0.4	0.41	0.03
0052AG03	0.002	0.25	20	0.2	2.41	1	404	0.5	0.31	0.06
0094AG01	<0.001	0.31	4	<0.2	1.56	2	199.5	0.6	0.27	<0.01
0102AG01	0.002	18.80	18	1.3	3.96	1	1065	0.5	0.50	0.44
0102AG02	0.001	0.76	14	0.3	2.35	1	374	0.4	0.34	0.07
0123AG01	0.001	0.39	14	0.2	1.56	1	432	0.3	0.29	0.04
0123AG02	0.001	1.08	14	<0.2	3.88	1	360	0.4	0.45	0.04
0124AG01	0.002	0.21	12	0.2	1.22	1	400	0.3	0.22	0.04
0125AG01	0.001	1.13	14	<0.2	2.42	1	393	0.4	0.45	0.03
0125AG01-2	0.001	1.35	17	0.2	4.61	2	548	0.6	0.36	0.06
0126AG01	0.001	0.56	11	<0.2	4.04	1	592	0.4	0.41	0.03
0126AG02	<0.001	1.09	10	<0.2	2.94	1	566	0.5	0.34	0.03
0133AG01	<0.001	0.41	6	<0.2	3.36	1	448	0.3	0.39	0.01
LK-NIP-1-923	0.001	<0.05	31	<0.2	2.95	1	167	0.3	0.61	<0.01
0138AG01-2	0.001	0.22	17	0.2	6.13	1	237	0.4	0.60	0.06
0133AG01-2	<0.001	0.30	6	<0.2	2.52	1	393	0.3	0.32	0.03
0138AG01	0.001	0.23	19	<0.2	2.47	1	222	0.5	0.34	0.07
0142BG01	0.001	2.24	18	<0.2	11.6	1	93.3	0.4	0.79	0.04
0252AG03	<0.001	0.22	18	0.2	5.16	2	475	0.6	0.63	0.02
0252AG04	<0.001	0.23	16	<0.2	7.50	1	575	0.9	0.78	0.02
0252AG05	<0.001	0.29	12	<0.2	4.34	1	634	0.5	0.44	0.03
0252AG06	0.001	0.32	16	0.2	5.99	1	616	0.6	0.66	0.03
0371AG12	0.001	0.67	14	0.4	1.51	1	359	0.5	0.33	0.08
0371AG13	0.001	0.72	14	0.4	1.60	1	420	0.4	0.25	0.08
0371AG14	0.001	0.56	13	0.3	1.67	1	482	0.5	0.23	0.03
0371AG15	0.001	0.56	13	0.4	4.73	1	476	0.4	0.48	0.02
0407AG28	0.001	57.10	20	3.3	7.05	2	695	0.8	0.64	0.41
0407AG29	0.001	10.25	13	0.8	4.72	1	643	0.5	0.41	0.10
0407AG30	0.001	1.78	13	0.2	2.81	<1	348	0.3	0.29	0.04
0407AG31	0.001	0.96	13	<0.2	5.86	1	396	0.5	0.44	0.04
0268AG01	<0.001	0.21	4	<0.2	1.88	<1	522	0.2	0.19	0.03
0406AG01	0.001	0.21	2	<0.2	1.44	<1	747	0.2	0.10	0.01
0444AG01	<0.001	0.14	2	<0.2	1.57	1	697	0.2	0.10	0.01
0445AG01	<0.001	0.17	3	<0.2	1.83	<1	738	0.2	0.18	0.01
0446AG01	<0.001	0.22	4	<0.2	2.47	1	775	0.2	0.17	0.01
0267AG01	<0.001	0.35	3	0.2	3.66	1	548	0.2	0.20	0.03
0271AG01	<0.001	0.52	5	<0.2	2.45	1	431	0.2	0.17	0.03
0286AG01	<0.001	0.10	5	<0.2	2.86	1	801	0.2	0.20	0.01
0404AG01	<0.001	0.16	3	<0.2	2.63	1	794	0.2	0.11	<0.01
0405AG01	<0.001	0.30	3	0.2	1.51	1	404	0.2	0.10	0.01
0443AG01	0.001	0.07	5	<0.2	3.53	1	630	0.3	0.21	0.04
0271AG01	<0.001	0.51	5	0.3	2.54	1	470	0.2	0.17	0.03
ORCA-1-1140	0.001	0.10	7	<0.2	9.51	4	71	1.0	1.65	<0.01
Precision	0.00	3.19	5.56	—	-44.4	0.00	-7.60	11.11	-27.66	7.69
Accuracy	—	—	7.64	—	2.58	-14.29	3.22	-0.51	9.45	—

Table 4: (concluded).

Analyte	Th	Tl	Tm	U	V	W	Y	Yb	Zn	Zr
Unit	ppm	ppm	ppm	ppm	ppm	ppm	ppm	ppm	ppm	ppm
LDL	0.05	0.02	0.01	0.05	5	1	0.5	0.03	2	2
Method	FUS-MS	AR-MS	FUS-MS	FUS-MS	FUS-MS	FUS-MS	FUS-MS	FUS-MS	TD-ICP	FUS-MS
0052AG01	8.82	0.20	0.23	2.3	122	3	13.4	1.63	82	140
0052AG02	7.09	0.42	0.18	1.86	72	2	11.5	1.18	62	130
0052AG03	7.65	0.47	0.20	2.25	147	2	10.6	1.42	89	121
0094AG01	20.10	0.05	0.15	4.00	30	5	9.5	1.08	32	134
0102AG01	9.39	0.17	0.25	3.24	166	22	15.1	1.76	70	234
0102AG02	7.15	0.18	0.19	2.45	121	5	11.8	1.25	48	191
0123AG01	5.07	0.30	0.19	1.67	99	1	11.1	1.21	77	115
0123AG02	6.11	0.4	0.19	1.99	111	3	13.4	1.35	51	156
0124AG01	5.20	0.46	0.17	1.62	91	<1	9.6	1.10	68	131
0125AG01	6.54	0.17	0.25	2.32	110	3	15.4	1.56	81	156
0125AG01-2	10.45	0.10	0.21	3.66	189	10	10.8	1.61	88	237
0126AG01	7.69	0.08	0.17	2.29	83	2	12.5	1.25	137	159
0126AG02	10.95	0.54	0.18	2.97	79	3	11.6	1.24	69	139
0133AG01	3.17	0.12	0.20	1.13	48	1	12.1	1.24	39	92
LK-NIP-1-923	1.63	0.08	0.32	0.50	311	1	21.3	2.21	105	86
0138AG01-2	5.79	0.34	0.23	1.52	128	2	16.4	1.51	86	123
0133AG01-2	2.87	0.12	0.17	0.78	45	1	10.2	1.11	41	91
0138AG01	7.02	0.31	0.22	1.91	151	2	12.2	1.70	88	143
0142BG01	6.56	0.04	0.26	2.12	132	2	19.1	1.67	61	123
0252AG03	9.49	0.17	0.35	2.95	255	8	20.3	2.13	107	219
0252AG04	9.03	0.23	0.36	2.82	234	4	23.8	2.18	114	220
0252AG05	5.18	0.05	0.23	1.53	132	2	14.9	1.30	60	129
0252AG06	6.74	0.15	0.27	1.96	174	3	19.1	1.87	67	184
0371AG12	5.92	0.33	0.21	1.95	129	19	12.3	1.50	79	170
0371AG13	5.81	0.32	0.19	1.87	124	22	11.3	1.25	86	163
0371AG14	5.56	0.42	0.19	1.91	119	25	10.8	1.26	73	151
0371AG15	4.85	0.42	0.22	1.62	108	23	13.2	1.44	70	116
0407AG28	12.40	0.05	0.37	4.05	210	25	20.4	2.20	38	357
0407AG29	7.17	0.49	0.22	2.21	118	7	12.8	1.29	80	176
0407AG30	4.85	0.55	0.16	1.67	86	4	9.0	1.05	87	126
0407AG31	6.07	0.63	0.20	1.92	112	4	12.4	1.47	90	161
0268AG01	1.28	0.15	0.09	0.48	53	8	6.3	0.76	26	90
0406AG01	1.21	0.07	0.05	0.54	29	2	3.2	0.27	17	89
0444AG01	1.25	0.04	0.04	0.47	43	3	3.5	0.47	15	101
0445AG01	1.27	0.12	0.09	0.35	31	2	7.4	0.73	19	104
0446AG01	1.54	0.05	0.06	0.70	47	8	4.8	0.40	20	104
0267AG01	2.25	0.08	0.04	0.74	42	3	3.6	0.21	57	130
0271AG01	1.69	0.24	0.05	0.71	54	3	4.0	0.31	60	108
0286AG01	1.75	0.44	0.07	0.56	53	3	4.6	0.4	80	107
0404AG01	1.70	0.16	0.03	0.52	28	1	2.8	0.24	65	123
0405AG01	1.89	0.26	0.03	0.82	39	3	2.7	0.17	52	128
0443AG01	2.10	0.40	0.07	0.65	58	3	6.0	0.47	74	126
0271AG01	1.85	0.25	0.04	0.70	51	2	3.8	0.33	52	109
ORCA-1-1140	4.76	0.02	1.20	1.28	8	2	72.1	8.35	56	257
Precision	5.08	-6.66	8.89	12.08	11.10	20.00	-12.12	2.79	8.29	7.06
Accuracy	2.13	58.64	6.10	-1.16	9.97	-127.3	3.51	-0.01	-8.26	-3.43

Note: Coordinates in UTM Zone 17 NAD 83; LOI, loss on ignition; S.G., specific gravity; FUS-ICP, lithium metaborate and tetraborate fusion ICP; LECO, combustion by Leco induction furnace; COM-IRS, combustion furnace and infrared spectrometry; KOH, potassiumhydroxide fusion and ion chromatography; TD-ICP, total four-acid digestion ICP; AR-MS, aqua regia digestion ICP-MS; FUS-MS, lithium metaborate and tetraborate fusion ICP-MS; Precision, precision uncertainty in percent; Accuracy, relative difference in percent.

4.2. Assay Results

Table 5: Gold and base metal assay results.

Analyte	Unit	Rock	Easting	Northing	Ag	Au	Cu	Pb	Zn
Unit		Type			ppm	ppm	%	%	%
LDL					0.2	0.001	0.001	0.001	0.001
Method					AR-AAS	FA-ICP	TD-ICP	TD-ICP	TD-ICP
0040AG01-2	Timiskaming	Quartz	0706379	5341672	<0.2	<0.001	<0.001	<0.001	0.001
0040AG01-3	Timiskaming	A.-s.s.	0706379	5341672	<0.2	0.333	0.012	0.001	0.007
0102AG01-2	Cadillac	Quartz	0708156	5341165	0.2	0.465	<0.001	<0.001	0.001
0102AG01-3	Cadillac	A.-s.s.	0708156	5341165	1.3	7.390	<0.001	0.002	0.004
0123AG02-2	Timiskaming	Quartz	0707020	5341531	0.7	0.040	<0.001	0.005	<0.001
0125AG01-3	Timiskaming	Quartz	0706953	5341433	<0.2	0.006	<0.001	<0.001	0.001
0125AG01-4	Timiskaming	A.-s.s.	0706953	5341433	<0.2	0.013	0.004	<0.001	0.009
0126AG01-2	Cadillac	Quartz	0707063	5341655	<0.2	0.007	<0.001	<0.001	0.001
0126AG01-3	Cadillac	A.-s.s.	0707063	5341655	<0.2	0.010	0.003	<0.001	0.01
0252AG03	Cadillac	S.A.-s.s.	0704893	5341775	—	0.010	—	—	—
0252AG04	Cadillac	M.A.-s.s.	0704893	5341775	—	0.026	—	—	—
0252AG05	Cadillac	W.A.-s.s.	0704893	5341775	—	0.008	—	—	—
0252AG06	Cadillac	L.A.-s.s.	0704893	5341775	—	0.010	—	—	—
0371AG12	Timiskaming	S.A.-s.s.	0706376	5341663	—	0.040	—	—	—
0371AG13	Timiskaming	M.A.-s.s.	0706376	5341663	—	0.035	—	—	—
0371AG14	Timiskaming	W.A.-s.s.	0706376	5341663	—	0.074	—	—	—
0371AG15	Timiskaming	L.A.-s.s.	0706376	5341663	—	0.096	—	—	—
0407AG28	Cadillac	S.A.-s.s.	0708166	5341143	—	12.800	—	—	—
0407AG29	Cadillac	M.A.-s.s.	0708166	5341143	—	1.4300	—	—	—
0407AG30	Cadillac	W.A.-s.s.	0708166	5341143	—	0.072	—	—	—
0407AG31	Cadillac	L.A.-s.s.	0708166	5341143	—	0.060	—	—	—
0271AG01	Timiskaming	QFP	0704954	5341798	—	0.003	—	—	—
0286AG01	Timiskaming	QFP	0705056	5341799	—	0.025	—	—	—
0404AG01	Timiskaming	QFP	0705336	5341851	—	0.001	—	—	—
0405AG01	Timiskaming	QFP	0704817	5341792	—	<0.001	—	—	—
0443AG01	Timiskaming	QFP	0704914	5341777	—	<0.001	—	—	—
0271AG01	Timiskaming	Duplicate	0705056	5341799	—	0.001	—	—	—
0407AG02	Cadillac	Quartz	0708155	5341162	<0.2	<0.001	0.001	<0.001	0.002
0407AG03	Cadillac	Quartz	0708147	5341164	<0.2	<0.001	0.001	0.001	0.002
0407AG04	Cadillac	Quartz	0708144	5341166	<0.2	0.008	0.001	<0.001	0.005
0407AG05	Cadillac	Quartz	0708141	5341167	<0.2	<0.001	0.001	<0.001	0.003
0407AG06	Cadillac	Quartz	0708140	5341167	<0.2	0.001	0.001	<0.001	0.003
0407AG07	Cadillac	Quartz	0708138	5341168	<0.2	0.004	<0.001	<0.001	0.003
0407AG08	Cadillac	Quartz	0708156	5341161	<0.2	<0.001	<0.001	0.001	0.002
0407AG09	Cadillac	Quartz	0708145	5341164	<0.2	<0.001	<0.001	<0.001	0.002
0407AG10	Cadillac	Quartz	0708150	5341163	<0.2	0.001	0.001	0.002	0.007
0407AG11	Cadillac	Quartz	0708157	5341165	<0.2	<0.001	<0.001	<0.001	0.001
0407AG12	Cadillac	Quartz	0708157	5341164	<0.2	<0.001	<0.001	<0.001	0.001
0371AG02	Timiskaming	Quartz	0706373	5341675	<0.2	<0.001	<0.001	<0.001	0.001
0371AG03	Timiskaming	Quartz	0706382	5341678	<0.2	<0.001	<0.001	<0.001	0.001
0371AG04	Timiskaming	Quartz	0706372	5341659	<0.2	<0.001	0.001	<0.001	0.003
0371AG05	Timiskaming	Quartz	0706372	5341657	<0.2	<0.001	<0.001	<0.001	0.001
0371AG06	Timiskaming	Quartz	0706369	5341661	<0.2	<0.001	<0.001	<0.001	0.001
0407AG12	Timiskaming	Quartz	0708157	5341164	<0.2	<0.001	<0.001	<0.001	0.001
CDN-GS-P6	Standard	0.626±0.074 g/t	—	—	<0.2	0.642	0.005	0.001	0.007
0407AG13	Cadillac	Quartz	0708139	5341170	<0.2	<0.001	<0.001	<0.001	0.001

Table 5: (concluded).

Analyte	Unit	Rock	Easting	Northing	Ag	Au	Cu	Pb	Zn
Unit		Type			ppm	ppm	%	%	%
LDL					0.2	0.001	0.001	0.001	0.001
Method					AR-AAS	FA-ICP	TD-ICP	TD-ICP	TD-ICP
0407AG14	Cadillac	Quartz	0708142	5341169	<0.2	0.023	<0.001	<0.001	0.001
0407AG15	Cadillac	Quartz	0708143	5341169	<0.2	<0.001	<0.001	<0.001	0.001
0407AG16	Cadillac	Quartz	0708146	5341168	<0.2	0.015	<0.001	<0.001	0.001
0407AG17	Cadillac	Quartz	0708151	5341166	<0.2	0.145	0.001	<0.001	0.001
0407AG18	Cadillac	Quartz	0708154	5341165	0.3	0.027	0.001	0.001	0.001
0407AG19	Cadillac	Quartz	0708157	5341165	<0.2	<0.001	<0.001	<0.001	0.001
0407AG20	Cadillac	Quartz	0708152	5341165	<0.2	0.019	0.001	0.002	0.002
0407AG21	Cadillac	Quartz	0708147	5341167	<0.2	<0.001	<0.001	<0.001	0.001
0407AG22	Cadillac	Quartz	0708143	5341168	<0.2	0.011	<0.001	<0.001	0.001
0407AG23	Cadillac	Quartz	0708166	5341157	<0.2	0.070	<0.001	<0.001	0.001
0407AG24	Cadillac	Quartz	0708162	5341158	<0.2	0.015	<0.001	<0.001	0.002
0407AG25	Cadillac	Quartz	0708159	5341159	<0.2	0.258	<0.001	<0.001	0.002
0407AG26	Cadillac	Quartz	0708152	5341161	<0.2	0.050	<0.001	<0.001	0.002
0407AG27	Cadillac	Quartz	0708139	5341164	<0.2	0.027	<0.001	<0.001	0.001
0371AG07	Timiskaming	Quartz	0706382	5341682	<0.2	0.070	<0.001	<0.001	0.001
0371AG08	Timiskaming	Quartz	0706379	5341682	<0.2	0.024	<0.001	<0.001	0.004
0371AG09	Timiskaming	Quartz	0706372	5341662	<0.2	0.183	0.001	<0.001	0.003
0371AG10	Timiskaming	Quartz	0706370	5341666	<0.2	0.006	<0.001	<0.001	0.002
0371AG11	Timiskaming	Quartz	0706369	5341669	<0.2	<0.001	<0.001	<0.001	0.001
0252AG07	Cadillac	Quartz	0704893	5341775	<0.2	0.008	0.001	<0.001	0.006
0371AG10	Timiskaming	Duplicate	0706370	5341666	<0.2	0.023	<0.001	<0.001	0.002
OREAS 44P	Standard	67 ppb	—	—	0.4	0.060	0.044	0.023	0.069

Note: Coordinates in UTM Zone 17 NAD 83; A.-s.s., altered sandstone; S.A., strongly altered; M.A., moderately altered; W.A., weakly altered; L.A., least altered; AR-AAS, aqua regia digestion AAS; FA-ICP, fire assay ICP; TD-ICP, total four-acid digestion ICP.

4.3. Structural Measurements

Table 6: Structural measurements.

Station ID	Easting	Northing	Structure Type	Strike	Dip
MEAM17BSA0039	0705903	5340077	S_1 cleavage	140	90
MEAM17BSA0040	0706380	5341672	Bedding	100	85
MEAM17BSA0041	0706085	5340147	S_1 cleavage	115	84
MEAM17BSA0042	0706076	5340130	F_1 axial plane	292	83
MEAM17BSA0044	0706350	5339678	S_1 cleavage	292	90
MEAM17BSA0045	0706498	5339717	S_1 cleavage	122	79
MEAM17BSA0046	0706587	5339852	S_1 cleavage	300	90
MEAM17BSA0047	0706652	5339864	S_1 cleavage	308	81
MEAM17BSA0048	0706592	5339918	F_1 axial plane	119	74
MEAM17BSA0049	0706546	5339923	S_1 cleavage	303	86
MEAM17BSA0050	0706552	5339929	S_1 cleavage	119	89
MEAM17BSA0052	0706325	5340249	Bedding	298	90
MEAM17BSA0053	0706403	5340236	Bedding	300	90
			S_1 cleavage	300	90
			Dextral fracture	194	81
MEAM17BSA0054	0706580	5340195	S_1 cleavage	302	90
			F_3 axial plane	090	81
MEAM17BSA0056	0706809	5340122	S_1 cleavage	286	89
MEAM17BSA0057	0707004	5340047	Bedding	290	90
MEAM17BSA0058	0707271	5340199	Bedding	275	88
			S_1 cleavage	280	88
MEAM17BSA0061	0706993	5340334	S_1 cleavage	285	89
			F_1 axial plane	100	84
			F_1 fold axis	105	19
MEAM17BSA0062	0706778	5340512	S_1 cleavage	292	82
MEAM17BSA0063	0709552	5337787	S_1 cleavage	280	76
			Dextral fracture	288	81
			Dextral fracture	024	71
MEAM17BSA0064	0709196	5338044	S_1 cleavage	330	84
			L_1 lineation	075	66
MEAM17BSA0065	0713180	5337016	S_1 cleavage	292	85
MEAM17BSA0067	0710083	5338445	Bedding	305	81
			L_1 lineation	108	21
MEAM17BSA0068	0709859	5338481	S_1 cleavage	287	81
MEAM17BSA0069	0709894	5338526	Bedding	305	86
			S_1 cleavage	300	87
MEAM17BSA0073	0710789	5336684	Bedding	139	64
			S_1 cleavage	265	81
			F_3 axial plane	266	81
MEAM17BSA0074	0708960	5337859	Bedding	326	86
			S_1 cleavage	300	86
MEAM17BSA0076	0709728	5337772	Bedding	330	84
			S_1 cleavage	329	85
MEAM17BSA0077	0709877	5337697	S_1 cleavage	285	90
			S_3 cleavage	083	84
			S_3 cleavage	075	80
MEAM17BSA0078	0713168	5336525	S_1 cleavage	270	76

Table 6: (continued).

Station ID	Easting	Northing	Structure Type	Strike	Dip
MEAM17BSA0079	0712692	5336655	S_1 cleavage	292	82
MEAM17BSA0083	0712137	5339423	S_1 cleavage	306	85
			L_1 lineation	092	30
MEAM17BSA0084	0712170	5339609	S_1 cleavage	290	72
MEAM17BSA0085	0712187	5339729	Bedding	295	77
			S_1 cleavage	295	77
MEAM17BSA0086	0712752	5339098	S_1 cleavage	291	85
MEAM17BSA0087	0712933	5338802	S_1 cleavage	291	86
MEAM17BSA0088	0712953	5338713	S_1 cleavage	295	85
MEAM17BSA0089	0707065	5341661	Bedding	112	88
			S_1 cleavage	112	88
			S_3 cleavage	260	86
MEAM17BSA0090	0706858	5341429	Bedding	300	85
			S_1 cleavage	110	86
MEAM17BSA0091	0707024	5341542	Bedding	290	85
			S_1 cleavage	285	87
MEAM17BSA0092	0706978	5341563	Bedding	129	89
MEAM17BSA0093	0706345	5341613	S_1 cleavage	286	87
MEAM17BSA0094	0706342	5341598	S_1 cleavage	273	78
			L_1 lineation	128	50
MEAM17BSA0095	0706336	5341718	Bedding	290	88
MEAM17BSA0096	0706340	5341727	S_1 cleavage	106	86
			V_4 vein	080	80
MEAM17BSA0097	0706553	5341464	Bedding	100	87
MEAM17BSA0098	0706555	5341480	S_1 cleavage	104	90
MEAM17BSA0099	0706770	5341580	F_1 axial plane	100	70
			F_1 fold axis	105	16
			V_3 vein	270	85
			V_4 vein	301	66
MEAM17BSA0100	0707161	5341434	Bedding	101	81
			S_1 cleavage	113	90
MEAM17BSA0101	0707188	5341473	Bedding	114	88
			S_1 cleavage	294	83
MEAM17BSA0102	0708157	5341165	Bedding	290	88
			S_1 cleavage	291	88
			F_1 axial plane	274	90
			F_1 fold axis	094	24
			S_3 cleavage	267	86
MEAM17BSA0103	0708215	5341258	Bedding	287	88
MEAM17BSA0104	0708287	5341192	S_1 cleavage	298	89
			F_1 axial plane	106	84
			F_1 axial plane	281	89
			F_1 fold axis	115	53
MEAM17BSA0105	0708495	5341203	Bedding	295	86
			F_3 axial plane	250	79
			F_3 fold axis	265	39
MEAM17BSA0106	0708582	5341177	L_1 lineation	285	89
MEAM17BSA0107	0708737	5341146	Bedding	287	88
			S_1 cleavage	287	88
MEAM17BSA0108	0708794	5340756	S_1 cleavage	296	84

Table 6: (continued).

Station ID	Easting	Northing	Structure Type	Strike	Dip
MEAM17BSA0108	0708794	5340756	F_1 axial plane	290	84
MEAM17BSA0109	0707853	5341263	Bedding	294	89
			S_1 cleavage	283	90
			F_1 axial plane	284	87
			F_1 fold axis	102	38
MEAM17BSA0110	0707807	5341348	Bedding	288	89
			S_1 cleavage	281	90
MEAM17BSA0111	0707720	5341412	Bedding	104	85
			S_1 cleavage	281	86
MEAM17BSA0112	0707593	5341459	Bedding	286	89
			S_1 cleavage	287	90
MEAM17BSA0113	0707501	5341480	Bedding	290	89
			S_1 cleavage	283	89
MEAM17BSA0114	0707228	5341604	Bedding	304	85
			S_1 cleavage	299	89
MEAM17BSA0115	0706980	5341710	Bedding	292	89
			S_1 cleavage	296	88
			S_3 cleavage	095	83
			F_3 axial plane	085	74
			F_3 fold axis	230	63
MEAM17BSA0117	0706916	5341579	Bedding	297	89
			S_1 cleavage	298	89
MEAM17BSA0118	0706610	5341627	Bedding	086	86
			S_3 cleavage	089	89
MEAM17BSA0120	0706826	5341602	Bedding	108	89
			S_1 cleavage	103	89
MEAM17BSA0127	0707931	5341177	Bedding	109	89
			S_1 cleavage	115	89
MEAM17BSA0128	0707959	5341185	Bedding	106	89
			S_1 cleavage	116	88
			F_1 axial plane	292	87
			F_1 fold axis	104	37
MEAM17BSA0129	0707945	5341238	Bedding	293	85
			S_1 cleavage	287	89
MEAM17BSA0130	0708152	5341137	Bedding	110	86
			S_1 cleavage	115	87
			L_1 lineation	095	39
MEAM17BSA0132	0708188	5341082	Bedding	108	86
			S_1 cleavage	112	85
MEAM17BSA0133	0706985	5340744	Bedding	289	87
			S_1 cleavage	102	86
MEAM17BSA0134	0706666	5340466	Bedding	102	89
			S_1 cleavage	110	90
			F_1 axial plane	280	88
			F_1 fold axis	094	33
MEAM17BSA0135	0706581	5340415	Bedding	291	86
			S_1 cleavage	296	85
MEAM17BSA0136	0708908	5340756	S_1 cleavage	105	89
MEAM17BSA0137	0707153	5341881	Bedding	295	86
			S_1 cleavage	290	88

Table 6: (continued).

Station ID	Easting	Northing	Structure Type	Strike	Dip
MEAM17BSA0137	0707153	5341881	S_3 cleavage	257	84
MEAM17BSA0138	0707457	5341937	Bedding	108	85
			S_1 cleavage	102	89
MEAM17BSA0139	0707378	5341938	Bedding	112	82
			S_1 cleavage	098	86
MEAM17BSA0141	0707344	5341972	Bedding	106	85
			S_1 cleavage	104	89
MEAM18BJS0214	0710663	5342708	L_1 lineation	106	54
			S_3 cleavage	083	82
MEAM18BJS0215	0710622	5342669	S_1 cleavage	102	88
			L_1 lineation	109	66
			S_3 cleavage	080	79
MEAM18BJS0216	0710604	5342636	S_1 cleavage	101	86
MEAM18BJS0217	0710482	5342621	Bedding	118	89
			S_1 cleavage	108	88
MEAM18BJS0218	0710458	5342532	Bedding	118	88
			S_1 cleavage	102	89
MEAM18BJS0219	0710445	5342513	Bedding	294	87
			S_1 cleavage	100	89
MEAM18BJS0221	0708774	5343206	Bedding	126	85
			S_1 cleavage	296	87
MEAM18BJS0223	0708735	5343522	S_1 cleavage	116	82
			L_1 lineation	180	74
MEAM18BJS0225	0708686	5343576	S_1 cleavage	126	86
MEAM18BJS0226	0708782	5343006	Bedding	106	88
			S_3 cleavage	264	79
MEAM18BJS0227	0708892	5343025	Bedding	121	87
			S_1 cleavage	100	80
			L_1 lineation	271	68
MEAM18BJS0228	0709057	5343595	S_1 cleavage	119	87
MEAM18BJS0229	0709218	5343608	S_1 cleavage	118	86
MEAM18BJS0230	0709373	5343163	Bedding	295	88
			S_1 cleavage	288	88
MEAM18BJS0231	0709320	5343039	Bedding	294	81
			S_1 cleavage	281	86
MEAM18BJS0232	0706071	5340111	S_1 cleavage	133	86
MEAM18BJS0234	0706329	5340251	Bedding	117	81
			Bedding	296	86
			S_1 cleavage	127	85
			S_1 cleavage	298	87
MEAM18BJS0235	0706410	5340235	Bedding	123	86
			S_1 cleavage	306	87
MEAM18BJS0236	0706659	5340440	Bedding	317	81
			S_1 cleavage	102	88
			F_1 axial plane	111	88
			V_4 vein	099	78
MEAM18BJS0237	0706943	5340709	Bedding	285	85
			S_1 cleavage	281	89
			F_3 fold axis	276	59
			Dextral fracture	020	86

Table 6: (continued).

Station ID	Easting	Northing	Structure Type	Strike	Dip
MEAM18BJS0238	0707156	5340275	Bedding	126	64
			S_3 cleavage	085	84
MEAM18BJS0239	0707045	5340296	Bedding	289	87
			L_1 lineation	098	54
			S_3 cleavage	275	88
			F_3 axial plane	089	84
MEAM18BJS0240	0707123	5340567	Bedding	114	78
			S_1 cleavage	100	84
MEAM18BJS0241	0707083	5340743	Bedding	101	81
			S_3 cleavage	098	86
MEAM18BJS0242	0705434	5340751	S_1 cleavage	119	89
MEAM18BJS0243	0705440	5340752	S_1 cleavage	137	88
MEAM18BJS0244	0705442	5340750	Bedding	136	87
MEAM18BJS0245	0705442	5340752	S_1 cleavage	140	86
MEAM18BJS0246	0705448	5340755	Bedding	129	88
MEAM18BJS0247	0705478	5340764	Bedding	317	83
MEAM18BJS0248	0705498	5340769	Bedding	120	88
MEAM18BJS0249	0705542	5340814	Bedding	301	88
			S_1 cleavage	298	86
			F_3 axial plane	110	86
			F_3 fold axis	285	49
MEAM18BJS0250	0705565	5340851	Bedding	314	76
			S_1 cleavage	293	88
			L_1 lineation	114	60
MEAM18BJS0251	0704797	5341698	Bedding	106	86
			S_1 cleavage	100	89
			S_1 cleavage	287	87
			L_1 lineation	100	72
			F_1 axial plane	102	89
			V_4 vein	293	88
			S_3 cleavage	276	87
MEAM18BJS0252	0704893	5341776	Bedding	120	87
			Bedding	297	89
			Bedding	283	86
			S_1 cleavage	121	88
			S_1 cleavage	305	87
			L_1 lineation	089	62
			F_1 axial plane	119	87
			V_4 vein	293	88
			V_4 vein	297	88
			S_3 cleavage	266	86
MEAM18BJS0253	0704800	5341730	S_1 cleavage	287	87
			S_1 cleavage	289	87
			L_1 lineation	124	52
			L_1 lineation	114	56
			F_1 axial plane	287	89
			V_4 vein	296	88
MEAM18BJS0254	0704816	5341758	Bedding	295	89
			S_1 cleavage	286	86
			L_1 lineation	108	71

Table 6: (continued).

Station ID	Easting	Northing	Structure Type	Strike	Dip
MEAM18BJS0255	0704838	5341780	S_1 cleavage	287	84
			L_1 lineation	092	65
MEAM18BJS0256	0704909	5341792	S_1 cleavage	290	88
			S_3 cleavage	281	84
MEAM18BJS0258	0704910	5341777	Bedding	288	85
MEAM18BJS0259	0704918	5341778	S_1 cleavage	283	87
MEAM18BJS0261	0704944	5341779	Bedding	328	88
MEAM18BJS0262	0704946	5341778	Bedding	258	83
			Bedding	266	86
			Bedding	093	89
			S_1 cleavage	280	86
			F_1 axial plane	105	85
			F_1 fold axis	116	64
			Sinistral fracture	306	99
MEAM18BJS0265	0704940	5341795	S_1 cleavage	106	88
MEAM18BJS0259	0704918	5341778	S_1 cleavage	283	87
MEAM18BJS0261	0704944	5341779	Bedding	328	88
MEAM18BJS0262	0704946	5341778	Bedding	258	83
			Bedding	266	86
			Bedding	093	89
			S_1 cleavage	280	86
			F_1 axial plane	105	85
			F_1 fold axis	116	64
			Sinistral fracture	306	99
MEAM18BJS0265	0704940	5341795	S_1 cleavage	106	88
MEAM18BJS0266	0704941	5341798	Bedding	054	84
MEAM18BJS0269	0704954	5341794	Bedding	116	84
			S_1 cleavage	296	87
MEAM18BJS0270	0705040	5341814	S_1 cleavage	110	85
			S_1 cleavage	301	85
MEAM18BJS0271	0705056	5341799	Bedding	118	86
MEAM18BJS0272	0705071	5341817	Bedding	109	88
			S_3 cleavage	264	86
			F_3 axial plane	266	85
			F_3 fold axis	270	57
MEAM18BJS0273	0705096	5341796	S_1 cleavage	109	88
			S_1 cleavage	285	85
MEAM18BJS0274	0705092	5341817	Bedding	106	87
MEAM18BJS0275	0705093	5341819	S_1 cleavage	303	85
MEAM18BJS0276	0705114	5341806	S_3 cleavage	097	85
MEAM18BJS0277	0705122	5341823	S_1 cleavage	295	88
			L_1 lineation	121	67
MEAM18BJS0278	0705118	5341819	S_1 cleavage	295	88
			F_1 axial plane	294	88
MEAM18BJS0279	0705129	5341809	S_1 cleavage	276	87
MEAM18BJS0280	0705144	5341815	S_1 cleavage	281	83
MEAM18BJS0281	0705146	5341830	S_1 cleavage	107	90
MEAM18BJS0282	0705159	5341839	S_1 cleavage	290	87
MEAM18BJS0283	0705181	5341826	S_1 cleavage	287	82
MEAM18BJS0284	0705269	5341859	S_1 cleavage	287	86

Table 6: (continued).

Station ID	Easting	Northing	Structure Type	Strike	Dip
MEAM18BJS0285	0705321	5341868	S_1 cleavage	286	86
MEAM18BJS0286	0705336	5341851	S_1 cleavage	285	85
			V_4 vein	078	58
MEAM18BJS0287	0705545	5341681	Bedding	276	83
			S_3 cleavage	276	89
MEAM18BJS0288	0705579	5341600	Bedding	270	72
			S_1 cleavage	284	86
MEAM18BJS0289	0705602	5341596	Bedding	270	82
			S_1 cleavage	288	87
MEAM18BJS0290	0705607	5341580	S_1 cleavage	282	86
			S_1 cleavage	286	84
			Z-kink band	238	80
MEAM18BJS0291	0705596	5341572	Bedding	111	81
MEAM18BJS0292	0705651	5341535	Bedding	107	83
			S_1 cleavage	289	83
			F_1 axial plane	293	86
			F_1 fold axis	093	32
MEAM18BJS0293	0705680	5341550	S_1 cleavage	115	87
			F_1 axial plane	108	88
MEAM18BJS0294	0705829	5341568	Bedding	108	83
			Bedding	120	82
			F_1 axial plane	287	88
MEAM18BJS0295	0705818	5341553	Bedding	107	87
			Bedding	120	85
			Bedding	100	84
MEAM18BJS0296	0705888	5341518	Bedding	098	81
			F_1 axial plane	289	88
MEAM18BJS0297	0705840	5341493	Bedding	116	89
			S_1 cleavage	098	81
			V_4 vein	272	88
			Z-kink band	015	86
MEAM18BJS0298	0705887	5341493	S_1 cleavage	110	88
			S_1 cleavage	293	86
MEAM18BJS0299	0705901	5341503	Bedding	092	82
			F_1 axial plane	287	86
MEAM18BJS0300	0705906	5341493	Bedding	270	87
			S_3 cleavage	275	87
			Dextral fracture	149	87
			Sinistral fracture	054	77
MEAM18BJS0301	0705908	5341472	Bedding	281	85
			S_3 cleavage	272	85
MEAM18BJS0302	0705947	5341428	Bedding	103	87
			S_1 cleavage	291	82
MEAM18BJS0303	0705974	5341408	S_1 cleavage	275	88
			F_1 axial plane	285	87
MEAM18BJS0304	0705945	5341406	F_1 axial plane	116	85
MEAM18BJS0305	0705945	5341403	Bedding	101	82
			Bedding	118	83
			Bedding	108	85
			S_1 cleavage	292	88

Table 6: (continued).

Station ID	Easting	Northing	Structure Type	Strike	Dip
MEAM18BJS0306	0705950	5341391	Bedding	286	85
			S_1 cleavage	296	87
			F_1 axial plane	291	81
MEAM18BJS0307	0705996	5341376	Bedding	116	85
			S_1 cleavage	285	87
MEAM18BJS0308	0705525	5340797	Bedding	117	82
			S_1 cleavage	115	89
MEAM18BJS0311	0705565	5340875	Bedding	099	72
			S_1 cleavage	299	87
MEAM18BJS0312	0705557	5340955	Bedding	075	80
			S_1 cleavage	106	82
MEAM18BJS0313	0705536	5340992	Bedding	093	78
			S_1 cleavage	307	88
MEAM18BJS0314	0705383	5341137	S_1 cleavage	304	89
			S_1 cleavage	297	85
			L_1 lineation	109	70
MEAM18BJS0315	0704852	5341284	Bedding	318	90
			L_1 lineation	147	48
MEAM18BJS0316	0704790	5341270	S_1 cleavage	126	84
			S_3 cleavage	276	84
MEAM18BJS0317	0704706	5341291	S_1 cleavage	301	85
MEAM18BJS0318	0704744	5341278	S_1 cleavage	139	84
MEAM18BJS0319	0704786	5341247	S_1 cleavage	293	87
			L_1 lineation	140	61
MEAM18BJS0320	0705205	5341165	S_3 cleavage	095	86
MEAM18BJS0321	0705754	5341035	Bedding	230	79
			V_4 vein	106	87
MEAM18BJS0322	0705746	5341066	Bedding	056	85
			Bedding	311	84
			S_1 cleavage	276	87
			L_1 lineation	124	66
MEAM18BJS0323	0705775	5341111	Bedding	112	90
			S_1 cleavage	109	88
MEAM18BJS0324	0705780	5341115	Bedding	318	87
MEAM18BJS0325	0705795	5341120	S_1 cleavage	284	89
			S_1 cleavage	302	89
MEAM18BJS0326	0705805	5341146	Bedding	292	88
			Bedding	103	87
			Bedding	135	79
			Bedding	103	86
			F_1 axial plane	299	89
			F_1 axial plane	296	88
			F_1 axial plane	298	89
			F_1 fold axis	123	59
MEAM18BJS0327	0705834	5341141	Bedding	309	85
			S_1 cleavage	298	89
			L_1 lineation	119	61
			F_1 axial plane	296	90
MEAM18BJS0328	0705843	5341152	Bedding	299	89
			S_1 cleavage	297	88

Table 6: (continued).

Station ID	Easting	Northing	Structure Type	Strike	Dip
MEAM18BJS0329	0705838	5341169	S_1 cleavage	305	86
MEAM18BJS0330	0705840	5341172	S_1 cleavage	113	89
MEAM18BJS0331	0705880	5341179	Bedding	333	85
MEAM18BJS0332	0705909	5341199	Bedding	306	88
			S_1 cleavage	309	88
			F_1 axial plane	310	89
MEAM18BJS0333	0705919	5341212	Bedding	290	82
			Bedding	324	86
			S_1 cleavage	305	90
			S_1 cleavage	305	86
			F_1 axial plane	311	88
MEAM18BJS0334	0705913	5341231	S_1 cleavage	302	87
MEAM18BJS0335	0705939	5341233	Bedding	295	85
			L_1 lineation	105	45
			F_1 axial plane	302	88
MEAM18BJS0336	0706001	5341337	S_1 cleavage	275	87
			S_1 cleavage	297	88
MEAM18BJS0337	0706582	5340191	Bedding	110	85
			S_1 cleavage	122	87
MEAM18BJS0338	0706641	5340172	Bedding	293	84
MEAM18BJS0339	0706686	5340169	Bedding	297	82
			S_1 cleavage	304	88
MEAM18BJS0340	0706596	5340430	Bedding	281	85
			S_1 cleavage	302	86
			F_1 axial plane	299	85
MEAM18BJS0341	0706669	5340482	Bedding	307	88
			S_1 cleavage	302	86
MEAM18BJS0342	0706751	5340518	Bedding	115	86
			S_1 cleavage	300	86
			L_1 lineation	118	51
MEAM18BJS0343	0707137	5340029	Bedding	108	87
			S_1 cleavage	122	88
MEAM18BJS0344	0707126	5340058	Bedding	288	84
			S_1 cleavage	116	87
MEAM18BJS0345	0707046	5340034	S_1 cleavage	280	88
			L_1 lineation	134	71
MEAM18BJS0346	0706995	5340052	Bedding	108	86
			S_1 cleavage	110	86
MEAM18BJS0347	0706960	5340075	Bedding	109	84
			S_1 cleavage	117	86
MEAM18BJS0348	0706943	5340128	Bedding	117	85
			S_1 cleavage	114	86
MEAM18BJS0349	0707021	5340095	S_1 cleavage	116	88
			S_1 cleavage	135	86
MEAM18BJS0350	0705466	5340879	Bedding	133	85
			S_1 cleavage	311	86
MEAM18BJS0351	0705464	5340898	Bedding	295	90
MEAM18BJS0352	0705459	5340970	Bedding	299	81
			S_1 cleavage	305	86
MEAM18BJS0353	0705436	5341003	Bedding	127	82

Table 6: (continued).

Station ID	Easting	Northing	Structure Type	Strike	Dip
MEAM18BJS0353	0705436	5341003	S_1 cleavage	296	86
MEAM18BJS0354	0705382	5340954	Bedding	318	86
			S_1 cleavage	124	81
MEAM18BJS0355	0705361	5341077	Bedding	116	87
			S_1 cleavage	315	87
MEAM18BJS0356	0705251	5341061	Bedding	306	88
			S_1 cleavage	109	85
MEAM18BJS0357	0705176	5341128	Bedding	299	85
			S_1 cleavage	303	89
MEAM18BJS0359	0704994	5341101	S_1 cleavage	296	87
			S_1 cleavage	285	86
MEAM18BJS0360	0704993	5341100	Bedding	300	89
MEAM18BJS0361	0704993	5341100	Bedding	285	86
			S_1 cleavage	294	87
MEAM18BJS0362	0706153	5341455	Bedding	287	84
			S_1 cleavage	279	83
			V_4 vein	281	84
			Dextral fracture	017	81
MEAM18BJS0363	0706181	5341451	Bedding	284	87
			S_1 cleavage	277	88
MEAM18BJS0364	0706249	5341506	S_1 cleavage	284	87
			S_1 cleavage	285	88
			S-kink band	161	86
MEAM18BJS0365	0706271	5341477	Bedding	291	87
MEAM18BJS0366	0706297	5341557	S_1 cleavage	283	87
			S_1 cleavage	292	88
			Z-kink band	200	83
MEAM18BJS0367	0706303	5341547	Bedding	282	86
MEAM18BJS0368	0706343	5341597	Bedding	287	89
			L_1 lineation	115	51
MEAM18BJS0369	0706343	5341604	Bedding	280	88
			S_1 cleavage	291	88
			V_4 vein	266	85
			S_3 cleavage	094	86
MEAM18BJS0370	0706368	5341649	S_1 cleavage	284	90
			S_1 cleavage	105	86
			V_3 vein	283	90
			V_4 vein	273	85
MEAM18BJS0371	0706376	5341664	Bedding	100	88
			Bedding	284	86
			Bedding	104	86
			Bedding	104	86
			S_1 cleavage	272	85
			S_1 cleavage	105	87
			S_1 cleavage	291	87
			S_1 cleavage	290	83
			S_1 cleavage	101	86
			L_1 lineation	093	36
			L_1 lineation	087	36
			L_1 lineation	101	35

Table 6: (continued).

Station ID	Easting	Northing	Structure Type	Strike	Dip
MEAM18BJS0371	0706376	5341664	L_1 lineation	093	36
			F_1 axial plane	110	67
			V_2 vein	162	66
			V_2 vein	149	63
			V_4 vein	282	84
			V_4 vein	284	90
			V_4 vein	086	84
			V_4 vein	282	89
			V_4 vein	277	84
			V_4 vein	283	82
			Shear bands	291	84
			Dextral fracture	003	82
			Sinistral fracture	049	77
MEAM18BJS0372	0706616	5341630	Bedding	273	88
			Bedding	115	87
			S_1 cleavage	280	84
			V_4 vein	276	86
			Dextral fracture	339	88
MEAM18BJS0373	0706929	5341597	Bedding	114	87
			S_1 cleavage	117	88
			V_4 vein	287	88
			Sinistral fracture	041	84
MEAM18BJS0374	0707064	5341652	Bedding	292	86
			S_1 cleavage	290	87
			V_4 vein	284	89
			S_3 cleavage	252	88
			F_3 axial plane	254	89
			F_3 fold axis	259	58
			Z-kink band	066	85
			S-kink band	170	87
MEAM18BJS0375	0707023	5341581	S_1 cleavage	283	84
MEAM18BJS0376	0707024	5341577	Bedding	297	81
MEAM18BJS0377	0707020	5341517	Bedding	097	87
			S_1 cleavage	291	86
			V_4 vein	277	85
MEAM18BJS0378	0706959	5341438	Bedding	291	83
			Bedding	288	87
			S_1 cleavage	109	85
			S_1 cleavage	286	87
			F_1 axial plane	289	88
			F_1 fold axis	111	60
			V_4 vein	093	85
MEAM18BJS0379	0704780	5341747	Bedding	113	90
			S_1 cleavage	296	88
			L_1 lineation	102	54
MEAM18BJS0381	0704815	5341656	Bedding	283	84
			S_1 cleavage	105	89
			L_1 lineation	151	82
MEAM18BJS0383	0704853	5341679	Bedding	296	85
			Bedding	288	89

Table 6: (continued).

Station ID	Easting	Northing	Structure Type	Strike	Dip
MEAM18BJS0383	0704853	5341679	S_1 cleavage	288	86
			S_1 cleavage	285	85
			L_1 lineation	106	73
MEAM18BJS0384	0704841	5341729	Bedding	283	88
			S_3 cleavage	283	90
MEAM18BJS0386	0704816	5341766	Bedding	283	89
			S_1 cleavage	295	87
			S_3 cleavage	273	87
MEAM18BJS0387	0704831	5341779	Bedding	281	89
			S_1 cleavage	289	86
			L_1 lineation	101	66
			S_3 cleavage	288	82
MEAM18BJS0388	0704857	5341759	Bedding	293	88
			Bedding	287	86
			S_1 cleavage	285	86
			S_1 cleavage	283	86
MEAM18BJS0389	0704842	5341767	S_1 cleavage	283	88
			S_1 cleavage	284	88
MEAM18BJS0390	0704855	5341789	S_1 cleavage	285	86
			L_1 lineation	107	58
MEAM18BJS0391	0704804	5341813	S_1 cleavage	275	88
MEAM18BJS0393	0704841	5341814	S_1 cleavage	284	87
			L_1 lineation	072	78
			S_3 cleavage	274	87
MEAM18BJS0394	0704943	5341816	Bedding	112	84
MEAM18BJS0395	0704906	5341760	Bedding	289	87
			S_1 cleavage	289	87
MEAM18BJS0396	0704886	5341752	Bedding	283	87
			S_1 cleavage	294	88
			L_1 lineation	079	84
MEAM18BJS0397	0706337	5341728	Bedding	287	88
			S_1 cleavage	287	89
MEAM18BJS0398	0706449	5341608	Bedding	281	84
			S_1 cleavage	277	87
MEAM18BJS0399	0706437	5341624	Bedding	286	87
			S_1 cleavage	105	80
MEAM18BJS0400	0706348	5341544	Bedding	097	79
			S_1 cleavage	291	88
MEAM18BJS0401	0706551	5341471	S_1 cleavage	100	88
			S_1 cleavage	282	86
MEAM18BJS0402	0706567	5341573	S_3 cleavage	087	88
MEAM18BJS0407	0708167	5341143	Bedding	289	86
			Bedding	286	84
			Bedding	289	84
			Bedding	289	90
			Bedding	291	86
			Bedding	290	87
			Bedding	286	84
			Bedding	289	87
			Bedding	290	87

Table 6: (continued).

Station ID	Easting	Northing	Structure Type	Strike	Dip
MEAM18BJS0407	0708167	5341143	S_1 cleavage	281	81
			S_1 cleavage	279	88
			S_1 cleavage	279	90
			S_1 cleavage	285	86
			S_1 cleavage	283	86
			S_1 cleavage	271	86
			S_1 cleavage	280	84
			S_1 cleavage	285	89
			L_1 lineation	105	51
			L_1 lineation	103	51
			L_1 lineation	100	56
			L_1 lineation	101	45
			L_1 lineation	109	43
			F_1 axial plane	280	80
			F_1 axial plane	102	86
			F_1 fold axis	109	33
			V_1 vein	096	79
			V_1 vein	102	84
			V_1 vein	101	75
			V_1 vein	287	85
			V_1 vein	280	87
			V_1 vein	288	89
			V_2 vein	219	55
			V_2 vein	230	55
			V_2 vein	192	53
			V_2 vein	178	66
			V_2 vein	204	63
			V_2 vein	195	51
			V_2 vein	193	46
			V_2 vein	182	39
			V_2 vein	186	65
			V_2 vein	195	51
			V_3 vein	079	66
			V_3 vein	083	59
			V_3 vein	086	57
			V_3 vein	078	65
			V_3 vein	094	62
			V_3 vein	102	77
			V_3 vein	074	83
			V_3 vein	314	85
			V_3 vein	074	83
			V_4 vein	252	82
			V_4 vein	286	88
			V_4 vein	281	82
			V_4 vein	284	87
			S_3 cleavage	270	85
			S_3 cleavage	269	81
			F_3 axial plane	086	76
			Shear bands	119	83
			Shear bands	133	81

Table 6: (continued).

Station ID	Easting	Northing	Structure Type	Strike	Dip
MEAM18BJS0407	0708167	5341143	Shear bands	145	83
			Shear bands	132	82
			Shear bands	129	83
			Shear bands	130	85
			Shear bands	127	84
			Shear bands	128	85
			Shear bands	130	82
			Shear bands	116	84
			Shear bands	122	81
			Shear bands	128	78
			Shear bands	109	78
			Shear bands	139	80
			Shear bands	127	83
MEAM18BJS0416	0707351	5342920	Bedding	098	84
			Bedding	111	88
MEAM18BJS0417	0707311	5342953	Bedding	109	86
			S_3 cleavage	085	87
MEAM18BJS0418	0707249	5342979	Bedding	294	87
			S_1 cleavage	109	87
MEAM18BJS0419	0707219	5342953	Bedding	106	86
			S_1 cleavage	287	86
MEAM18BJS0420	0707225	5342927	Bedding	110	88
			S_1 cleavage	101	87
MEAM18BJS0421	0707115	5342802	Bedding	280	85
			S_1 cleavage	104	88
MEAM18BJS0422	0707074	5342715	Bedding	112	87
			S_3 cleavage	274	88
MEAM18BJS0423	0706043	5342279	S_1 cleavage	101	88
			S_1 cleavage	114	87
MEAM18BJS0424	0706182	5342257	Bedding	107	86
			L_1 lineation	122	53
			S_3 cleavage	091	86
MEAM18BJS0425	0706211	5342249	Bedding	091	84
MEAM18BJS0426	0706257	5342242	Bedding	095	84
			S_3 cleavage	085	83
MEAM18BJS0427	0706380	5342350	Bedding	289	88
			S_3 cleavage	088	85
MEAM18BJS0428	0706271	5342360	Bedding	110	85
			S_1 cleavage	282	87
MEAM18BJS0429	0706237	5342362	Bedding	118	86
			S_1 cleavage	105	86
MEAM18BJS0430	0706028	5342278	Bedding	114	86
			S_1 cleavage	111	84
MEAM18BJS0431	0705855	5342075	Bedding	115	87
			S_1 cleavage	108	88
MEAM18BJS0432	0705832	5342036	Bedding	114	89
			S_1 cleavage	107	88
MEAM18BJS0433	0705763	5342043	Bedding	280	86
			S_1 cleavage	105	87
MEAM18BJS0434	0705644	5342064	Bedding	295	87

Table 6: (concluded).

Station ID	Easting	Northing	Structure Type	Strike	Dip
MEAM18BJS0434	0705644	5342064	S_1 cleavage	276	87
MEAM18BJS0435	0705689	5342080	Bedding	284	88
			S_1 cleavage	300	88
MEAM18BJS0436	0705584	5342080	S_1 cleavage	116	86
			S_3 cleavage	279	85
MEAM18BJS0437	0705467	5342057	Bedding	114	85
			L_1 lineation	122	61
MEAM18BJS0438	0705470	5342147	Bedding	292	88
			S_1 cleavage	106	85
MEAM18BJS0440	0705549	5342108	S_1 cleavage	294	85
			S_1 cleavage	284	87
MEAM18BJS0441	0705885	5342130	Bedding	288	88
MEAM18BJS0442	0705835	5342176	S_1 cleavage	286	87
MEAM18BJS0437	0705467	5342057	Bedding	114	85
			L_1 lineation	122	61
MEAM18BJS0438	0705470	5342147	Bedding	292	88
			S_1 cleavage	106	85
MEAM18BJS0440	0705549	5342108	S_1 cleavage	294	85
			S_1 cleavage	284	87
MEAM18BJS0441	0705885	5342130	Bedding	288	88
MEAM18BJS0442	0705835	5342176	S_1 cleavage	286	87

Note: Coordinates in UTM Zone 17 NAD 83.

5. Appendix C: Summary of Field Work Publications

5.1. 2017 Summary of Field Work

Structural geology of the Timiskaming and Cadillac groups along the Malartic segment of the Larder Lake–Cadillac deformation zone and implications for gold mineralization, Abitibi greenstone belt, northwestern Quebec

Brendon Samson, Xiaohui Zhou and Bruno Lafrance

Mineral Exploration Research Centre, Harquail School of Earth Sciences, Laurentian University, Sudbury, Ontario, P3E 2C6

INTRODUCTION

The Larder Lake–Cadillac deformation zone (LLCDZ; Figure 1) in the Abitibi greenstone belt of the Archean Superior Province is a major crustal-scale deformation zone hosting numerous world-class gold deposits. Little work has been done on gold mineralization hosted by metasedimentary rocks of the Timiskaming and Cadillac groups along the Malartic segment of the LLCDZ due to the lack of outcrops. However, new outcrops stripped mechanically by Midland Exploration Inc. over the last two years provide a great opportunity to study gold mineralization in this prospective district. An area along the Malartic segment of the LLCDZ (Figure 2) was mapped in the summer of 2017 as part of the Malartic seismic-transect mapping project of the Metal Earth initiative. The goals of the 2017 mapping project were to establish the structural history of the supracrustal rocks, determine the structural timing of gold- bearing quartz veins and establish the relationship between the Timiskaming Group and Cadillac group in the study area. This report focuses on the structural evolution of these rocks and their gold-bearing veins.

REGIONAL SETTING

The Abitibi greenstone belt comprises volcanic and sedimentary assemblages intruded by large granitoid bodies. Four volcanic units occur in close proximity to the LLCDZ: the Piché (>2709 Ma; Pilote et al., 2014), Malartic (2714–2702 Ma; Pilote et al., 1997, 1998, 1999), Louvicourt (2704 Ma; Pilote et al., 2014) and Blake River (2703–2695 Ma; Corfu et al., 1989, 1993; Mortensen, 1993; Moore et al., 2016) groups (Bedeaux et al., 2017). The Piché group occurs along the LLCDZ and consists mainly of strongly deformed ultramafic and mafic volcanic rocks (Latulippe, 1976; Simard et al., 2013), with minor intermediate andesitic rocks (Landry, 1991). All the other groups consist of ultramafic and mafic volcanic rocks intercalated with minor intermediate to felsic volcanic rocks, with the exception of the Blake River group, which consists mostly of mafic and felsic volcanic rocks (Bedeaux et al., 2017).

Two Archean sedimentary successor basins overly the volcanic assemblages (Figure 1; Thurston et al., 2008). Rocks of the Cadillac group (Dimroth et al., 1982) occupy a 150 by 5 km basin unconformably overlying older volcanic rocks of the Blake River group, north of the LLCDZ (Goutier, 1997; Lafrance et al., 2003; Mercier-Langevin et al., 2007; Thurston et al.,

2008). The Cadillac group was deposited <2686 Ma ago (Davis, 2002) and is equivalent to the Porcupine group in Ontario (Ayer et al., 2002; Thurston et al., 2008). Younger (<2676 Ma) fluvial conglomerate, sandstone and shallow marine turbidites of the Timiskaming Group were unconformably deposited over the Cadillac group (Corfu and Davis, 1991; Davis, 2002; Pilote et al., 2015).

The Pontiac Subprovince, which lies immediately south of the LLCDZ and the Abitibi greenstone belt, consists of turbiditic sandstone and minor conglomerate (Goulet, 1978; Dimroth et al., 1982). It was deposited between ca. 2685 Ma, the age of the youngest detrital zircons in the metasandstone of the northern part of the Pontiac Subprovince, and ca. 2682 Ma, the crystallization age of the Lac Fournière pluton that intruded Pontiac metasedimentary rocks. It is similar in age and rock type to the Cadillac group (Mortensen, 1993; Davis, 2002).

LITHOLOGICAL UNITS IN THE STUDY AREA

The Cadillac and Timiskaming groups are the two main rock assemblages in the study area (Figure 3). The Cadillac group consists of turbiditic sandstone, with minor iron formation. Individual sandstone beds are 2–20 cm thick, generally top to the north or south, based on normal grading, andalternate with mudstone beds 1–5 cm thick. The Timiskaming Group includes polymictic conglomerate, sandstone and minor turbidites. Polymictic conglomerate beds, typically 1–5 m thick, contain clasts of mafic and felsic volcanic and granitoid rocks, minor chert and smoky quartz clasts. Sandstone beds are massive to trough crossbedded and metres thick. Erosional channelling at the base of conglomeratic beds, normal grading in turbidite beds and trough crossbedding in sandstone bedding suggest younging direction is generally to the north. Younging reversals are commonly present due to well-developed isoclinal folds.

DEFORMATION, ALTERATION AND MINERALIZATION

Regional Folding

A regional cleavage strikes west-northwest and dips steeply to the north and locally to the south. It is expressed as a continuous slaty cleavage in mudstone, as a spaced disjunctive cleavage in sandstone, and by the flattening and elongation of clasts in conglomerate (Figure 4a). It is oriented anticlockwise to north-facing beds and clockwise to south-facing beds. The cleavage is axial planar to west-northwest- striking folds plunging moderately to shallowly to the east-southeast. The folds are tight to isoclinal, with amplitudes varying in size from centimetres to metres (Figure 4b). An intersection lineation defined by the intersection of bedding with the regional cleavage plunges moderately to the east-southeast, parallel to the fold axes. Younging reversals within the Timiskaming and Cadillac groups, the presence of S- and Z-shaped asymmetrical folds and changes in structural facing of the regional cleavage suggest that the Cadillac and Timiskaming groups were overprinted by regional folds, with amplitudes measuring metres to hundreds of metres.

Sinistral Movement

Arrays of en échelon quartz veins crosscut bedding and the regional cleavage (Figure 4c, d). The veins are typically 5–30 cm thick and vary in length from a few metres to hundreds of metres. They are oriented anticlockwise to bedding and to the regional cleavage on both limbs of

the regional folds. The orientation of these veins and the presence of sigmoidal S-shaped tension gashes (Figure 4e), with similar orientation as the en échelon quartz veins, suggest that these veins were emplaced during sinistral shearing. The veins are present on several outcrops, suggesting that this sinistral shearing event was not a localized deformation event.

The veins are surrounded by chlorite+sericite+biotite+arsenopyrite alteration haloes that extend over 10–20 cm in the wallrocks. Assays of the veins and their alteration haloes returned values of 1.7–41 g/t Au (Midland Exploration Inc., 2016).

Dextral Movement

The en échelon veins are boudinaged (Figure 4d, f), cut by dextral shear bands (Figure 4f) and overprinted by Z-shaped folds (Figure 4g). The shear bands are steeply dipping and strike to the northwest. The Z-folds range in amplitude from 10 to 30 cm and are generally steeply dipping, east- to east-northeast-striking and moderately east-plunging. They have an axial plane cleavage expressed as a fine differentiated foliation, which is oriented anticlockwise to bedding. Some Z-shaped flanking folds are present adjacent to the quartz veins (Figure 5a). These structures are well-developed in the turbiditic sandstone and collectively suggest that the quartz veins were deformed during a superposed younger dextral shear event. The occurrence of Z-shaped tension gashes (Figure 5b) with similar orientation to the dextral shear band also suggests emplacement during dextral shearing. Granitic clasts in the Timiskaming conglomerate are surrounded by asymmetrical dextral strain shadows (Figure 5c), suggesting that the conglomerate was also deformed during dextral shearing.

DISCUSSION AND CONCLUSION

Gold mineralization at the nearby Canadian Malartic mine is controlled by the Sladen fault and by other faults and shear zones that cut the hinge of major folds (De Souza et al., 2015). The mineralized zones are oriented subparallel to the northwest-striking axial planar cleavage to the folds and to the east- striking and south-dipping Sladen fault. The gold mineralization was emplaced within these faults and shear zones as a result of the remobilization of gold that was introduced earlier through a magmatic or hydrothermal system related to porphyritic intrusions of Timiskaming age (De Souza et al., 2015).

The faults associated with gold mineralization at the Canadian Malartic deposit have reverse sinistral-slip kinematics and a moderately to steeply northeast-plunging lineation (De Souza et al., 2015). As the gold-bearing veins in the study area also formed during a sinistral shearing event, they may be coeval with the mineralization at the Canadian Malartic deposit. This interpretation will be investigated further during a follow-up field season.

FUTURE WORK

The northern contact of the Timiskaming Group with the Cadillac group is not well understood. The older Cadillac turbidites are located north of a sequence of Timiskaming conglomerate and crossbedded sandstone but as both are younging to the north, this contact must either be tectonic or conformable. Should the latter prove the case, the turbidites correspond to the marine facies of the Timiskaming Group, as described by Hyde (1980) for the Kirkland Lake–Larder Lake area. Samples were collected from both groups and will be submitted for lithogeochemicalanalysis and detrital-zircon geochronology to compare their

geochemistry and zircon populations.

The focus of the 2018 field season will be to examine the stratigraphic and structural setting of gold mineralization within the metasedimentary rocks of the Timiskaming and Cadillac groups in a larger area north of the LLCDZ. Contacts between the Cadillac and Timiskaming groups with the Blake River and Piché groups will also be investigated.

ACKNOWLEDGMENTS

Gino Roger, President and CEO of Midland Exploration Inc., and Marie-France Bugnon, General Manager Exploration of IAMGOLD Corp. are thanked for allowing access to the Héva East property. The authors are grateful for the help received from Pierre Pilote and James Moorhead of the Ministère de l'Énergie et des Ressources naturelles (Quebec), as well as Réal Daigneault from the Université du Québec à Chicoutimi with the development of this project. Lastly but not least, Michelle Jacques is thanked for her hard work and assistance throughout the field season.

Harquail School of Earth Sciences, Mineral Exploration Research Centre contribution MERC- ME2017-007.

REFERENCES

Ayer, J., Amelin, Y., Corfu, F., Kamo, S., Ketchum, J., Kwok, K. and Trowell, N. 2002. Evolution of the southern Abitibi greenstone belt base on U-Pb geochronology: autochthonous volcanic construction followed by plutonism, regional deformation and sedimentation; Precambrian Research, v. 115, p. 63–95.

Bedeaux, P., Pilote, P., Daigneault, R. and Rafini, S. 2017. Synthesis of the structural evolution and associated gold mineralization of the Cadillac Fault, Abitibi, Canada; Ore Geology Reviews; v. 82, p. 49–69.

Corfu, F. and Davis, D.W. 1991. Archean hydrothermal zircon in the Abitibi greenstone belt–constraints on the timing of gold mineralization–comment; Earth and Planetary Science Letters, v. 104, p. 545–552.

Corfu, F., Krogh, T.E., Kwok, Y.Y. and Jensen, L.S. 1989. U–Pb zircon geochronology in the southwestern Abitibi greenstone belt, Superior Province; Canadian Journal of Earth Sciences, v. 26, p. 1747–1763.

Corfu, F., Spooner, E.T.C. and Barrie, C.T. 1993. The evolution of the southern Abitibi greenstone belt in light of precise U-Pb geochronology; Economic Geology, Buletin of the Society of Economic Geologists, v. 88,

p. 1323–1340.

Davis, D.W. 2002. U-Pb geochronology of Archean metasedimentary rocks in the Pontiac and Abitibi subprovinces, Quebec, constraints on timing, provenance and regional tectonics; Precambrian Research, v. 115, p. 97–117.

De Souza, S.P., Gaillard, N., Piette-Lauzière, N., Mir, R., Bardoux, M., Olivo, G.R., Linnen, R.L., Bérubé, C.L., Lypaczewski, P., Guilmette, C., Feltrin, L. and Morris, W.A. 2015. Structural setting for Canadian Malartic style of gold mineralization in the Pontiac Subprovince, south of the Cadillac Larder Lake Deformation Zone, Québec, Canada; Ore Geology Reviews, v. 84, p. 185–201.

Desrochers, J.P. and Hubert, C. 1996. Structural evolution and early accretion of the Archean Malartic Composite Block, southern Abitibi greenstone belt, Quebec, Canada Canadian Journal of Earth Sciences, v. 33, p. 1556–1569.

Desrochers, J.P., Hubert, C., Ludden, J.N. and Pilote, P. 1993. Accretion of Archean oceanic plateau fragments in the Abitibi greenstone-belt, Canada; Geology, v. 21, p. 451–454.

Dimroth, E., Imreh, L., Rocheleau, M. and Goulet, N. 1982. Evolution of the south-central part of the Archean Abitibi Belt, Quebec. Part I: stratigraphy and paleogeographic model; Canadian Journal of Earth Sciences, v. 19, p. 1729–1758.

Goulet, N. 1978. Stratigraphy and structural relationships across the Cadillac-Larder Lake Fault, Rouyn-Beauchastel area, Quebec; Ph.D. thesis, Queen's University, Ontario, Canada.

Goutier, J. 1997. Géologie de la région de Destor; Ministère des Ressources naturelles du Québec, rapport RG 96-13, 37 p.

Hubert, C., Trudel, P. and Gelinas, L. 1984. Archean wrench fault tectonics and structural evolution of the Blake River group, Abitibi belt, Quebec; Canadian Journal of Earth Sciences, v. 21, 1024–1032.

Hyde, R.S. 1980. Sedimentary facies in the archean Timiskaming Group and their tectonic implications, Abitibi Greenstone-Belt, Northeastern Ontario, Canada; Precambrian Research, v. 12, p. 161–195.

Imreh, L. 1984. Sillon de la Motte-Vassan et son avant-pays méridional; synthèse volcanologique, lithostratigraphique et gîtologique; *in* The La Motte-Vassan Structure and its southern foreland; volcanologic, lithostratigraphic and economic synthesis, Ministère des Ressources naturelles; MM 82-04. 72 p.

Lafrance, B., Moorhead, J. and Davis, D.W. 2003. Cadre géologique du camp minier de Doyon-Bousquet-Laronde: Ministère des Ressources naturelles, de la Faune et des Parcs du Québec, rapport ET 2002-07, 43 p.

Landry, J. 1991. Volcanologie physique et sédimentologie du groupe volcanique de Piché et relations stratigraphiques avec les groupes sédimentaires encaissants de Pontiac et de Cadillac; unpublished M.Sc. thesis, Université du Québec à Chicoutimi, Quebec, Canada.

Latulippe, M. 1976. Excursion géologique: la région de Val-d'Or-Malartic; Ministère des Richesses naturelles du Québec (ed.), Institut canadien des mines et de la métallurgie.

Mercier-Langevin, P., Dubé, B., Hannington, M.D., Richer-Laflèche, M. and Gosselin, G. 2007. The LaRonde Penna Au-rich volcanogenic massive sulfide deposit, Abitibi greenstone belt, Quebec: Part II. Lithogeochemistry and paleotectonic setting; Economic Geology, v. 102, p. 611–631.

Midland Exploration Inc. 2016. Midland continues to discover several new gold-bearing zones on its Heva project, with grades up to 41.0 g/t Au by prospecting; retrieved from URL http://www.midlandexploration.com/en/Communique.aspx?ResourceId=31fa1039-8a5a-4807-a8c7-2ea5bc814052 [last accessed: September 2017].

Moore, L.N., Daigneault, R., Aird, H.M., Banerjee, N.R. and Mueller, W.U. 2016. Reconstruction and evolution of Archean intracaldera facies: the Rouyn- Pelletier Caldera Complex of the Blake River Group, Abitibi greenstone belt, Canada; Canadian Journal of Earth Sciences, v. 53, p. 355–377.

Mortensen, J.K. 1993. U-Pb geochronology of the eastern Abitibi Subprovince. Part 2: Noranda–Kirkland Lake area; Canadian Journal of Earth Sciences, v. 30, p. 29–41.

Pilote, P. 2013. Géologie Malartic, 32D01-NE; Ministère de l'Énergie et des Ressources naturelles du Québec, CG-32D01D-2013-01.

Pilote, P., Daigneault, R., David, J. and McNicoll, V. 2014. L'architecture des groupes de Malartic, de Piché et de Cadillac et de la Faille de Cadillac, Abitibi: révision géologique, nouvelles datations et interprétations; Ministère de l'Énergie et des Ressources du Québec, DV 2015-03.

Pilote, P., Daigneault, R., David, J. and McNicoll, V. 2015. Architecture of the Malartic, Piché and Cadillac groups and the Cadillac Fault: geological revisions, new dates and interpretations; *in* Abstracts of Oral Presentations and Posters, Québec Mines, 2014, Ministère de l'Énergie et des Ressources naturelles, 37 p.

Pilote, P., Mueller, W., Moorehead, J., Scott, C. and Lavoie, S. 1997. Géologie, volcanologie et lithogéochimie des formations de Val-d'Or et d'Héva, district de Val-d'Or, sous-province de l'Abitibi; *in* Vers de nouvelles découvertes, séminaire d'information sur la recherche géologique, programme et résumés, 1997.

Gouvernement du Québec, Ministère des Ressources naturelles, Institut Canadien des Mines, Québec, QC, Canada, p. 47. DV 97-03.

Pilote, P., Mueller, W.U., Parent, M., Machado, N., Moorhead, J., Scott, C.R. and Lavoie, S. 1998. Géologie et volcanologie des formations Val-d'Or et Héva, district de Val-d'Or, sous-province de l'Abitibi, Québec : contraintes géochimiques et géochronologiques; Program with Abstracts, GAC, MAC, CGU Joint Annual Meeting 23, p. 146–147.

Pilote, P., Scott, C.R., Mueller, W., Lavoie, S. and Riopel, P. 1999. Géologie des formations de Val-d'Or, Héva et Jacola: nouvelle interprétation du groupe de Malartic; *in* Explorer au Québec : le défi de la connaissance;

Séminaire d'information sur la recherche géologique, programme et résumés, 1999, Ministère de l'Énergie et des Ressources, DV 99-03, 52 p.

SIGÉOM. c2003–2017. Québec (QC) ; Gouvernement du Québec, URL http://sigeom.mines.gouv.qc.ca/signet/classes/I1102_indexAccueil?l=a# [last accessed: September 2017].

Simard, M., Gaboury, D., Daigneault, R. and Mercier-Langevin, P. 2013. Multistage gold mineralization at the Lapa mine, Abitibi Subprovince: insights into auriferous hydrothermal and metasomatic processes in the Cadillac-Larder Lake Fault Zone; Mineral Deposits, v. 48, p. 883–905.

Thurston, P.C., Ayer, J.A., Goutier, J. and Hamilton, M.A. 2008. Depositional gaps in Abitibi greenstone belt stratigraphy: a key to exploration for syngenetic mineralization; Economic Geology, v. 103, p. 1097–1134.

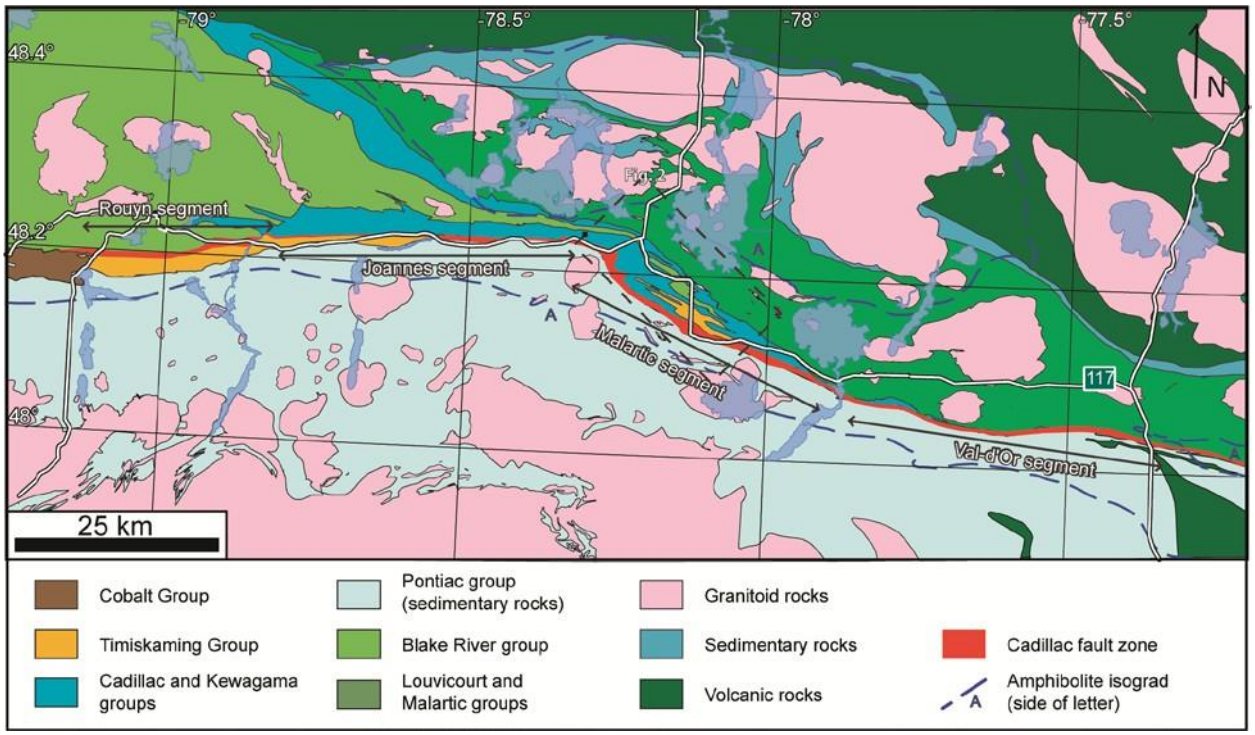

Figure 1. Regional geology, showing the four fault segments of the Larder Lake–Cadillac deformation zone in the Abitibi greenstone belt. Modified from Hubert et al. (1984), Imreh (1984), Desrochers and Hubert (1996), and Bedeaux et al. (2017).

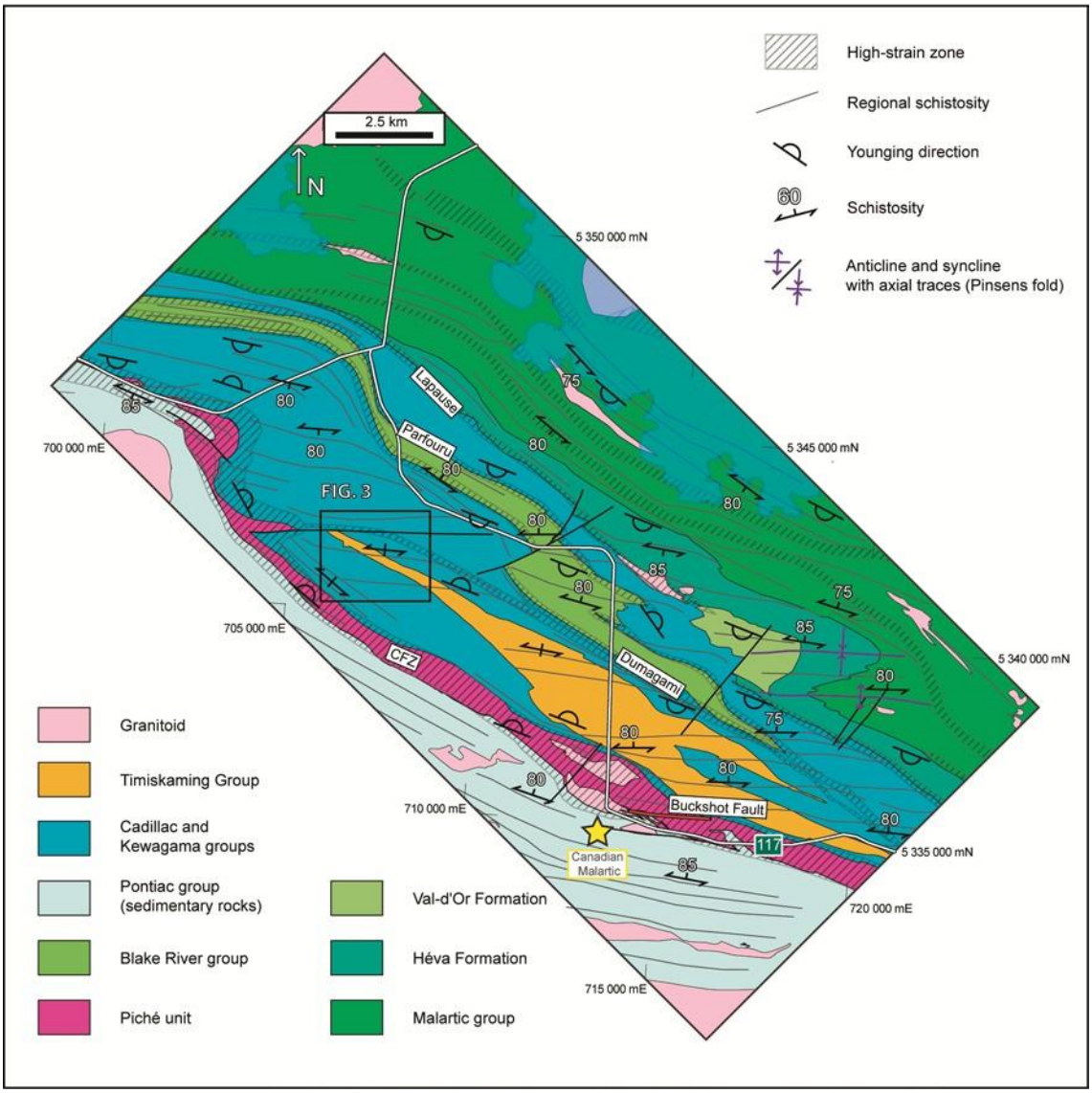

Figure 2. Geology of the Malartic segment of the Larder Lake–Cadillac deformation zone in the Abitibi greenstone belt. Modified from Desrochers et al. (1993), Desrochers and Hubert (1996), Pilote et al. (1999), Pilote (2013), Pilote et al. (2014), and Bedeaux et al. (2017). Abbreviation: CFZ, Cadillac fault zone.

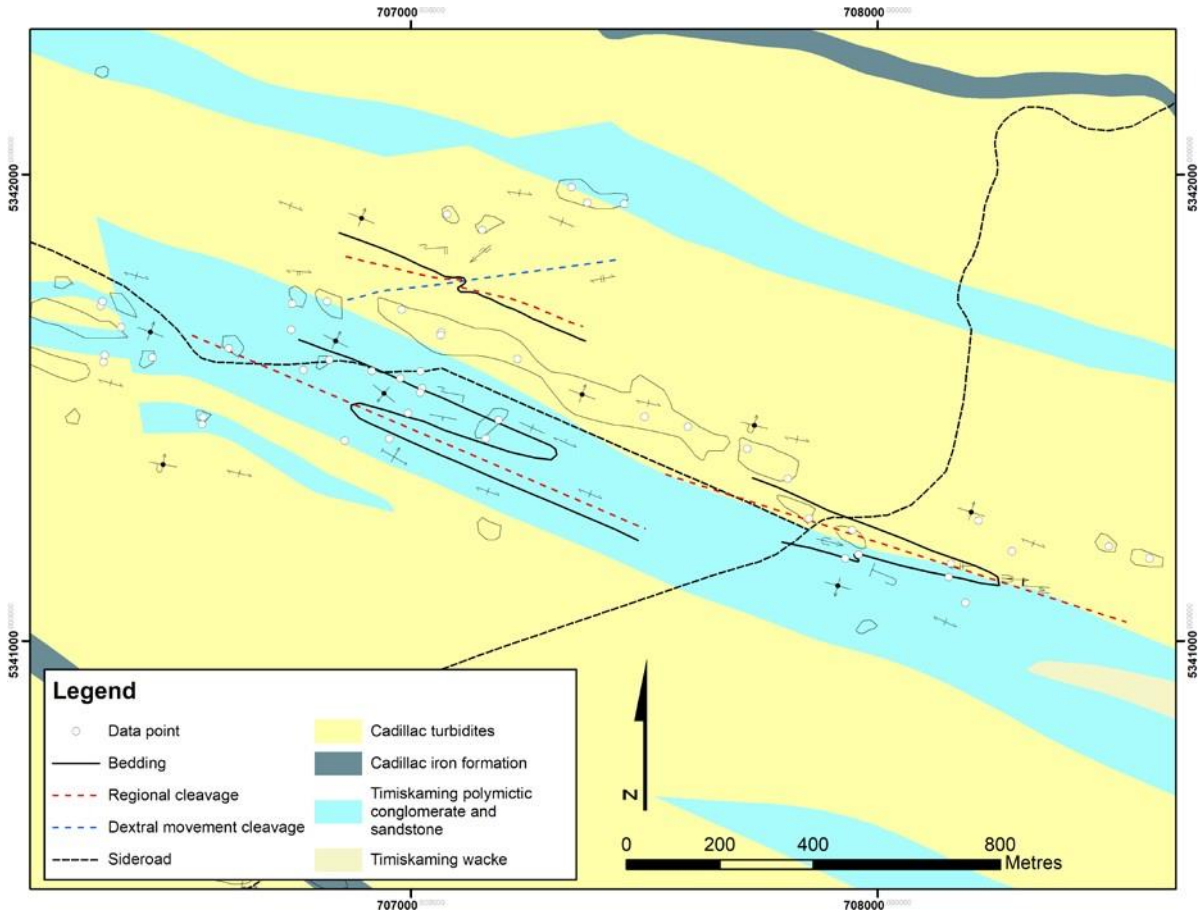

Figure 3. Geology of the study area of the Cadillac and Timiskaming groups within the Malartic segment of the Larder Lake–Cadillac deformation zone in the Abitibi greenstone belt (modified from interactive map developed by SIGÉOM, 2017).

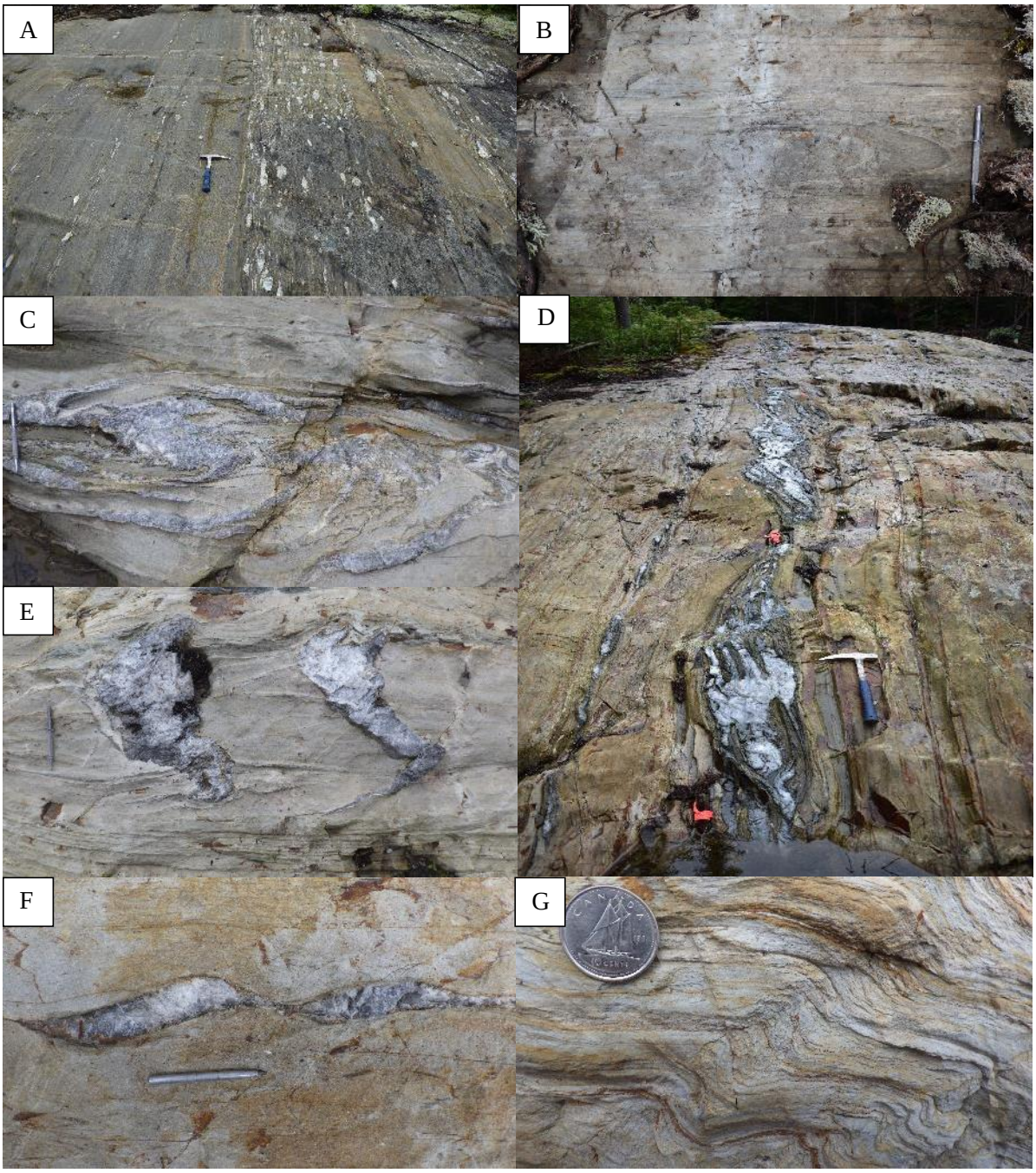

Figure 4. Selected photos of structural features in the Abitibi greenstone belt study area, showing **a)** Timiskaming polymictic conglomerate and bedded sandstone at UTM 706379E, 5341672N (flattened clasts of the conglomerate define regional cleavage); **b)** isoclinal U-shaped folds developed during regional folding within the Cadillac turbidites at UTM 707958E, 5341185N; **c)** S-folded en échelon quartz vein at UTM 708156E, 5341165N; **d)** S-folded and boudinaged gold-bearing en échelon quartz veins at UTM 708156E, 5341165N; **e)** S-folded quartz tension gashes at UTM 708156E, 5341165N; **f)** boudinaged quartz veins along a dextral shear-band cleavage at UTM 708156E, 5341165N; **g)** dextral movement Z-folds with an axial planar cleavage at UTM 708156E, 5341165N. All co-ordinates are in NAD83 UTM Zone 17N. Hammer is 33 cm long and pen magnet is 13 cm long.

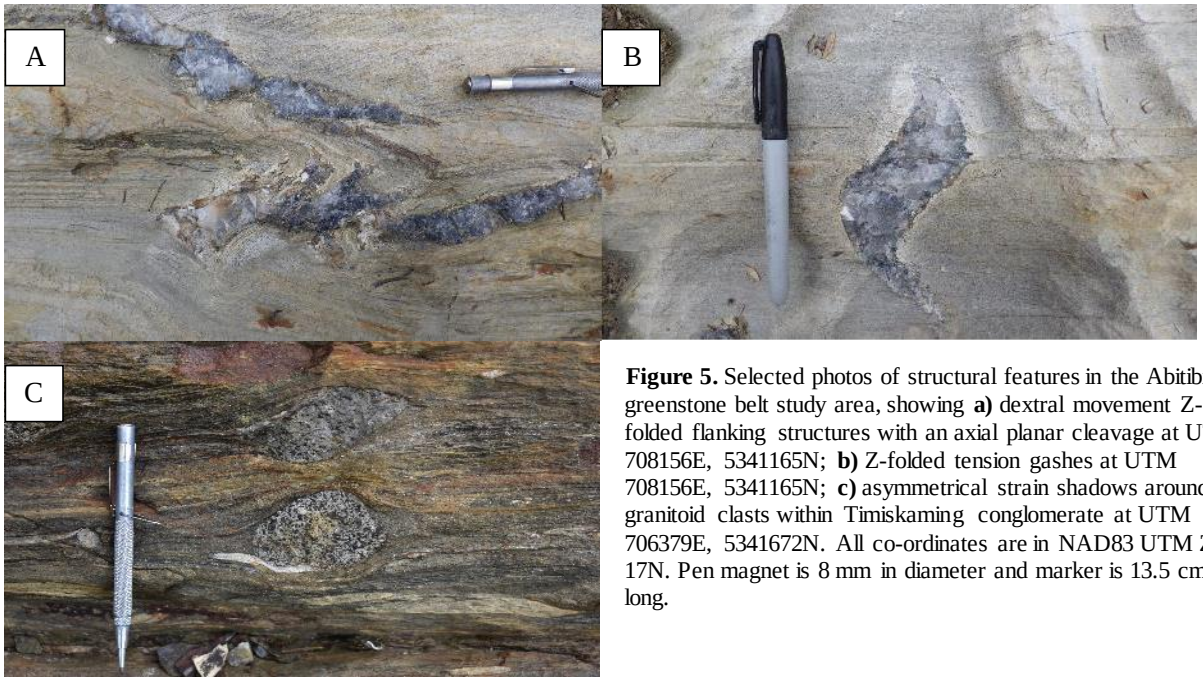

Figure 5. Selected photos of structural features in the Abitibi greenstone belt study area, showing **a)** dextral movement Z-folded flanking structures with an axial planar cleavage at UTM 708156E, 5341165N; **b)** Z-folded tension gashes at UTM 708156E, 5341165N; **c)** asymmetrical strain shadows around granitoid clasts within Timiskaming conglomerate at UTM 706379E, 5341672N. All co-ordinates are in NAD83 UTM Zone 17N. Pen magnet is 8 mm in diameter and marker is 13.5 cm long.

5.2. 2018 Summary of Field Work

Regional Folding, Quartz Veining and Gold Mineralization in a Metasedimentary Basin along the Malartic Segment of the Larder Lake–Cadillac Deformation Zone, Abitibi Greenstone Belt, Quebec

B. Samson, B. Lafrance and X. Zhou

Mineral Exploration Research Centre, Harquail School of Earth Sciences, Laurentian University, Sudbury, Ontario, P3E 2C6

INTRODUCTION

The Larder Lake–Cadillac deformation zone (LLCDZ; Figure 1) in the Abitibi greenstone belt of the Archean Superior Province is a major crustal-scale deformation zone hosting numerous world-class gold deposits. Little work has been done on gold mineralization within the metasedimentary basin along the Malartic segment of the LLCDZ due to the lack of outcrop. However, new outcrops stripped mechanically by Midland Exploration Inc. and IAMGOLD Corp. over the last three years, as well as logging in the fall of 2017, provide a new opportunity to study gold mineralization in this prospective district. An area along the Malartic segment of the LLCDZ (Figure 2) was mapped in the summer of 2018 as part of the Malartic seismic-transect mapping project of the Metal Earth research initiative.

The goals of this 2018 mapping project were to confirm the structural history of the basin, determine the relative timing of the quartz veining and establish the significance of a newly found quartz-feldspar porphyry along the LLCDZ. This report summarizes preliminary results from the field mapping, with emphasis on the structural history of the supracrustal rocks, the gold-bearing veins and their relative timing with respect to regional folding.

REGIONAL SETTING

The Abitibi greenstone belt comprises volcanic and sedimentary assemblages intruded by large granitoid bodies. Four volcanic units occur in close proximity to the LLCDZ: the Piché (2709–2706 Ma; Pilote et al., 2015), Malartic (2714–2704 Ma; Pilote et al., 1999, 2015), Louvicourt (2704 Ma; Pilote et al., 1999, 2015) and Blake River (2703–2695 Ma; Corfu et al., 1989, 1993; Mortensen, 1993; McNicoll et al., 2014) groups (Bedeaux et al., 2017). The Piché group occurs along the LLCDZ and consists mainly of strongly deformed ultramafic and mafic volcanic rocks (Latulippe, 1976; Simard et al., 2013), with minor intermediate andesitic rocks (Landry, 1991). The Malartic group consists of ultramafic and mafic volcanic rocks intercalated with minor intermediate to felsic volcanic rocks, whereas the Louvicourt and Blake River groups consist mostly of mafic and felsic volcanic rocks (Bedeaux et al., 2017).

Two Archean metasedimentary basins along the Malartic segment of the LLCDZ overlie the volcanic units (Thurston et al., 2008; Figure 1). Rocks of the Cadillac group (Dimroth et al., 1982) were deposited in a basin, now exposed over a 150 by 5 km area, unconformably overlying older volcanic rocks of the Blake River group, north of the LLCDZ (Goutier, 1997; Lafrance et al., 2003; Mercier-Langevin et al., 2007, Thurston et al., 2008). The Cadillac group was deposited at ca. 2686 Ma (Mortensen 1993; Davis, 2002) and is equivalent to the Porcupine Assemblage in Ontario (Ayer et al., 2002; Thurston et al., 2008). The Cadillac basin is in turn unconformably overlain by younger fluvial

conglomerate, sandstone and shallow marine turbidites of the ca. 2677–2672 Ma Timiskaming Group (Corfu and Davis, 1991; Davis, 2002; Pilote et al., 2015).

The Pontiac Subprovince, which lies immediately south of the LLCDZ and the Abitibi greenstone belt, consists of turbiditic sandstone, minor conglomerate, iron formation, and ultramafic and mafic rocks (Goulet, 1978; Dimroth et al., 1982; Perrouty et al., 2017). Metasedimentary rocks were deposited between ca. 2685 Ma, the age of the youngest detrital zircons in sandstone, and ca. 2682 Ma, the crystallization age of the crosscutting Lac Fournière pluton.

LITHOLOGICAL UNITS AND REGIONAL STRUCTURES

The Cadillac group consists of interlayered turbiditic sandstone and mudstone. Younging indicators include erosional channelling at the base of conglomeratic beds and normal grading in sandstone beds. The younger Timiskaming Group includes alternating horizons of polymictic conglomerate (Figure 3a) and trough-crossbedded sandstone, as well as marine-facies turbiditic sedimentary rocks (Figure 3b). Polymictic conglomeratic beds contain clasts of mafic volcanic rocks, felsic volcanic rocks, granitoids, chert and smoky quartz.

The Cadillac and Timiskaming rocks are overprinted by regional folds with an axial planar regional cleavage striking west-northwest and dipping steeply to the north and south (Figure 4). The regional cleavage is expressed as a continuous slaty cleavage in mudstone, as a spaced disjunctive cleavage in sandstone, and by the flattening and elongation of clasts in conglomerate. It is oriented anticlockwise to north-facing beds (Figure 3b) and clockwise to south-facing beds., Tight to isoclinal, S-shaped and Z-shaped parasitic folds (Figure 3c) are present on opposite limbs of the regional folds. The parasitic folds plunge moderately to shallowly to the east-southeast parallel to a mineral stretching lineation, which is defined by biotite porphyroblasts in turbiditic sandstone (Figures 3d) and elongation of clasts in conglomerate. Two stripped mineralized outcrops, TR16-10 (Figure 5) and TR16-02 (Figure 6), which are located on opposite limbs of a regional fold, were mapped in detail and are described below.

Stripping TR16-10 (708141E, 5341183N; UTM Zone 17, NAD83)

Stripping TR16-10 is located on the north-younging northern limb of a regional anticline. It consists of turbiditic siltstone and mudstone and thick-bedded sandstone. Beds strike ~290˚ and dip steeply to the north. The steeply-dipping regional cleavage strikes 280˚ anticlockwise to bedding. A mineral stretching lineation is parallel to parasitic fold axes and plunges moderately toward the east-southeast (105˚).

Four generations of quartz veins (V1 to V4) are present on outcrop. The V1 veins (Figure 7a) only occur in the thicker sandstone beds, where they form en-échelon arrays oriented roughly parallel to the cleavage. They consist of smoky quartz and vary in width from ~2 mm to 3 cm. The V2 veins (Figure 7b) are tension gashes composed of quartz, albite, Fe-carbonate and biotite, and vary in width from 2 to 5 cm, with an average length of ~10 cm. They strike 190˚ and dip moderately to the west, subperpendicular to the mineral stretching lineation. The V3 veins (Figure 7c) are sigmoidal en-échelon veins, which are also restricted to the more competent thicker sandstone beds, consist of smoky to white quartz and vary in width from 2 to 10 cm. The V4 veins (Figure 7d, e) are extensional veins composed of black smoky quartz and white quartz. Reaching up to several metres in length and 25 cm in width, these veins extend for hundreds of metres. They strike 100˚, are oriented at a low angle anticlockwise to bedding and are overprinted by tight S-shaped folds. They are surrounded by an alteration halo of chlorite, arsenopyrite, carbonate, tourmaline and biotite, which extends over 5 to 10 cm on both sides of the veins. The V4 veins and their alteration haloes are gold-bearing and returned gold assay values of 1.7–41 g/t Au (Midland Exploration Inc., 2016).

The orientation of the V3 and V4 veins anticlockwise to bedding, the sigmoidal shape of the V3 veins and the overprinting of the V4 veins by S-shaped folds are consistent with the emplacement of the veins during sinistral shearing. The veins were deformed during a subsequent deformation event. The V4 veins are boudinaged, offset by steeply-dipping dextral shear bands and overprinted by Z-shaped drag folds, due to later dextral shearing parallel to bedding (Figure 7e).

Stripping TR16-02 (706373E, 5341667N; UTM Zone 17, NAD 83)

Stripping TR16-02 is located on the south-younging southern limb of the regional anticline, where the regional cleavage is defined by flattened clasts oriented clockwise to bedding. The stripping consists of polymictic Timiskaming conglomerate interlayered with massive and normal-graded sandstone. The beds strike 280˚ and dip steeply to the north. The subvertical cleavage strikes ~290˚ and is oriented clockwise to bedding. A mineral stretching lineation defined by elongated clasts plunges moderately to shallowly toward ~100˚.

Only V2 and V4 veins are present on this outcrop. The V2 veins are oriented (~160˚/60˚) roughly perpendicular to the mineral stretching lineation (Figure 8a), whereas the S-folded V4 veins are east–west oriented anticlockwise to bedding (Figure 8b). The V4 veins are boudinaged and overprinted by dextral shear bands (Figure 8c). Granitic clasts in conglomerate are surrounded by dextral asymmetrical strain shadows and locally filled with hydrothermal minerals (Figure 8d).

SUMMARY AND CONCLUSION

The regional isoclinal folds and their axial plane cleavage formed during a north-northeast–directed shortening event. The V1 veins were emplaced prior to folding and were rotated into the orientation of the axial plane cleavage. The V2 veins were emplaced during folding as tension gashes oriented subperpendicularly to the stretching lineation. During subsequent progressive sinistral shear, the V3 veins formed as arrays of tension gashes that were curved into S-shaped folds during continued shear. The gold-bearing V4 quartz veins filled fractures oriented anticlockwise to bedding and were then folded to form an S-like shape. As the V4 veins are oriented anticlockwise to bedding on both limbs of the fold, this suggests that they formed after regional folding. Later dextral shearing parallel to bedding produced dextral shear bands, boudinage structures and dextral drag folds overprinting the V4 veins.

At the nearby Canadian Malartic gold deposit located south of the LLCDZ, gold mineralization is controlled by structures that formed during regional sinistral folding of the Pontiac metasedimentary rocks (De Souza et al., 2016). As gold mineralization in the Cadillac and Timiskaming basins is also associated with sinistral structures, its emplacement could be structurally coeval or slightly later than that of gold mineralization at the Canadian Malartic deposit.

ACKNOWLEDGMENTS

Both G Roger, President and CEO of Midland Exploration Inc., and M.-F. Bugnon, General Manager Exploration of IAMGOLD Corp., are thanked for allowing access to the Héva East property. The authors are grateful for the discussion on interpretations throughout the summer with P. Pilote of the Ministère de l'Énergie et des Ressources naturelles du Québec, as well as R. Daigneault from the Université du Québec à Chicoutimi and S. De Souza from the Université du Québec à Montréal. Lastly but not least, L. Roy is thanked for his hard work and assistance throughout the field season.

Harquail School of Earth Sciences, Mineral Exploration Research Centre contribution MERC-ME2018-066

REFERENCES

Ayer, J., Amelin, Y., Corfu, F., Kamo, S., Ketchum, J., Kwok, K. and Trowell, N. 2002. Evolution of the southern Abitibi greenstone belt base on U-Pb geochronology: autochthonous volcanic construction followed by plutonism, regional deformation and sedimentation; Precambrian Research, v. 115, p. 63–95.

Bedeaux, P., Pilote, P., Daigneault, R. and Rafini, S. 2017. Synthesis of the structural evolution and associated gold mineralization of the Cadillac Fault, Abitibi, Canada; Ore Geology Reviews; v. 82, p. 49–69.

Corfu, F. and Davis, D.W. 1991. Comment on "Archean hydrothermal zircon in the Abitibi greenstone belt: constraints on the timing of gold mineralization" by J.C. Claoué-Long, R.W. King and R. Kerrich; Earth and Planetary Science Letters, v. 104, p. 545–552.

Corfu, F., Krogh, T.E., Kwok, Y.Y. and Jensen, L.S. 1989. U–Pb zircon geochronology in the southwestern Abitibi greenstone belt, Superior Province; Canadian Journal of Earth Sciences, v. 26, p. 1747–1763.

Corfu, F., Spooner, E.T.C. and Barrie, C.T. 1993. The evolution of the southern Abitibi greenstone belt in light of precise U-Pb geochronology; Economic Geology, Bulletin of the Society of Economic Geologists, v. 88, p. 1323–1340.

Davis, D.W. 2002. U-Pb geochronology of Archean metasedimentary rocks in the Pontiac and Abitibi subprovinces, Quebec, constraints on timing, provenance and regional tectonics; Precambrian Research, v. 115, p. 97–117.

De Souza, S., Dubé, B., McNicoll, V., Dupuis, C., Mercier-Langevin, P., Creaser, R. and Kjarsgaard, I. 2016. Geology and hydrothermal alteration of the world-class Canadian Malartic gold deposit: genesis of an Archean stockwork-disseminated gold deposit in the Abitibi greenstone belt, Quebec; chapter 9 *in* Archean Base and Precious Metal Deposits, Southern Abitibi Greenstone Belt, Canada, T. Monecke, P. Mercier-Langevin, B. Dubé (ed.); Reviews in Economic Geology, v. 19, p. 263–276.

Desrochers, J.P. and Hubert, C. 1996. Structural evolution and early accretion of the Archean Malartic Composite Block, southern Abitibi greenstone belt, Quebec, Canada Canadian Journal of Earth Sciences, v. 33, p. 1556–1569.

Desrochers, J.P., Hubert, C., Ludden, J.N. and Pilote, P. 1993. Accretion of Archean oceanic plateau fragments in the Abitibi greenstone belt, Canada; Geology, v. 21, p. 451–454.

Dimroth, E., Imreh, L., Rocheleau, M. and Goulet, N. 1982. Evolution of the south-central part of the Archean Abitibi Belt, Quebec. Part I: stratigraphy and paleogeographic model; Canadian Journal of Earth Sciences, v. 19, p. 1729–1758.

Goulet, N. 1978. Stratigraphy and structural relationships across the Cadillac-Larder Lake Fault, Rouyn-Beauchastel area, Quebec; Ph.D. thesis, Queen's University, Kingston, Ontario, 286 p.

Goutier, J. 1997. Géologie de la région de Destor; Ministère des Ressources naturelles du Québec, report RG 96-13, 37 p.

Hubert, C., Trudel, P. and Gelinas, L. 1984. Archean wrench fault tectonics and structural evolution of the Blake River group, Abitibi belt, Quebec; Canadian Journal of Earth Sciences, v. 21, 1024–1032.

Hyde, R.S. 1980. Sedimentary facies in the Archean Timiskaming Group and their tectonic implications, Abitibi greenstone belt, northeastern Ontario, Canada; Precambrian Research, v. 12, p. 161–195.

Imreh, L. 1984. Sillon de La Motte–Vassan et son avant-pays méridional: synthèse volcanologique, lithostratigraphique et gîtologique; Ministère de l'Énergie et des Ressources du Québec, Direction générale de l'exploration géologique et minérale, MM82-4, 72 p., 2 maps.

Lafrance, B., Moorhead, J. and Davis, D.W. 2003. Cadre géologique du camp minier de Doyon-Bousquet-Laronde: Ministère des Ressources naturelles, de la Faune et des Parcs du Québec, report ET 2002-07, 43 p.

Landry, J. 1991. Volcanologie physique et sédimentologie du groupe volcanique de Piché et relations stratigraphiques avec les groupes sédimentaires encaissants de Pontiac et de Cadillac; unpublished M.Sc. thesis, Université du Québec à Chicoutimi, Chicoutimi, Quebec, 210 p.

Latulippe, M. 1976. Excursion géologique: la région de Val d'Or–Malartic; Ministère des Richesses naturelles du Québec (ed.), Institut canadien des mines et de la métallurgie, DPV-367, 129 p.

McNicoll, V., Goutier, J., Dubé, B., Mercier-Langevin, P., Ross, P.-S., Dion, C., Monecke, T., Legault, M., Percival, J. and Gibson, H. 2014. U–Pb Geochronology of the Blake River Group, Abitibi greenstone belt, Quebec, and implications for base metal exploration; Economic Geology, v. 109, p. 27–59.

Mercier-Langevin, P., Dubé, B., Hannington, M.D., Richer-Laflèche, M. and Gosselin, G. 2007. The LaRonde Penna Au-rich volcanogenic massive sulfide deposit, Abitibi greenstone belt, Quebec: Part II. Lithogeochemistry and paleotectonic setting; Economic Geology, v. 102, p. 611–631.

Midland Exploration Inc. 2016. Midland continues to discover several new gold-bearing zones on its Heva project, with grades up to 41.0 g/t Au by prospecting; news release, December 20, 2016, http://www.midlandexploration.com/en/Communique.aspx?ResourceId=31fa1039-8a5a-4807-a8c7-2ea5bc814052 [last accessed: September 2018].

Mortensen, J.K. 1993. U-Pb geochronology of the eastern Abitibi Subprovince. Part 2: Noranda–Kirkland Lake area; Canadian Journal of Earth Sciences, v. 30, p. 29–41.

Perrouty, S., Gaillard, N., Piette-Lauzière, N., Mir, R., Bardoux, M., Olivo, G.R., Linnen, R., Bérubé, C., Lypaczewski, P., Guilmette, C., Feltrin, L. and Morris, W. 2017. Structural setting for Canadian Malartic style of gold mineralization in the Pontiac Subprovince, south of the Cadillac Larder Lake Deformation Zone, Québec, Canada; Ore Geology Reviews, v. 84, p. 185–201.

Pilote, P. 2013. Géologie Malartic, 32D01-NE; Ministère de l'Énergie et des Ressources naturelles du Québec, CG-32D01D-2013-01.

Pilote, P., Daigneault, R., David, J. and McNicoll, V. 2015. Architecture of the Malartic, Piché and Cadillac groups and the Cadillac Fault: geological revisions, new dates and interpretations; Ministère de l'Énergie et des Ressources naturelles du Québec, DV 2015-04. 37 p.

Pilote, P., Scott, C.R., Mueller, W., Lavoie, S. and Riopel, P. 1999. Géologie des formations de Val-d'Or, Héva et Jacola: nouvelle interprétation du groupe de Malartic; *in* Explorer au Québec : le défi de la connaissance. Séminaire d'information sur la recherche géologique, programme et résumés, 1999; Ministère de l'Énergie et des Ressources, DV 99-03, 52 p.

Simard, M., Gaboury, D., Daigneault, R. and Mercier-Langevin, P. 2013. Multistage gold mineralization at the Lapa mine, Abitibi Subprovince: insights into auriferous hydrothermal and metasomatic processes in the Cadillac–Larder Lake Fault Zone; Mineral Deposits, v. 48, p. 883–905.

Thurston, P.C., Ayer, J.A., Goutier, J. and Hamilton, M.A. 2008. Depositional gaps in Abitibi greenstone belt stratigraphy: a key to exploration for syngenetic mineralization; Economic Geology, v. 103, p. 1097–1134.

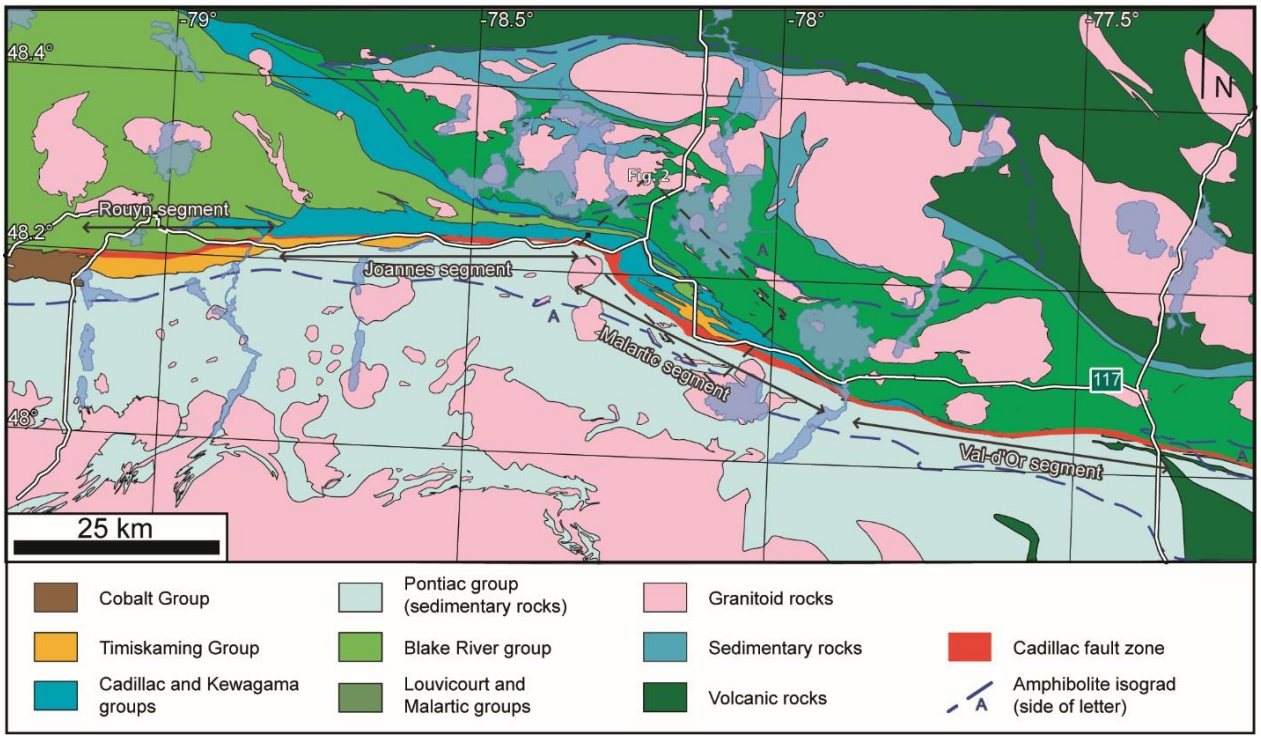

Figure 1. Regional geology of the Larder Lake–Cadillac deformation zone (LLCDZ) subdivided into four segments. Figure *modified from* Hubert et al. (1984), Imreh (1984), Desrochers and Hubert (1996) and Bedeaux et al. (2017).

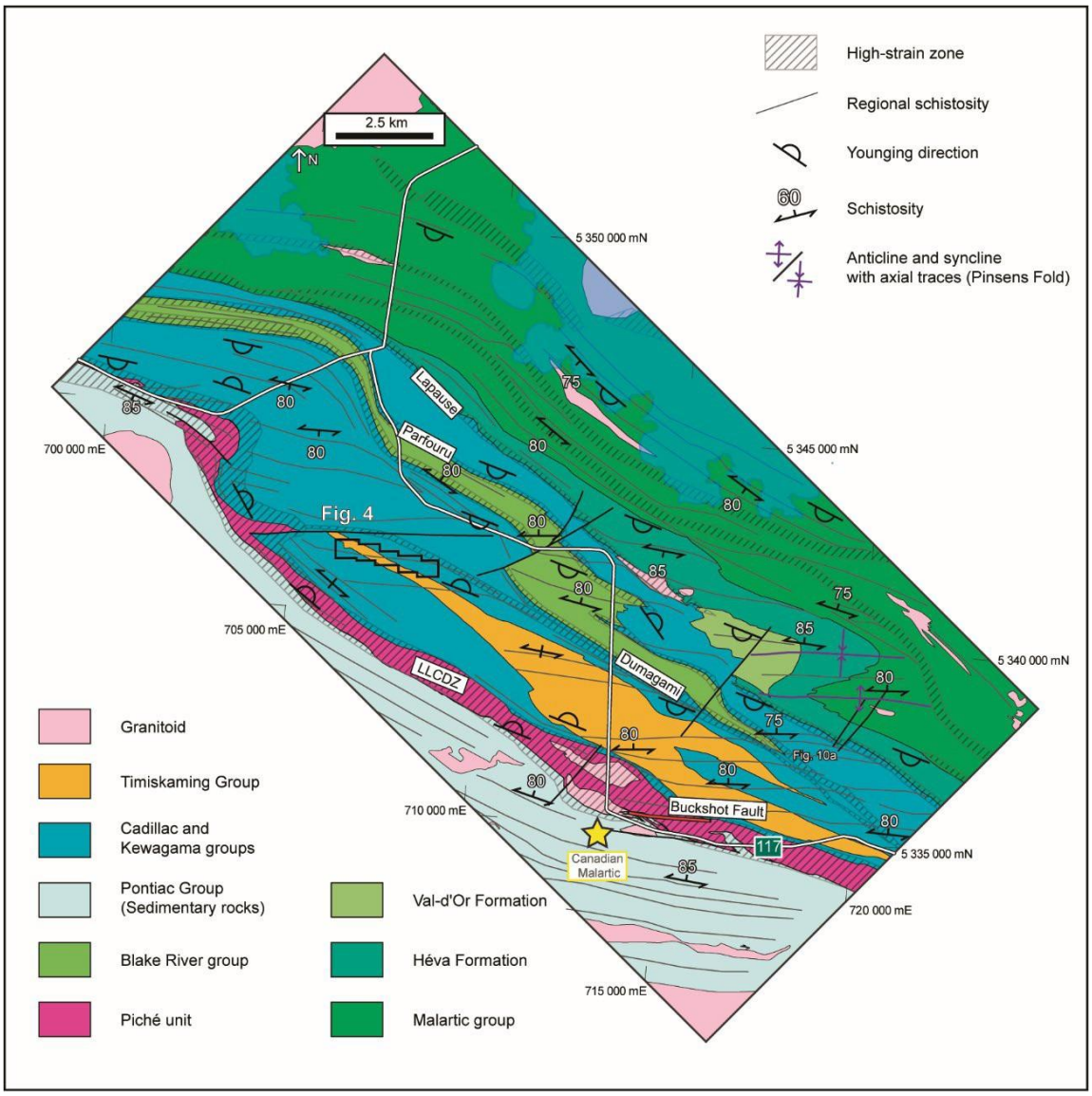

Figure 2. Geology of the Malartic segment of the Larder Lake–Cadillac deformation zone (LLCDZ). Figure *modified from* Desrochers et al. (1993), Desrochers and Hubert (1996), Pilote et al. (1999), Pilote (2013), Pilote et al. (2015) and Bedeaux et al. (2017). Outline in black shows location of Figure 4.

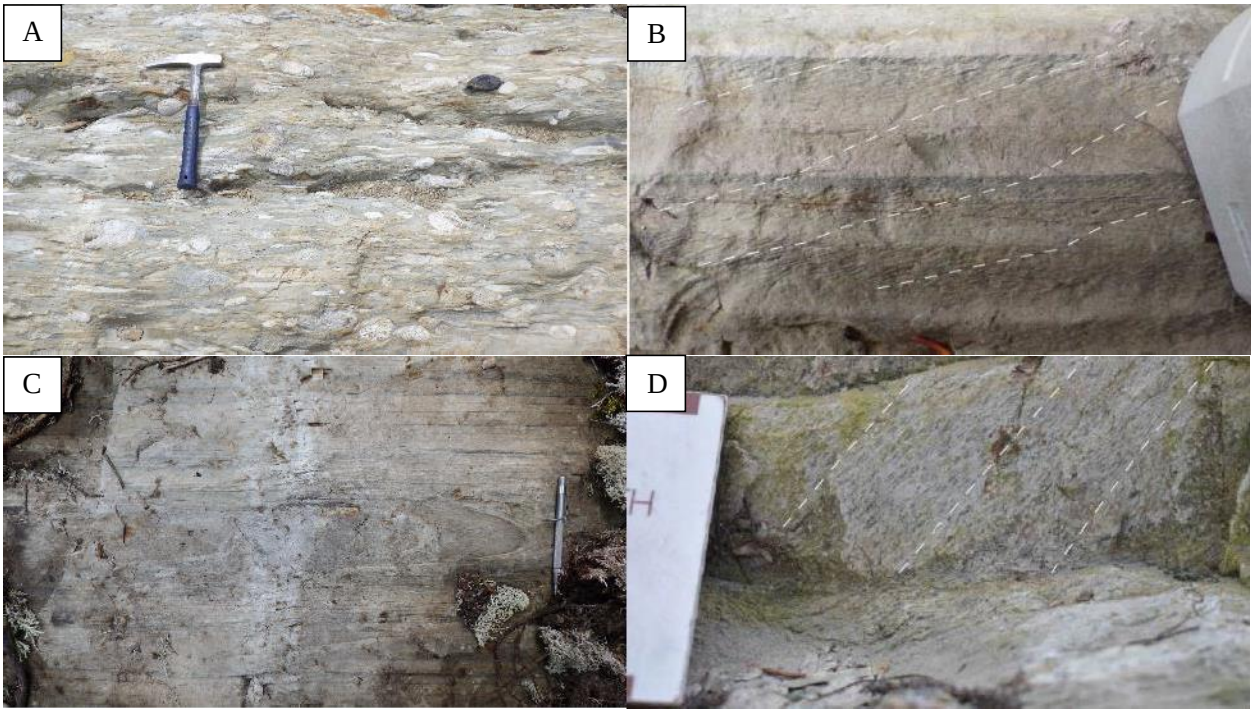

Figure 3. Field photographs of the lithological units of the Timiskaming Group in the Abitibi greenstone belt: **a)** typical Timiskaming polymictic conglomerate (hammer is 33 cm long); **b)** north-younging, normal-graded turbiditic sandstone of the Timiskaming Group overprinted by an anticlockwise cleavage indicated by white dashed lines (compass is 7 cm long); **c)** isoclinal fold parasitic to regional folds (pen magnet is 13 cm long); **d)** biotite porphyroblasts define regional stretching lineation indicated by white dashed lines (photo card is 5 cm in width).

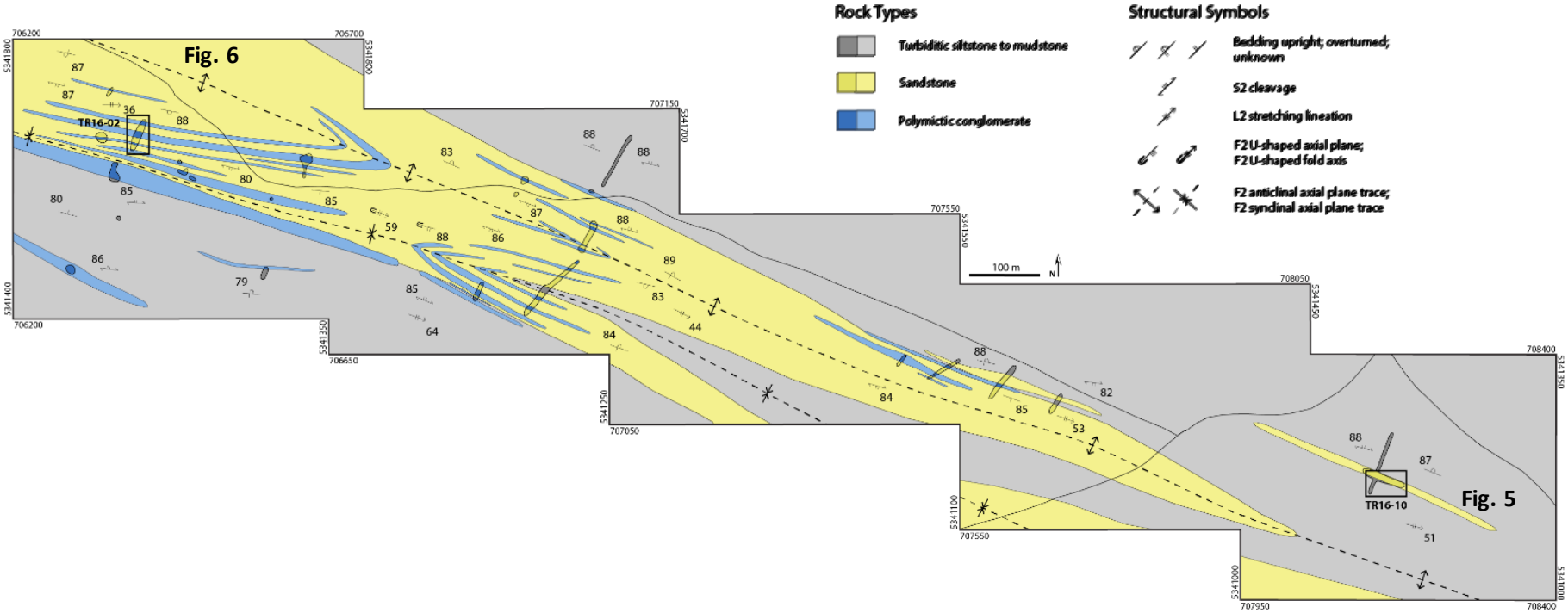

Figure 4. Geological map, showing regional isoclinal anticline and syncline in Timiskaming conglomerate, sandstone and turbidites at 1:2000 scale.

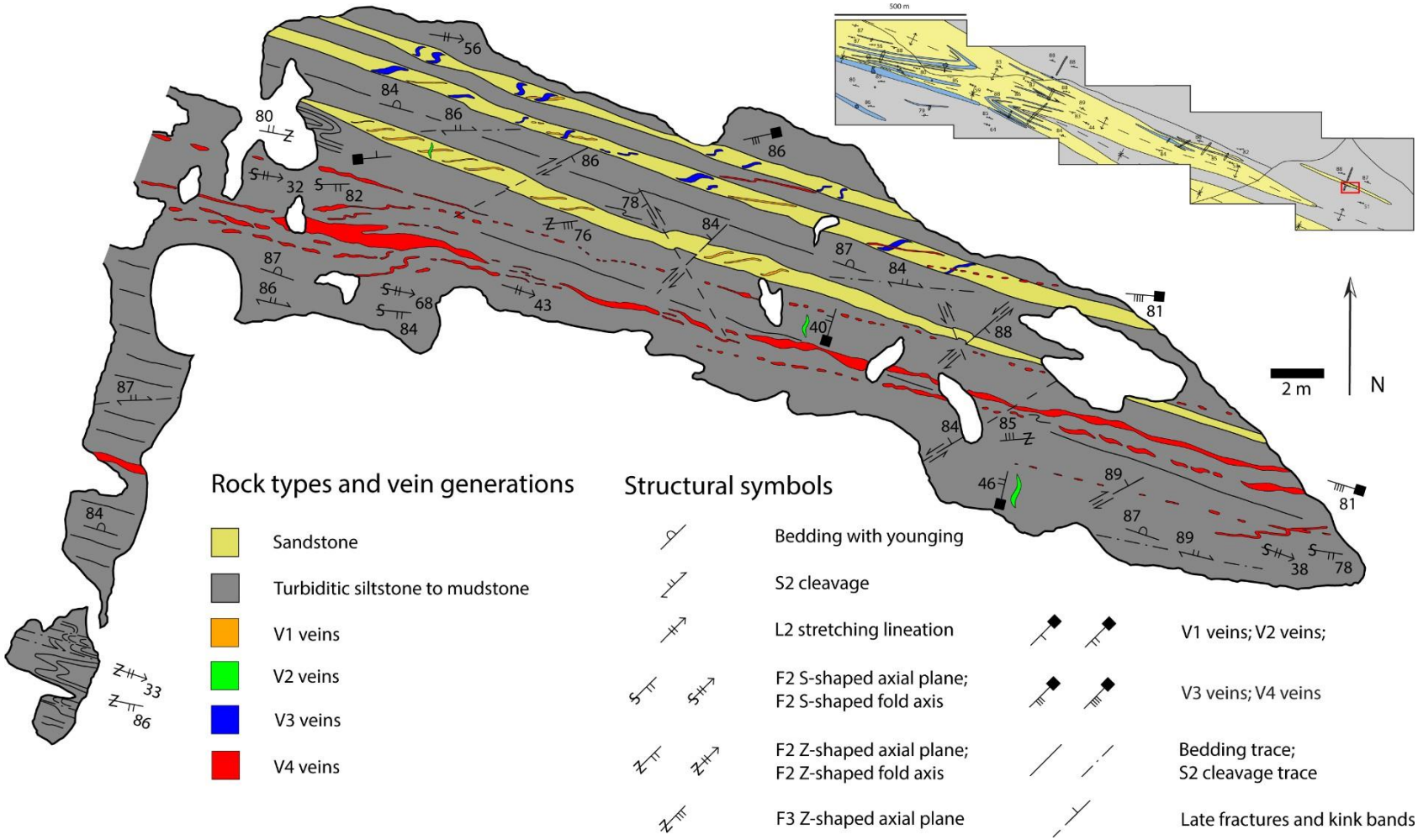

Figure 5. Geology of stripped mineralized outcrop TR16-10 located on the northern limb of a regional anticline of the Abitibi greenstone belt. Bedding is younging toward the north on this outcrop, with the cleavage oriented anticlockwise to the bedding. The gold-bearing V4 quartz veins are shown in red. Inset shows location of outcrop on Figure 4.

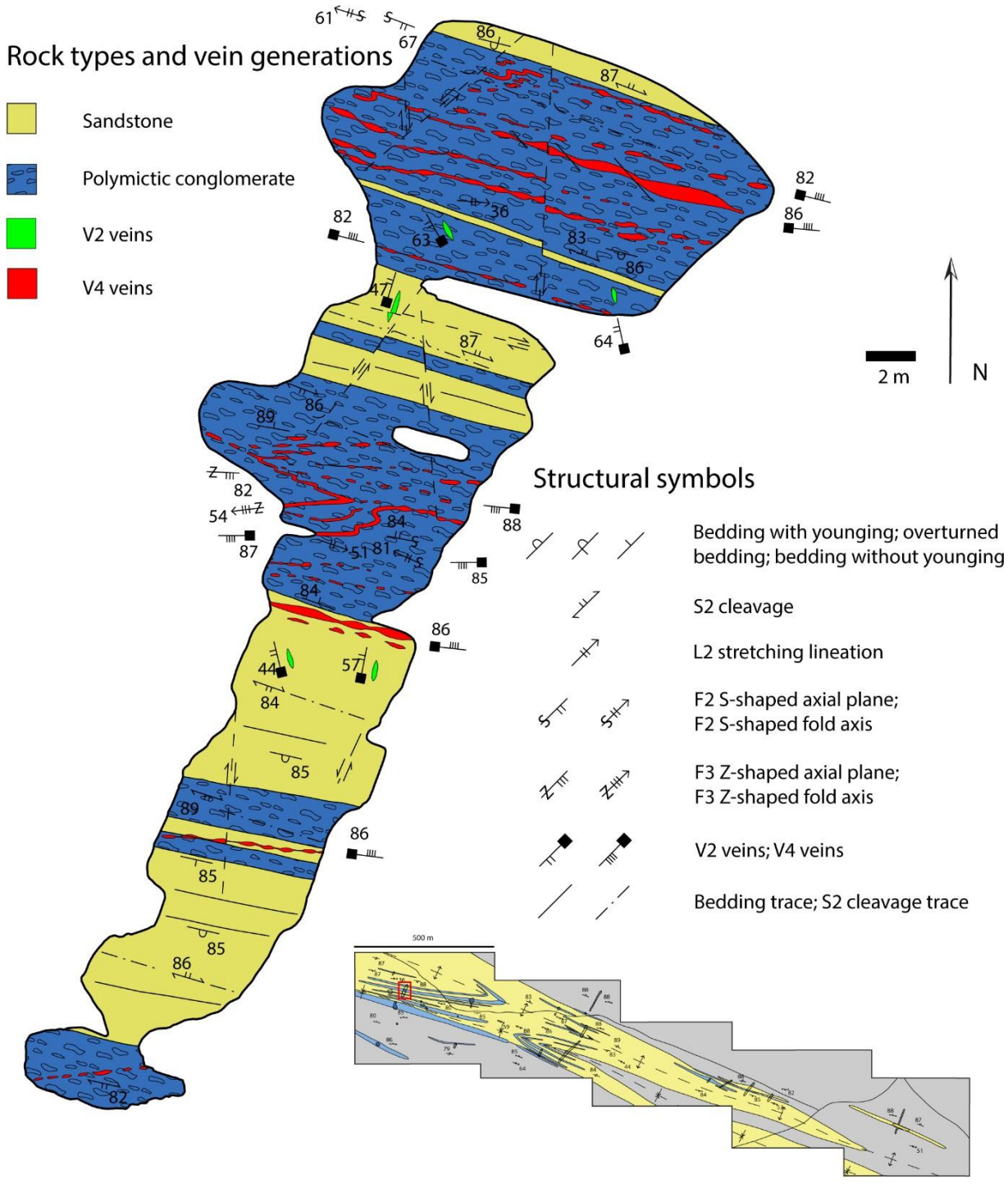

Figure 6. Geology of stripped mineralized outcrop TR16-02 located on the southern limb of a regional anticline of the Abitibi greenstone belt. Bedding is younging toward the south, with the cleavage oriented clockwise to the bedding. Gold-bearing V4 veins are shown in red. Inset shows location of outcrop on Figure 4.

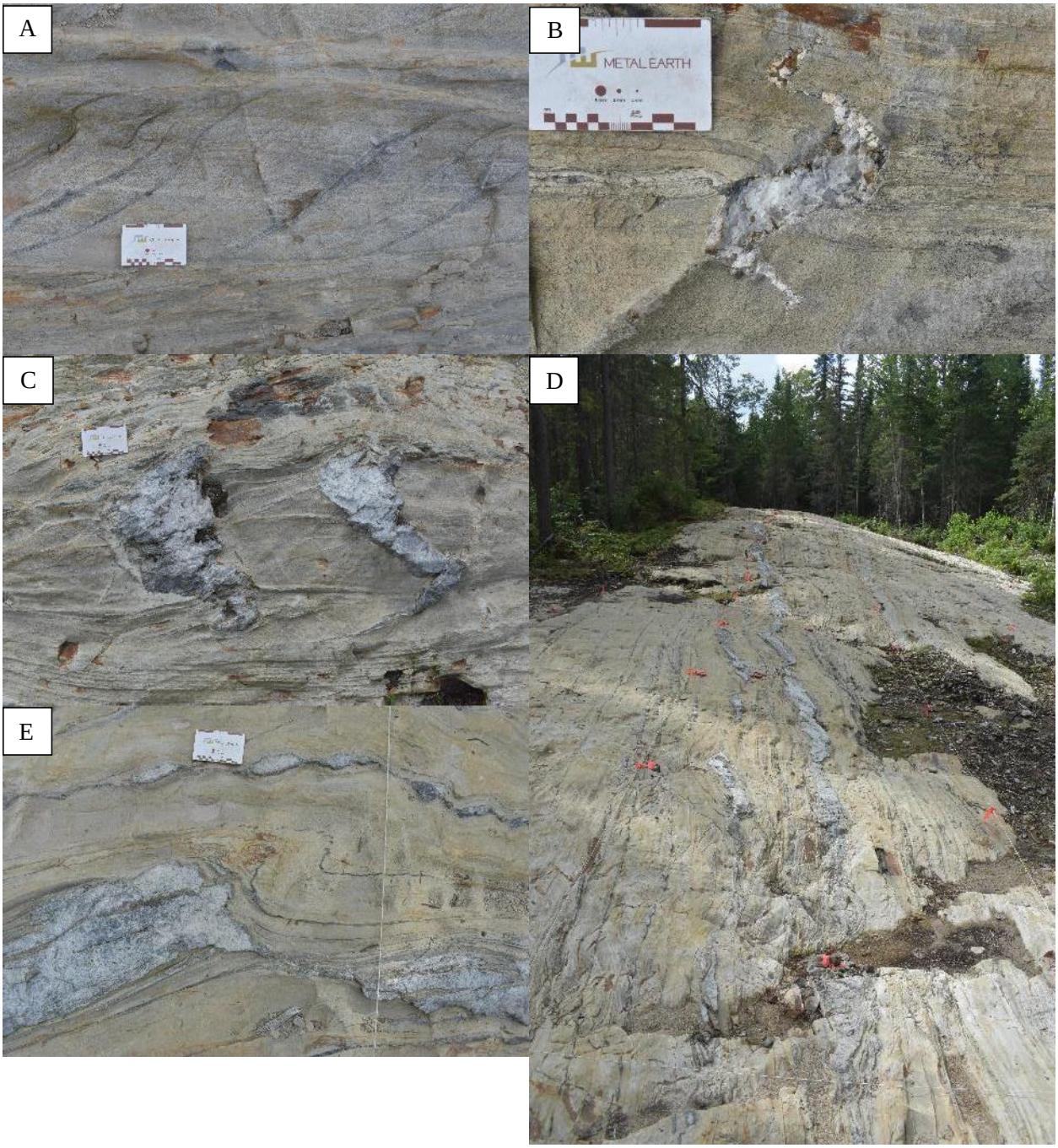

Figure 7. Field photographs of V1 to V4 veins on stripped mineralized outcrop TR16-10 located on the northern limb of a regional anticline of the Abitibi greenstone belt: **a)** dark quartz, en-échelon V1 veins (photograph card measures 8 cm); **b)** Z-shaped V2 tension gash (photograph card measures 8 cm); **c)** smoky to white quartz, S-shaped V3 veins (photograph card measures 8 cm); **d)** smoky to white quartz, extensional V4 veins oriented at a low angle anticlockwise to bedding (spacing between orange flagging is 2 m); **e)** boudinaged V4 veins overprinted by dextral shear bands and flanked by late Z-folds (photograph card measures 8 cm).

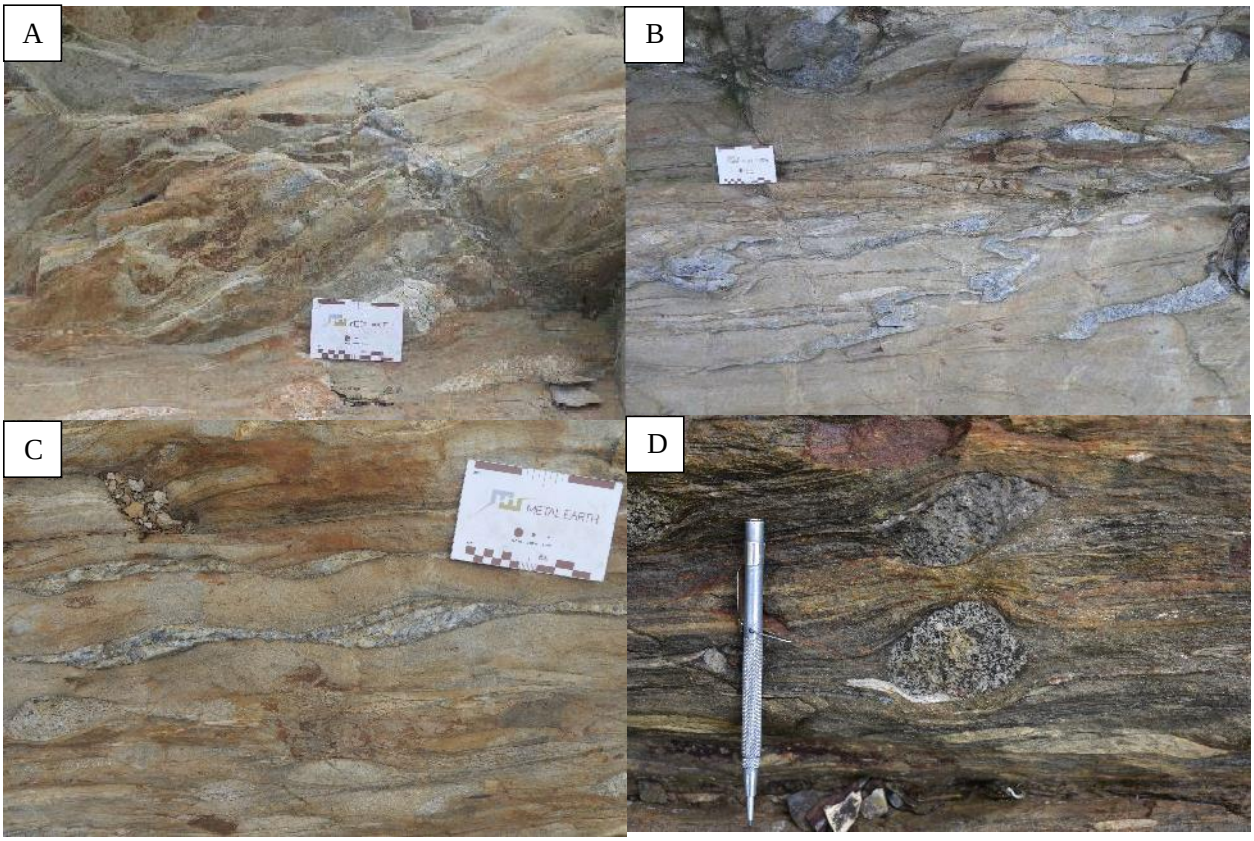

Figure 8. Field photographs from stripped mineralized outcrop TR16-02 located on the southern limb of a regional anticline of the Abitibi greenstone belt: **a)** V2 vein oriented subperpendicularly to the stretching lineation (photograph card measures 8 cm); **b)** S-folded V4 vein oriented anticlockwise to bedding (photograph card measures 8 cm); **c)** V4 veins, which have been boudinaged and cut by dextral shear bands (photograph card measures 8 cm); **d)** Dextral asymmetrical strain shadows surrounding granitoid clasts in conglomerate (pen magnet is 13 cm long).